Quantum cascade lasers as super terahertz local oscillators for astronomy

Behnam MIRZAEI

Quantum cascade lasers as super terahertz local oscillators for astronomy

Dissertation

for the purpose of obtaining the degree of doctor
at Delft University of Technology
by the authority of the Rector Magnificus, prof.dr.ir. T.H.J.J. van der Hagen,
Chair of the Board for Doctorates
to be defended publicly on
Tuesday 4 September 2018 at 15:00 o'clock

by

Behnam MIRZAEI

Master of science in electrical engineering, University of Tabriz, Iran
Born in Arak, Iran

This dissertation has been approved by the promoter and the copromoter.

Composition of the doctral committee:

Rector Magnificus,	chairperson
Prof.dr.ir. L.P. Kouwenhoven	Delft University of Technology, promoter
Dr. J.R. Gao	Delft University of Technology, copromoter

Independent members:

Prof.dr. C. Walker	University of Arizona, USA
Prof.dr. X. A.G.G.M Tielens	Leiden University
Prof.dr. L.B.F.M Waters	University of Amsterdam
Prof.dr. H.P. Urbach	Delft University of Technology
Dr. D.J. Hayton	NASA Jet Propulsion Laboratory (JPL) , USA
Prof.dr. L. Kuipers	Delft University of Technology, reserve member

Keywords: terahertz, quantum cascade laser, local oscillator, astronomy

Printed by: Gildeprint

Cover: Front, 3D plot of a part of the 4.7 THz 8-pixel phase grating (chapter 6). Back, GUSTO, studying the life cycle of the interstellar medium. Background, highly magnified SEM photo of the phase grating in front, coloured with a THz image of the Cygnus-X star-forming region, taken by Herschel.

Casimir PhD series, Delft-Leiden 2018-24

ISBN 978-90-8593-353-3

An electronic version of this dissertation is available at: http://repository.tudelft.nl

Contents

1

INTRODUCTION

After an overview on THz astronomy, what the work in this thesis tries to facilitate, a review on different THz detection techniques is given in this chapter. It is tried to address the relative key state-of-the-art technologies especially in heterodyne detection systems and clarify the vital role of the local oscillator.

1.1. THz window into cosmic evolution

The interstellar medium (ISM) is the material between the stars in space. The ISM is also the place where the stars are formed in its densest regions, live in and die through replenishing it with matter and energy. In other words, galactic evolution is mainly driven by the ISM mass and energetics. The ISM mainly consists of gas by 99 %[*], dominated by hydrogen in its different neutral atomic, ionic and molecular forms and dust by 1 %, made of micron-size particles predominantly of carbon and silicon. Although it makes up a tiny bit of the ISM, dust has a huge effect on light propagation in space especially when its grain size is comparable to the wavelength acting as a strong scatterer. The latter causes an effect called extinction, which happens strongly on visible, ultraviolet (UV) and even infrared (IR) radiations.

Our solar system was formed about 4.6 billion years ago out of violent processes in the local ISM of our Milky Way. The latter consists of multiple sub-mediums or phases with major differences in material, being either ionized or neutral, temperature and density. These phases include: hot ionized medium (HIM), warm neutral medium (WNM), warm ionized medium (WIM) and the cool neutral medium (CNM).

The HIM consisting of very low density ionized gas with a temperature of more than $10^{5.5}$ K, fills about a half of the ISM volume, looking like its background. However, it only contributes by about 0.2 % to the overall mass of the ISM. The WNM containing higher density natural atomic hydrogen with a temperature of about $10^{3.7}$ K, occupies about 40 % of the ISM volume. The largest portion of the whole ISM thermal energy is included in WNM by about 53 %. The gas ionized by the extreme ultraviolet (EUV) radiation from massive stars forms the low density WIM phase with the same order of temperature to the WNM, taking up about 10 % of the ISM volume. Finally, the CNM is mainly made of neutral atomic hydrogen with a temperature of about 100 K. Clouds of diffuse molecular hydrogen, H_2, are

[*] Most of the astronomical statistical information are adapted from [1].

possible to be formed in high density regions of the CNM. They take about 0.1 % of the ISM volume while the CNM itself fills it by about 1 %.

The density of hydrogen atoms in some regions of the CNM is sufficiently high, so that gravity dominates the expansion induced by the thermal energy. Thereon the matter starts to contract and continues as long as the heat can be radiated away. At a certain stage, where the gas gets dense enough, hydrogen atoms start to block the far ultraviolet (FUV) light emitted by the background stars, from passing into the formed cloud. This FUV blockage lets molecular hydrogen (H_2) form via a chemical reaction on dust surfaces. The bounding force of the resulted H_2 to the dust is low enough to be broken by the reaction generated heat itself and let H_2 be released. Increasing the density of H_2 happens along with increasing the dust density, which is a good FUV absorber and further fortifies the molecular formation, leading to a molecular cloud.

Figure 1.1. Barnard 68 molecular cloud, dark because of a high optical extinction

Molecular clouds with large amounts of gas and dust are the birth place of stars. Those with the mass exceeding of about 10^5 suns are called giant molecular clouds (GMC), the most massive and largest objects in galaxies. They can be as giant as 600 light-years (ly) in diameter. Because of the large optical extinction

introduced by the high density dust they appear dark when looked by an optical telescope. Figure 1.1 shows this effect in the molecular cloud *Barnard 68* at a distance of about 500 ly with a diameter of 0.5 ly.

Despite of the abundance of H_2, it does not have a radiation being able to pass through the dust and bring valuable information out. However besides it, GMCs have small amounts of other gases like carbon, oxygen and nitrogen, which can also produce compound gases where the FUV light is blocked. These gases cool the ISM by their line radiation with wavelengths far larger than the dust grain size and provide useful tools to probe the dynamics within the ISM. These probes all are in the THz frequency range (f ~ 1–10 THz; corresponding to the wavelength λ ~ 300–30 μm).

The regions with H_2 densities of 10^3–10^6 cm^{-3} and temperatures of 10–50 K within a GMC are called cloud clumps or cores, where the stars are formed. These regions are referred to as cold dense molecular clouds (CDM) filling about 0.01 % of the Milky Way volume. Depending on the cloud conditions a could core can further and further collapse until its outward thermal pressure reaches equilibrium with gravitational energy and collapse gets halted. What has been formed is called a protostar with H_2 density of about 10^{10} cm^{-3}.

To conserve the rotational momentum, the protostar spins up as it further contracts and a disk is formed around, where it accretes more material from the natal cloud through. The disk evolution process lasts long (10^7 years) until a planetary system is formed. Finally, massive stars return their masses to the ISM by going supernova. Stars have a great impact during their life time on the ISM through several mechanisms such as bipolar outflows, stellar winds, ionizing radiation and supernova explosions. These all cause to disrupt the surrounding cloud and bring it back to the warm natural/ionized gas state and close the ISM life cycle. Figure 1.2 depicts all the phases of the ISM life cycle, where in each, specific THz molecular lines can be used to probe.

Formation probability of ions depends on the ionization potential, which should

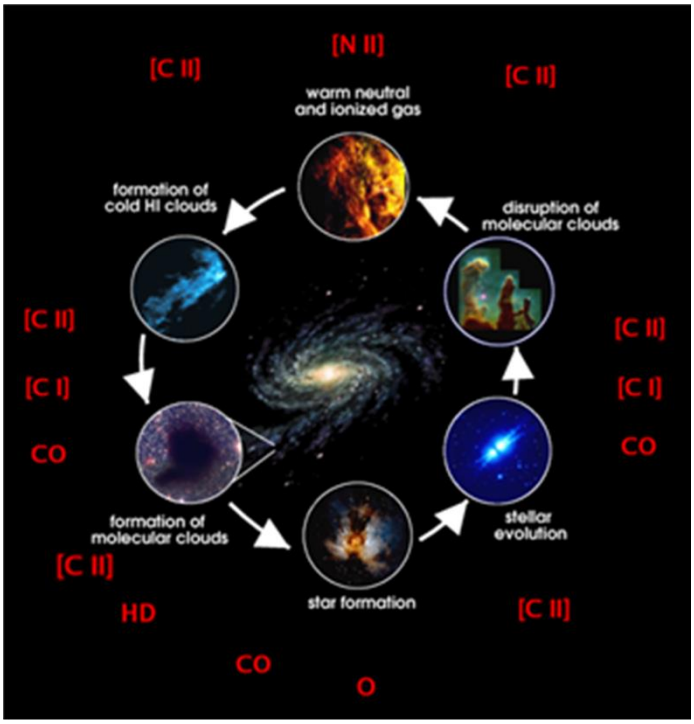

Figure 1.2. The interstellar medium life cycle. Specific molecular lines can probe the evolution status (adapted from [1])

be smaller than the flowing photons energies. Table 1.1 summarises some important elements together with their abundances in the natural form (normalized to hydrogen), ionization potentials from natural to singly ionized state and also useful emission line frequencies and wavelengths.

Element	Abundance in natural form	Natural to single-ionization potential (eV)	THz Emission Frequency	Corresponding Wavelength (μm)
HII	1	13.5984	N.A.	N.A.
CII	2.95×10^{-4}	11.2603	1.901	157.74
NII	7.41×10^{-5}	14.5341	1.461	205.18
OI	5.37×10^{-4}	13.61	4.745	63.18

Table 1.1. The abundances, ionization energies and bright THz emission frequencies and wavelengths of some important ISM elements

Since Hydrogen is more abundant by far, it absorbs almost all the photons with energies more than 13.6 eV. Therefore the ions with ionizing potentials beyond hydrogen's can be formed only in the strongly ionized regions, where the photons left over is enough for. In the table 1.1 and also among other abundant elements, carbon is the only one having the ionizing potential less than hydrogen causing its appearance in both ionized and natural regions and basically in all phases of the ISM. This fact makes [CII] the brightest and the most important emission line (at 1.9 THz) from a galaxy. The competence only happens in very high density and hot regions, where the star formation is happening and when the [OI] emission at 4.7 THz becomes a significant coolant and a useful probe. The difficulty of distinguishing the origin of [CII], arisen form its existence in all the ISM phases can be overcome using [NII] line at 1.4 THz, which has the same excitation requirement except the ionizing potential. This means that everywhere [NII] appears, [CII] is present too, making it possible to find out whether the latter originates from ionized or natural regions.

One of the major challenges in ground-based THz astronomy is the huge atmospheric absorption mainly caused by water vapour. To overcome this obstacle THz observations should be performed at the highest accessible altitudes, where it gets drier. Figure 1.3 shows the atmospheric transmission at three different altitudes on the left and the corresponding instruments implemented around these altitudes on the right.

At a typical mountaintop altitude of 4.2 km almost no signal can be received above 1 THz, while it is still worthy to develop ground-based observatories for looking at the lower, far-infrared or sub-mm side. ALMA (Atacama Large Millimetre/submillimetre Array), located at Chajnantor in the middle of the Chile's Atacama desert with 5000 meters above sea level, is a good example.

To go further, an airplane with a non-standard powerful motor can be employed to reach 12 km above, where a big portion of THz can be seen moderately while the rest is still suffering from a considerable absorption. SOFIA (Stratospheric Observatory for Infrared Astronomy) on board of a Boeing 747SP

aircraft tries to look at some important THz emission lines using its GREAT (German Receiver for Astronomy at Terahertz frequencies) heterodyne instrument.

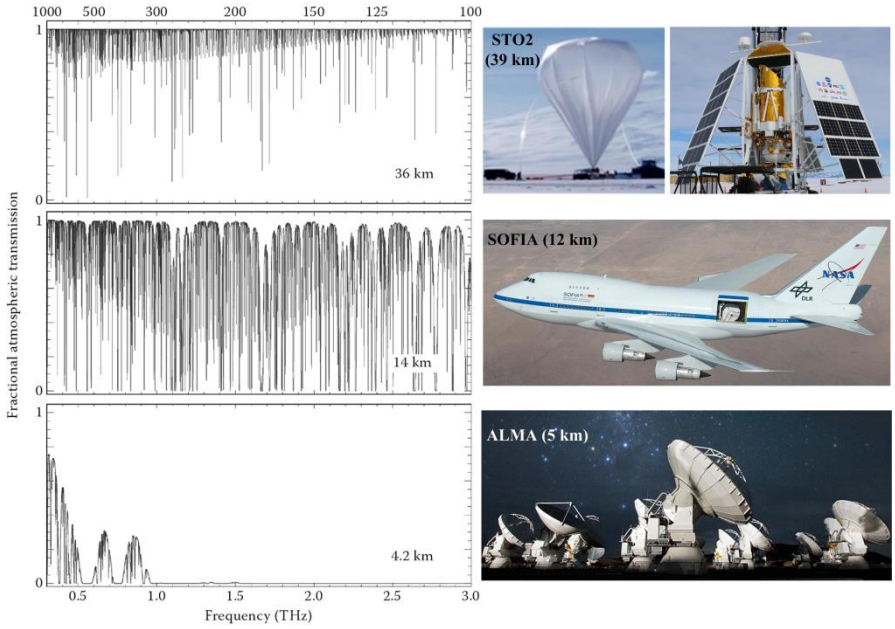

Figure 1.3. Left: Atmospheric transmission at three different altitudes [1], Right: Implemented instruments around corresponding altitudes on the left

Whilst going to space is the ultimate solution, sitting at the edge of it using the balloon technology greatly compromises the cost and maintains a decent atmospheric clarity. The latter can be realized from the top section of Fig. 1.3 at 36 km altitude. This approach allows for a continues THz observation for tens of days, enough to deeply look at a particular object or cover a large area in mapping missions. STO2 (Stratospheric/Spectroscopic Terahertz Observatory 2) with a successful operation in December 2016 is the only THz instrument based on this concept. GUSTO (Galactic/X-galactic Ultra-duration-balloon Spectroscopic/Stratospheric Terahertz Observatory) with 8-pixel heterodyne array receivers would be the next balloon-borne THz observatory, planned to launch at

2021 from Antarctica. It is aimed to look at three crucial emission lines of N[II], C[II] and O[I] at respective frequencies of 1.4, 1.9 and 4.7 THz simultaneously.

1.2. THz coherent detection

To resolve atomic/molecular lines of emission/absorption for probing the physics and dynamics of the ISM, detectors with very high spectral resolution are demanded. The [NII] spectral linewidth (at 1.4 THz) of ~ 4.7 MHz, when a velocity dispersion of 1 km/s is assumed, indicates how narrow a line can be. The challenging THz frequency region (> 1 THz) in terms of technology maturity, which is often called *THz gap,* does not allow for a direct measurement with very high resolution. Direct detectors have only been demonstrated up to couple of hundreds of GHz, still with poor resolution for such line measurements. The coherent or indirect detection in contrast provides the required resolution by translating the signal from THz to microwave, where the technology is advanced enough for further processing steps. This technique has been widely used for many different proposes including their daily use in cell-phones, TVs and wireless networks for about a century. However its advancement in THz has been under great research and development in the past decades.

A simple block diagram of the technique principle is shown in Fig. 1.4. The THz signal received by the telescope (the blue solid arrows in Fig. 1.4) is guided through an intermediate optical system to reach to a point, where it gets combined with a much stronger signal generated locally with a very close frequency to the target (the red dashed arrow in Fig. 1.4). The latter is called local oscillator (LO) acting basically as a reference with respect to which the THz signal gets measured. The combination of these two signals is usually performed using a thin dielectric beam splitter with a certain transmittance and reflectance. Since the power received from a celestial source is much smaller, the beam splitter is adjusted such to provide a higher transmission for, e.g. 90 %, whilst the LO gets reflected only with a small fraction e.g. 10 %. This great loss of the LO makes it even more challenging to

provide a sufficiently powerful source at this intrinsically challenging frequency range.

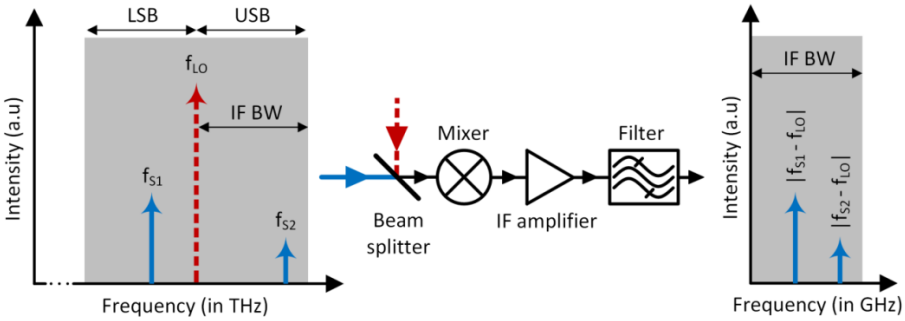

Figure 1.4. The block diagram of the coherence detection technique. The blue (solid) indicates the THz signal and red (dashed) the LO

After combination, THz signal and LO enter together to a mixer that can be either a non-linear device or a superconducting bolometer with a relatively short thermal time constant. A mixer element has a current-voltage (I-V) characteristics such that its input voltage affects the current in a squared form. Such squaring of the combined signal leads to formation of a component with a frequency equal to the frequency difference between THz signal and LO i.e. intermediate frequency (IF). One crucial characteristic of a mixer element is the maximum frequency difference between LO and signal, at which it can still function, named IF bandwidth, which is in GHz range (grey area in Fig. 1.4). It can be noticed in Fig. 1.4 that as long as the THz signal is within the IF bandwidth of the mixer, it gets down converted no matter if it is in upper sideband (USB) or lower one (LSB), causing difficulty to distinguish. The latter can be overcome if another measurement with a slightly shifted LO in frequency is performed. Then the IF gets higher or lower depending on its sideband of origin. This is the double sideband (DSB) intrinsic operation of a mixer. One can suppress the unwanted sideband and operate in the single sideband (SSB) mode using quasi-optical filters or by employing two mixers for image rejection through phase cancellation [2]. Besides the mixer implementation in the simplest form of setup, there are couple of arrangements of

mixers and LO such as sideband separation [3] or balanced DSB [4], each with some strong and weak points in addressing the noise issue, complexity, spectral confusion, etc.

Since the IF signal power (output of the mixer) is tiny comparing to what a typical power detector requires, it needs to be amplified tremendously (~ 130 dB) [1], which is usually done by cascading couple of amplifiers. High mobility field effect transistors (FETs) are the key components of low noise IF amplifiers implemented in THz receivers. The amplified signal with a microwave frequency then gets filtered and further processed. This receiver architecture is also called "heterodyne" based on the fact that more than one signal are employed in the process.

1.2.1. Receiver noise temperature and quantum noise limit

The sensitivity of a heterodyne receiver is characterized by its noise temperature (T_n), which is basically a representation of the noise power P_n in a bandwidth BW as $T_n=P_n/kBW$, where k is the Boltzmann constant. Due to the Heisenberg Uncertainty Principle applied for the electromagnetic field, $\Delta N\Delta\varphi \geq 1$, where ΔN and $\Delta\varphi$ are the uncertainties of the number of photons and the phase. Since in the coherent detection the phase information of the incoming signal is preserved, $\Delta\varphi \leq 1$ and so ΔN has a minimum of 1 [5]. It means that any measurement of the incoming energy at any given time has a minimum uncertainty of the energy of a single photon, $hf=kT$, where *h, f and T* are the Planck constant, frequency and photon effective temperature respectively. In other words there is a fundamental quantum noise limit (T_N), over which the receiver noise temperature cannot be improved, i.e. $T_N=hf/k$. It is identical to say that a perfect receiver with a terminated input to a perfectly matched load at zero Kelvin still shows fluctuations in its output power, equal to a single photon energy [6].

The usual way to measure the noise temperature of a THz receiver is using so-called Y-factor measurements. In this method a hot and a cold black-body sources with respective temperatures of T_H and T_C are repeatedly placed in front of the

receiver and the corresponding output powers of P_H and P_C are measured. The Y-factor then is calculated by $Y=P_H/P_C$. Using Raleigh-Jeans approximation (valid at lower frequencies) for P_H and P_C, the receiver noise temperature is derived as

$$T_n = \frac{T_H - Y.T_C}{Y - 1}$$

It should be noted that at THz frequencies the physical temperatures of T_H and T_C should be substituted with Callen-Welton temperatures [7]

$$T_{H(C)}^{C-W} = \frac{hf}{k}(e^{(hf/kT_{H(C)})} - 1)^{-1} + \frac{hf}{2k}$$

T_H and T_C are most often taken as 295 K (room temperature) and 77 K (liquid nitrogen temperature) to provide a reliably measurable difference in the output power.

Besides the mixer element the receiver also consists of other components like optics and IF amplifiers each with a certain noise contribution. Great efforts have been put during the past decade to reduce the noise temperature i.e. increasing the sensitivity of THz heterodyne receivers by improving the performance of all the components. As a result, the state-of-the-art sensitivities of such receivers are now close to the quantum noise limit at THz frequencies [8]. Although the progress is still being made, it gets considerably more challenging to be pushed towards the limit. On the other hand since the amount of achievement gets less by getting closer to the end, the motivation gets weaker as well. Here introducing a more practical and earlier accessible alternative for improving the efficiency of the receiver catches more interest. Increasing the number of pixels i.e. developing array receivers is an effective way, which will be elaborated later in this chapter.

1.2.2. Receiver stability

When the sensitivity of a THz receiver gets higher, it also gets more affected by the unwanted unstablizing factors, which are often unavoidable. The latter can be one

or combination of the followings: quick variations in the atmospheric condition, the slight movements of quasi-optical components, variations of LO power, instabilities of IF amplifiers and biasing systems, temperature variation, etc. The Allan time of the receiver reflects its summarized stability and determines the optimum integration time on an astronomic source. After this time, which is typically between 10 and 30 seconds, the telescope should be re-calibrated.

The random white noise integrates down by time (T) following the radiometer equation with the rate of $T^{-1/2}$ [9]. However, in practice, after a certain integration time, the present 1/f noise and then drift noise get dominated, which do not integrate down effectively. This is another indication of the Allan time. A plot depicting the Allan variance versus time is the common way to quote this behaviour. Figure 1.5 shows such a graph, in which the LO power stabilization is used to increase the receiver stability at 4.7 THz [10]. There the curves minimum points indicate the Allan times, which are 1 and 15 seconds with and without stabilization in air. By definition, the Allan time is the point, at which the noise integrates down two standard deviations slower than the rate expected from the radiometer equation as shown with dashed lines in Fig. 1.5. A 7 seconds increase in the non-stabilized Allan time using air removal (by purging nitrogen) implies the contribution of the atmospheric turbulence in the system instability.

1.2.3. THz mixers

There are some parameters that determine the merit of a typical mixer for a certain application. The first factor is the frequency, at which the mixer can function. Because of the intrinsic difficulties associated with technology development at THz there are not many mature choices available as mixers in these frequencies. The sensitivity is the crucial characteristic especially in THz astronomical observations, where the desired signal is extremely weak and overwhelmed by noise. This parameter is quoted with the noise temperature that a mixer provides in a certain receiver configuration. The other significant factor is the IF bandwidth, which defines the extent of red (blue) shift that can be detected in

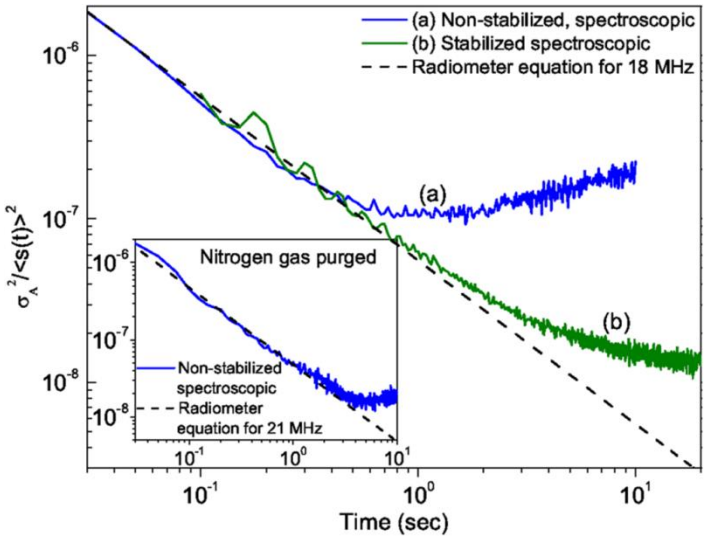

Figure 1.5. Allan variance curves measured in different conditions [10]

order to resolve the dynamics of a certain celestial object. The next influential feature of a mixer is the amount of the required LO power, extremely important in THz, where generating power is quite challenging and an independent research topic by itself. The last important property is the working temperature, which makes a great impact on the space-based and other resource-limited applications. The latter comes from the fact that having a cryogenic system burdens a big weight and power capacity requirement on a typical instrument.

Three major available THz mixer technologies are Schottky diode mixers, superconductor-insulator-superconductor (SIS) mixers and hot electron bolometer (HEB) mixers. The aforementioned characteristics for these mixers are summarized in table 1.2. Although Schottky diode mixers offer wide IF bandwidths with the room temperature operation and are available in all THz range, the poor sensitivity and high required LO power make them non-ideal for THz astronomy. SIS mixers have the best sensitivities and relatively wide IF bandwidth with low LO power requirements. However their operating frequencies are limited by their superconducting energy gap. Finally, HEB mixers can work at higher frequencies with relatively low noise and very small required LO power, although the latter

causes instability due to LO fluctuations. On the downside, their narrow IF bandwidth limits the observation efficiency.

Mixer	THz coverage	Best DSB noise temperature (× quantum noise limit)	Best IF bandwidth	Required LO power	Working temperature
Schottky diode	complete	~ 100	~ 50 GHz	0.5 – 1 mW	300 K
SIS	< 1.2 THz	~ 3	~ 10 GHz	1 – 3 μW	cryogenics
HEB	complete	~ 7	~ 6 GHz	0.1 – 0.5 μW	cryogenics

Table 1.2. Qualification factors of three major THz mixer technologies

1.2.3.1. Schottky diode mixers

In principle a Schottky diode is formed when a metal gets in contact with a semiconductor. In this situation some free electrons flow from the semiconductor to the metal, which causes imbalance in the charge distribution. The latter implies an electric field opposing further charge flow, which after equilibrium creates an electric potential difference across a certain area around the metal-semiconductor junction called depletion region. The minimum required energy for an electron to flow across this region is equal to that electric potential difference named Schottky barrier. In THz the semiconductor material is n-doped GaAs because of its important high electron mobility, essential for very high frequency operation. The thermionic emission is the dominant mechanism, through which the electrons flows across the barrier in THz frequencies, making an I-V characteristic with exponential form and enough nonlinearity for efficient mixing with high sensitivity.

THz heterodyne observations in the beginning were performed using this technology, for example on the Kuiper Airborne Observatory [11]. They can work uncooled with a large IF bandwidth efficiently throughout the THz spectrum nowadays. However they suffer from the noise dominated mostly by their intrinsic resistance and hot electrons. Cooling down lowers their noise level but not significantly [12]. On the other hand they require a powerful LO especially when they are operated at lower temperatures, which is not practically feasible at super-

THz (> 2 THz). The superconducting technology development offers far better noise-performance mixers, favourable for THz astronomy, where the sensitivity becomes extremely important.

1.2.3.2. Superconductor-Insulator-Superconductor (SIS) mixers

As it's named, a Superconductor-Insulator-Superconductor (SIS) devices is made of a thin insulating layer sandwiched by two superconducting films. The schematics and I-V characteristic of a typical SIS mixer is plotted in Fig. 1.6.

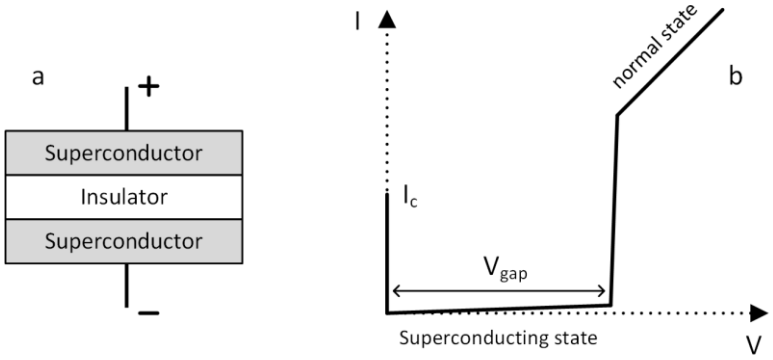

Figure 1.6. a) Geometry of SIS devices; b) Unpumped I-V characteristics of SIS devices

Without any applied bias voltage there is a sharp spike in current as depicted, called Josephson supercurrent (I_c). Because the thickness of the insulator layer is smaller than the superconductor coherence length (the maximum distance at which the electrons in a Cooper pair keep bounded) electrons on one superconductor layer can make Cooper pairs with ones on the other layer. Since the energy state of all Cooper pairs are the same they can tunnel across the insulator and form such a supercurrent. However as soon as applying a bias voltage i.e. applying a potential energy difference between superconducting layers, Cooper pairs stop sharing the same energy state and consequently the tunnelling i.e. the supercurrent stops. However in practice some leakage current always exists mainly due to thermally excited electrons with enough energy for breaking their Cooper

pairs and passing through the imperfect insulating layer. There would be ideally no current until the applied voltage reaches to a certain point at which the implied energy is enough for breaking Cooper pairs. This voltage is called energy gap voltage V_{gap} at which a sudden rise in current happens, all Cooper pairs get broken and normal resistance appears. This sharp transition between superconducting and normal states provides enough nonlinearity in the I-V curve for SIS devices to act as sensitive mixers.

The Josephson supercurrent and other sources of instabilities can be suppressed or removed by applying a certain level of magnetic field [13]. This field induces a phase difference between the wave functions of two superconductor layers and affects the extent of their overlap and consequently the supercurrent.

As shown in Fig. 1.6b, in theory, the total available voltage swinging range (including the negative voltage part) is $2V_{gap}$. This defines the maximum frequency of the incoming photons and so the maximum operating frequency of an SIS device to be $f_{max}= 2eV_{gap}/h$ ($2f_{gap}$). This limit is around 1.4 THz in commonly used Nb/Al-oxide/Nb SIS devices (Nb has an energy gap corresponding to 0.7 THz) . However, the quantum assisted tunnelling stops when the photons energy approaches to f_{max} (~ $1.7f_{gap}$), making another frequency limit. Applying NbN or NbTiN with larger energy gaps comparing to Nb could so far help to push the limit over 1.2 THz [14].

On the positive side, however, they show a superior sensitivity close to the quantum noise limit. The little required LO power together with a relatively large IF bandwidths are the other advantages of SIS mixers.

1.2.3.3. Hot electron bolometer (HEB) mixers

As named, hot electron bolometers are thermal devices, which in essence translate related conditions into their resistance behaviour through their temperature. They are made by a thin short superconducting film in between two normal metal contact pads, which is called micro-bridge. The device geometry together with the temperature profile and the I-V characteristics are shown in the top and bottom of Fig. 1.7 respectively.

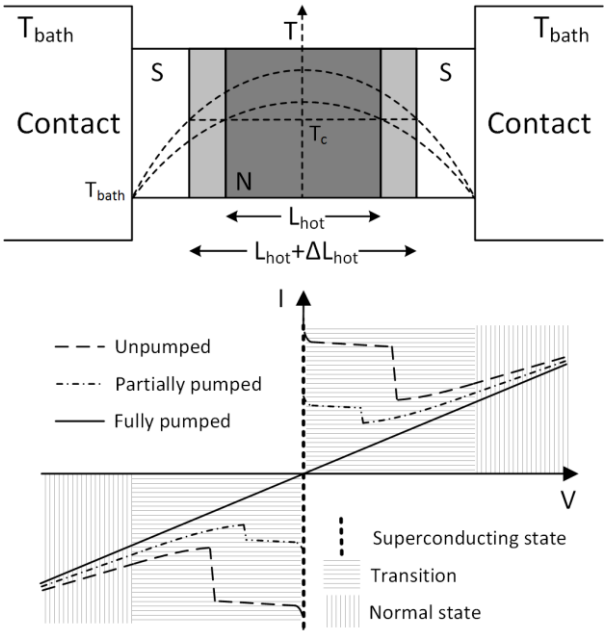

Figure 1.7. Top) Geometry and temperature profile of an HEB mixer, Bottom) I-V characteristics of an HEB device

When there is no voltage applied, the micro-bridge is purely superconductor and a supercurrent of Cooper pairs flows through. As soon as a voltage is applied, it causes Cooper pairs to break and supercurrent to stop. From this moment up to the point, where the micro-bridge gets fully resistive is referred to the nonlinear transition region. The device bias when the LO is being coupled to, should place it in a part of this region, where the resistance is positive to prevent instability. At such a bias the central part of the micro-bridge heats up and turns to the normal state while the sides are still superconductive. This central resistive region is called hotspot. When a signal is coupled to the micro-bridge the added energy increases the length of the hotspot (L_{hot}) proportional to the signal power. This change (ΔL_{hot}) is the key player in the mixing process.

The LO mixed with the desired signal are guided either quasi-optically or through waveguide to the contact pads, where they enter the micro-bridge.

Consequently the L_{hot} and hence the micro-bridge conductivity get modulated at the intermediate frequency (IF). This is often called hotspot mixing [15].

How fast the electrons can return their additional heats to the Helium bath (thermal time constant) defines the device response time and hence the IF bandwidth. HEBs are divided in two types regarding the dominant cooling mechanism of electrons, which is determined by the length of the micro-bridge and the thermal healing length [16]. The latter is the minimum distance, over which an electron travels in a micro-bridge before it returns the heat to the bath through phonon coupling to the substrate material. If the micro-bridge is longer than this length, electron-phonon coupling gets dominated and the device is called phonon-cooled HEB. Otherwise, the micro-bridge cools down dominantly by electron diffusion through the contact pads and device is called diffusion-cooled HEB. The former offers better sensitivity and the latter wider IF bandwidth.

Because of their thermodynamic nature, they have no upper-limit in the frequency of operation, unlike SIS devices, where superconducting gap sets the maximum frequency. Therefore, for the vast majority of the THz spectrum (> 1.2 THz), HEBs are the most sensitive devices requiring very low level of LO power suitable for space applications. Since the IF bandwidths of the NbN based HEBs are still limited to 4–5 GHz [17], developing new HEBs based on other superconductors like MgB_2 with demonstrated IF bandwidth of 11 GHz [18], is interesting for the community.

1.2.4. THz local oscillators

1.2.4.1. Local oscillator requirements

As introduced previously in this chapter, a local oscillator (LO) is a locally generated signal with a frequency being different from the targeted signal in an extent lying within the IF bandwidth of the employed mixer. Apart from this inherent requirement, which is determined by the mixer technology there are some other criteria that should be met by a typical LO for a space heterodyne receiver.

- **Output power:** This factor is quite critical for proper operation of a mixer and, at the same time, is the most challenging LO requirement at THz frequencies. In principle the LO power should be sufficient to switch the state of a mixer from one operating mode to the other. While superconducting mixers need level of LO powers in the order µW, Schottky diode mixers require more than 0.5 mW. One should note that there is usually a certain power loss associated with the intermediate optical setup between the LO output and the mixer input, which can be considerable e.g. ~ 90 % when a thin dielectric beam splitter is used.
- **Spectral purity:** The LO linewidth, which is proportional to its spectral (frequency/phase) stability, is an important factor in THz heterodyne spectroscopy. As defined earlier, the desired signal gets measured with respect to the LO signal as reference in the heterodyne scheme. Thus the sharper (narrower linewidth) the LO is, the more the spectral resolution would be. It is required to be at least 5 times narrower than the line under observation, whose width is set by the object velocity dispersion $\Delta\upsilon$ [1]. The latter is in the order of 1 km/s for ISM observations. By the relation $\Delta\upsilon=c(\Delta f/f_0)$, where c is the speed of light, Δf is the spectral linewidth (in Hz) and f_0 is the line frequency, for [NII] line at 1.4 THz and [OI] line at 4.7 THz for example, it requires maximum linewidths of (4.7/5) and (15.7/5) MHz respectively.
- **Intensity stability:** This factor affects the total stability of a receiver, which is mostly quoted by the term Allan time. The mixer type being used, again determines the upper limit for intensity stability of the LO. Superconducting HEB mixers are the most sensitive to the LO power fluctuations.
- **Power hungriness, dissipation and compactness:** This requirement gets more critical where the observation is not ground based i.e. air or space-based. The limited available resources do not allow to apply a power hungry nor a bulky heavy element on board. The former asks for more electrical power and sometimes cooling capacity and the latter demands higher carriage capability, both challenging and expensive up there.

Although lots of efforts have been made during the past decades to develop different types of THz sources and push the technology from both sides of the THz gap, the THz LO-qualified sources are still quite limited. The solid state electronic sources such as Gunn, Immpatt and RTD diodes and HBT and HEMT transistors suffer from the frequency upper limit induced by the carrier transient time across the structure [19]. Their powers tend to fall quickly at higher THz frequencies. Vacuum electronic sources like free electron lasers (FEL), backward wave oscillators, traveling wave tubes, klystrons and gyrotrons are in general power hungry and need strong magnetic fields in some cases. The large physical size is the other issue associated with these technologies. Whilst optically pumped far infrared (FIR) gas lasers can produce large amounts of power, their discrete frequency coverages are limited by some certain number of molecular lines as well as the fact that they are bulky and high power consuming. Indirect THz generation techniques either down-conversion e.g. difference frequency generation (DFG) and optical rectification, or up-conversion have low conversion efficiencies in THz. Nevertheless, since advances in microwave technology provide high power pumping sources and high gain amplifiers, frequency multipliers are able to deliver sufficient output powers and have been the most common THz LO sources for many years, used in different millimetre/sub-millimetre observatories. However, at super-THz (> 2 THz) they are not practically applicable both because of their low output powers and manufacturing complexities. Instead, this challenging frequency band can be covered by quantum cascade lasers, the only available LO-qualified super-THz sources.

1.2.4.2. Frequency multiplier-based sources

The nonlinearity is the working essence of frequency multiplier-based sources, which conveys microwave technology into the THz. Schottky diodes are the most established and used nonlinear elements for this purpose. Such elements essentially raise the pumping signal to powers of n (1, 2, 3, …) i.e. the frequency to multiples of n with an amplitude degradation to $1/2^{n-1}$[1]. This already shows that

the pumping signal should be so powerful to leave a workable THz signal behind after multiplication. This is available nowadays thanks to the advanced microwave sources and amplifiers.

In a THz frequency multiplier chain a continuous-wave signal in the X (8-11 GHz) or K_u (12-18 GHz) frequency band is initiated by a microwave synthesizer with a power of ~ 10-20 mW [1]. This signal then undergoes the initial multiplication and amplification steps, which lift the frequency to the W (70-110 GHz) band and the power to ~100 mW [1]. The rest of the chain consists of a few cascaded frequency multipliers to obtain the desired LO frequency. Of course the latter can be reached by proper adjustment of the synthesizer frequency and multiplication steps.

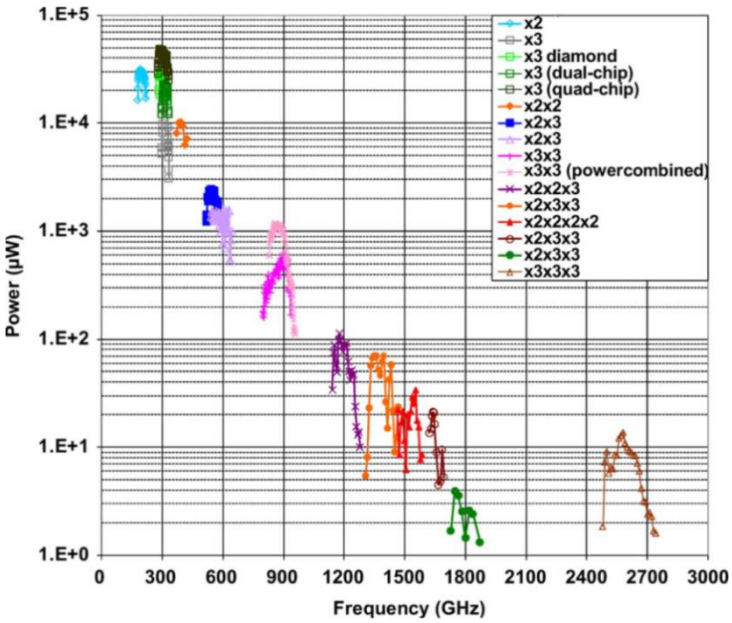

Figure 1.8. Power vs frequency for frequency multiplier-based sources with different multiplication steps [20]

Frequency multiplier-based sources deliver tens of µWs of power at lower THz frequencies in room temperature nowadays [20]. Figure 1.8 shows the power versus frequency for some such THz sources operating at room temperature with different multiplication steps [20]. Although lots of efforts are still being made to

push the frequency upper limit, their coverage up to 2 THz is practically applicable. At higher frequencies in addition to the quick power drop, the manufacturing gets much more complicated and expensive.

It should be mentioned that cooling these devices down improves their output powers through sharpening the I-V curves and consequently the up-conversion efficiencies. At 120 K the powers of 100 and 10-20 μW have been achieved at respective frequencies of 1645 [21] and 1900 GHz [22], while at the latter frequency range for example, it is in the range of few μWs at room temperature [23].

1.2.4.3. Terahertz quantum cascade lasers (QCL)

Lots of efforts have been made to develop THz quantum cascade lasers (QCL) since their emergence in 2002 [24]. Nowadays they are the only available LO-qualified super-THz sources capable of delivering tens of mWs of continuous-wave (CW) power [25]. The cryogenic cooling requirement, however, is their downside, which can be still tolerated since it is also asked often by superconducting mixers in THz heterodyne receivers. An extensive overview on such sources with regard to their suitability for space applications would be given in the next chapter.

1.2.5. THz Heterodyne array receivers

As briefly mentioned before, having receivers with sensitivities approaching to the quantum noise limit makes the construction of array (multi-pixel) receivers quite interesting for increasing the telescope observing efficiency i.e. the mapping speed. Figure 1.9 shows the mapping coverage of different array sizes considered for CCAT (Cornell-Caltech Atacama Telescope) at 650 GHz on the famous Horsehead Nebula, indicating their corresponding effects on the mapping process [26].

It should be mentioned that the amount of influence of the number of pixels (N) on the mapping speed is highly dependent on the noise temperatures of the array pixel (T_{Array}) and that of a single-pixel receiver (T_{sp}), proportional to $N(T_{array}/T_{sp})^2$ [1]. Therefore, to have a linear effect, one should keep the noise temperature

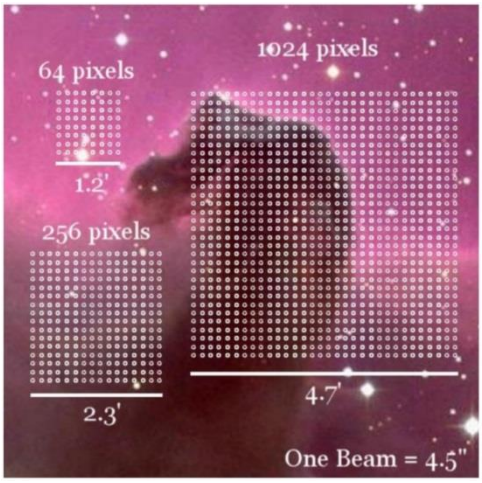

Figure 1.9. Spatial coverage of different array sizes considered for CCAT at 650 GHz on the famous Horsehead Nebula

comparable when switches from a single-pixel to an array receiver. Besides shortening the mapping time, arrays significantly reduce the manpower and operating costs associated with large-scale survey projects too [1].

The relative technology advances in all the components of the heterodyne receivers e.g. mixers, LOs and IF amplifiers together with developments in micromachining and packaging have allowed sub-THz (< 1 THz) arrays to be demonstrated [27-29]. However, challenges at higher THz frequencies in a practical instrument e.g. array LOs and high power dissipation of low noise cryogenic IF amplifiers have kept the state-of-the-art THz heterodyne receiver arrays having in the order of 10 pixels.

1.2.5.1. THz phase gratings for array local oscillators

Making a THz multi-beam LO can be done using waveguide-based power splitters in combination with frequency multiplier-based sources [30], where the initial microwave signal first gets split and then multiplied in sequential steps. Here the problem of the manufacturing complexity again arises and does not let this technology be practical at super-THz. Figure 1.10 shows a photograph of a 4-pixel, 1.4 THz LO developed by JPL [30].

Combining THz QCLs with waveguide splitters is non-practical because of the challenges in beam coupling and also potential waveguide losses. Employing multiple THz QCLs working in parallel to act as an array LO is hardly applicable since the limited accuracy of the lithography makes it too challenging to have several QCLs exactly identical in frequency. On the other hand, frequency/phase locking of multiple THz QCLs is also quite complex. Here multiplexing the beam of a THz QCL with certain criteria is highly desirable.

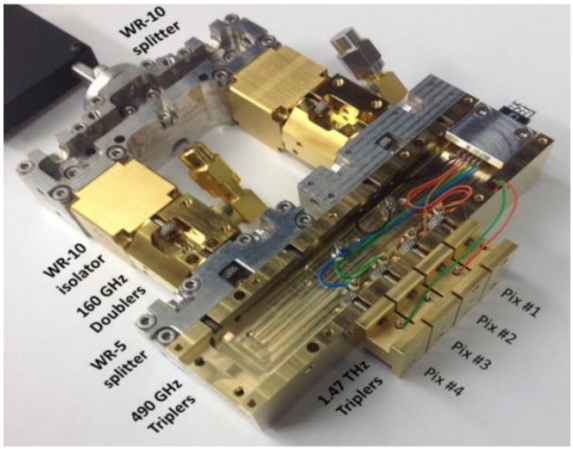

Figure. 1.10. Photograph of a 4-pixel 1.4 THz LO [30]

A phase grating in general is a periodic structure (each period is called a unit cell), which modulates the phase of the incident electromagnetic field in a way to make a series of diffraction orders with a certain configuration in the far-field [31]. These devices are highly scalable to make an LO array of many pixels if sufficient input power is available. Because of the high level of THz absorption losses in dielectrics, THz phase gratings should be made in the reflection (not transmission) mode. In this fashion a single input beam illuminates the grating surface, which dominantly diffracts the desired orders and makes a multi-beam far-field pattern. With this principle, diffracted beams have the same shape as the input, when it is flipped regarding the incident beam's orientation. The key figure of merit of such beam dividers is the diffraction efficiency defined as the ratio between the total power of the resulting multiple beams and that of the input single beam.

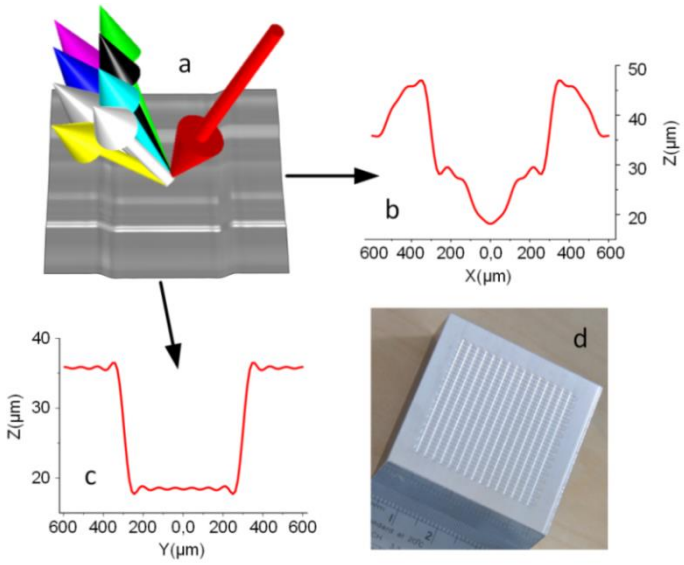

Figure 1.11. a) schematic of the operating principle of an 8-pixel reflective Fourier phase grating; b,c) unit cell orthogonal cross section profiles; d) a photograph of the phase grating

A reflective phase grating can be made by a very high reflective metal e.g. gold or aluminium, which gets patterned by direct milling. Traditional Damman gratings [32] with stepwise profiles are very hard to fabricate because of serious challenges in milling the right corners. The smooth and continuous surfaces of Fourier phase gratings [33] instead can be relatively accurately machined nowadays. However, the minimum radius of curvature that can be handled is still limited and should be concerned. The unit cell surface topology in a Fourier phase grating is derived through a Fourier series with a certain number of applied coefficients. In principle, a higher number of coefficients leads to a higher efficiency. Apart from the unit cell proper surface morphology, its size should be also carefully adjusted. The latter determines the divergence of the whole far-field pattern and consequently affects the rest of the optical system after the grating. A schematic of the working principle of an 8-pixel (4×2) Fourier phase grating together with typical orthogonal cross section profiles of a unit cell and the grating photograph are shown in Fig. 1.11. Each of the two orthogonal profiles is responsible for a certain multiplication

(*m* and *n*), which after superimposing gives the whole (with $m \times n$ beams) beam pattern.

The diffracted beams by the grating then usually get collimated quasi-optically such to match the beams of a mixer array. A considerable fraction of this thesis (chapters 5 and 6) is dedicated to the development of THz phase gratings with the ultimate purpose of the array LO demonstration at [OI] line frequency of 4.7 THz using a QCL as the prototype LO unit for GUSTO's higher frequency channel.

1.3. THz incoherent detectors

For many astronomical observations including dust in the ISM, external galaxies and cosmic background, having very high spectral resolution is not necessary. This means that there is no need for retaining the phase information of the incoming photons (incoherence) as it is in coherent detectors. An incoherent detector system consists typically of a filtering section to pick the desired frequency range to be observed, a detector with an output voltage proportional to the incident power, and an amplification section, all placed in a shared cryostat. Because the signal is detected without the contribution of any other reference signal, this method is also called direct detection. The measure for a direct detector sensitivity is typically quoted based on its noise equivalent power (NEP) in $W/Hz^{1/2}$, which is the signal power required for a signal-to-noise ratio equal to one in a 1-Hz output bandwidth. THz Incoherent detectors are in three major types of semiconductor bolometers, transition edge sensors (TES) and microwave kinetic inductance detectors (MKID), where the last two are based on the superconductivity.

Semiconductor bolometers convert the photons energies into heat using an absorbing layer, which changes the resistivity of a thermally contacted semiconductor thermometer. The latter, which is a doped semiconductor at very low temperatures (<5 K), is called a bolometer. The bolometer is biased by a constant current so that any change in its resistivity shows up in its voltage that can be amplified and detected. Having NEPs of ~ 6×10^{-17} $W/Hz^{1/2}$ they have been

applied in the first THz bolometer array, SCUBA (Submillimetre Common-User Bolometer Array) with 131 composite germanium bolometers [34].

Superconducting technology later introduced detectors with higher sensitivities and array compatibilities. TES is a piece of superconductor, voltage-biased in its transition region between zero resistance superconductivity and a normal conductor. Here a tiny incoming energy i.e. photons cause a jump in its resistance, which can be red-out efficiently using an SQUID (Superconducting Quantum Interface Device). They have been applied in large arrays like SCUBA-2 with 10000 pixels [35]. Figure 1.12 shows an SEM photo of a state-of-the-art TES developed by SRON with an NEP in the order of 10^{-19} W/Hz$^{1/2}$ [36].

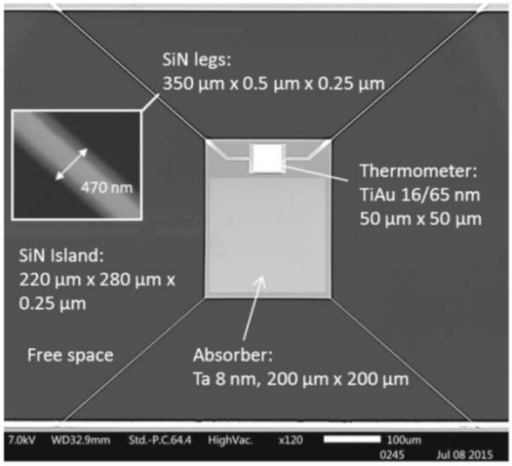

Figure 1.12. SEM photo of an TES developed by SRON [36]

MKIDs rely on the change of the kinetic inductance and resistivity of a superconductor when photons are absorbed by. Putting the superconductor in parallel with a fixed capacitor makes a resonant circuit, in which the resonance frequency (f_r) changes by the change of the superconductor inductance. The schematics of the MKID together with its resonance behaviour are plotted in Fig. 1.13 [37]. The size of the fixed capacitor is chosen to give an f_r at microwave range (as in the detector's name). Besides the change in the f_r , the resistivity change

makes the resonant dip broader and shallower. These two probes are used to accurately determine the incident power.

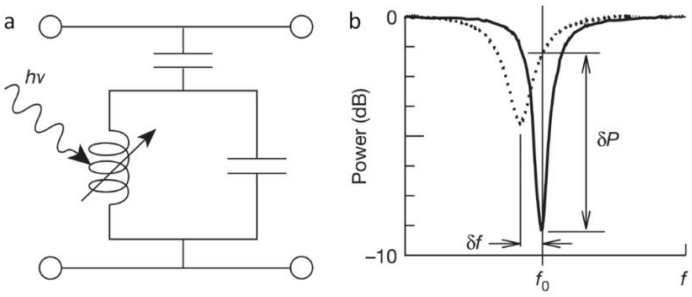

Figure 1.13. a) Schematic of an MKID; b) resonance response of an MKID in presence of incoming photons [37]

The fabrication simplicity allows making thousands of MKID pixels on a single substrate, each with a different resonant frequency, which are red-out using frequency domain multiplexing through a single transmission line and a single cryogenic low noise amplifier [38]. The NEP of ~ 3.8×10^{-19} W/Hz$^{1/2}$ has been achieved for MKIDs [39], comparable with TES devices.

1.4. Thesis outline

In this thesis the adaptation of THz QCLs for LO applications in heterodyne receivers is studied including their frequency locking in a new setup with the aim of taking full advantage of the available output power, their post-processing frequency tuning and their beam multiplexing desired for array receivers.

Chapter 2: This chapter is the introduction and overview on THz QCLs and achieved milestones towards their modification for space LO applications.

Chapter 3: Frequency locking of a 3.5 THz third-order DFB QCL using the radiation from both directions is reported in this chapter for the first time. Being able to take full advantage of the generated output power of the laser is the main massage, which has been implied in a frequency locking scheme; one direction for locking and the other for quality monitoring.

Chapter 4: Tuning the frequency of third-order DFB THz QCLs as a post-processing step is studied in this chapter. It investigates an easy-to-do adjustment technique to compensate the frequency deviation of fully processed THz QCLs due to the limited accuracy of the lithographical process or unexpected frequency drifts. Altering the laser surroundings by deposition of dielectrics in order to change the effective modal index is the essence.

Chapter 5: Preparing a platform for THz beam multiplexing, necessary for developing multi-beam LOs for array heterodyne receivers is accomplished and reported in this chapter. A Fourier phase grating operating at 1.4 THz is demonstrated for the first time. The performance is evaluated experimentally using a far-infrared gas laser and by 3D simulations. This work is a proof of concept, opening the path towards super-THz, where THz QCLs are the only applicable LOs.

Chapter 6: An array LO at astronomically significant frequency of 4.7 THz is demonstrated in this chapter for the first time. The combination of a phase grating and a THz third-order DFB QCL makes an 8-pixel rectangularly configured LO. The system full characterisation including the far-field beam pattern, diffraction efficiency, operation bandwidth and power distribution uniformity is performed both experimentally and by 3D simulations. An study on the grating manufacturability is given too. Finally the QCL power requirement is analysed using a superconductor mixer.

The demonstrations and achievements in this thesis open up multiple new ways and possibilities for practically incorporating THz QCLs into heterodyne receivers. While the given material provides a practical toolbox in general for LO application of THz QCLs, the chapters 4 and 5 are the steps towards realization of the LO unit for the higher frequency channel (4.7 THz) of NASA science mission GUSTO (Galactic/X-galactic Ultra-duration-balloon Spectroscopic/Stratospheric Terahertz Observatory). The latter is scheduled to launch in 2021 from Antarctica and map three THz fine structured lines including [OI] at 4.7 THz in our galaxy using an 8-pixel receiver array.

Bibliography

[1] C. Walker, “Terahertz Astronomy,” (CRC, Taylor & Francis Group, 2016), Chap. 5&6.

[2] B. C. Henderson and J. A. Cook, “Image-reject and single-sideband mixers,” Watkins-Johnson Tech-Notes (1985).

[3] B. Billade, “Mixers, multiplier and passive components for low noise receivers,” PhD dissertation, Chalmers University of technology (2013).

[4] A. Kerr and S. Pan, “Design of planar image separating and balanced SIS mixers,” in Proceedings of the 7th international symposium on space terahertz technology, Charlottesville (1996).

[5] E. C. Sutton, “Observational astronomy: techniques and instrumentation,” (Cambridge University press, 2011), Chap. 12.

[6] E. Kollberg and S. Yngvesson, “Quantum noise contribution to the receiver noise temperature of HEB heterodyne receivers,” in Proceedings of the 13th international symposium on space terahertz technology, Harvard (2002).

[7] H. Callen and T. Welton, “Irreversibility and generalized noise,” Phys. Rev. **83**(1), 34 (1951).

[8] W. Zhang, P. Khosropanah, J. R. Gao, E. L. Kollberg, K. S. Yngvesson, T. Bansal, R. Barends and T. M. Klapwijk, “Quantum noise in a terahertz hot electron bolometer mixer,” Appl. Phys. Lett. **96**, 111113 (2010).

[9] D. J. Hayton, J. R. Gao, J. W. Kooi, Y. Ren, W. Zhang and G. de Lange, “Stabilized hot electron bolometer heterodyne receiver at 2.5 THz,” Appl. Phys. Lett. **100**, 081102 (2012).

[10] J. L. Kloosterman, D. J. Hayton, Y. Ren, T. Y. Kao, J. N. Hovenier, J. R. Gao, T. M. Klapwijk, Q. Hu, C. K. Walker and J. L. Reno, “Hot electron bolometer heterodyne receiver with a 4.7-THz quantum cascade laser as a local oscillator,” Appl. Phys. Lett. **102**, 011123 (2013).

[11] R. T. Boreiko and A. L. Betz, “Ionized carbon in the large magellanic cloud,” Ap. J. 380, 27 (1991).

[12] H. W. Hubers, “Terahertz heterodyne receivers,” IEEE J. Select. Top. Quant. Electron. **14**(2), 378 (2008).

[13] A. Barone and G. Paterno, “ Physics and applications of the Josephson effect,” (John Wiley & Sons, 1982).

[14] A. Karpov, D. Miller, F. Rice and J. Zmuidzinas, “Low noise 1.2 THz SIS receiver,” in Proceedings of the 12th international symposium on space terahertz technology, San Diego (2001).

[15] D. W. Floet, E. Miedema, T. M. Klapwijk and J. R. Gao, "Hotspot mixing: A frame-work for heterodyne mixing in superconducting hot-electron bolometers," Appl. Phys. Lett. **74**, 433 (1999).

[16] W. Skocpol, M. Beasley and M. Tinkham, "Self-heating hotspots in superconducting thin-film microbridges," J. Appl. Phys. Lett. **45**, 4054 (1974).

[17] S. Cherednichenko, V. Drakinskiy, T. Berg, P. Khosropanah and E. Kollberg, "Hot-electron bolometer mixers for the Herschel space observatory," Rev. Sci. Instrum. **79**, 034501 (2008).

[18] E. Novoselov and S. Cherednichenko, "Low noise terahertz MgB_2 hot-electron bolometer mixers with an 11 GHz bandwidth," Appl. Phys. Lett. **110**, 031601 (2017).

[19] H. Kanaya, et al, "Fundamental oscillation up to 1.42 THz in RTD by optimized collector spacer thickness," J. IR MM THz Waves **35** (5), 425 (2014).

[20] G. Chattopadhyay, "Technology, capabilities and performance of low power terahertz sources," IEEE Trans. Terahertz. Sci. Technol. **1**(1), 33 (2011).

[21] A. Maestrini, J. S. Ward, H. Javadi, C. Tripon-Canseliet, J. Gill, G. Chattopadhyay, E. Schlecht and I. Mehdi, "Local oscillator chain for 1.55 to 1.75 THz with 100 µw peak power," IEEE Microw. Wireless Compon. Lett., **15**(12), 871 (2005).

[22] I. Mehdi, G. Chattopadhyay, E. Schlecht, J. Ward, J. Gill, F. Maiwald and A. Maestrini, "Terahertz multiplier circuits," in IEEE MTT-S Int. Microw. Symp. Dig., 341–344 (2006).

[23] T. W. Crowe, J. L. Hesler, D. W. Porterfield, D. S. Kurtz and K. Hui, "Development of multiplier based sources for up to 2 THz," in Joint 32nd Int. Infrared Millimeter-Waves Conf. /15th Int. Terahertz Electron. Conf., 621–622 (2007).

[24] R. Köhler, A. Tredicucci, F. Beltram, E. H. Beere, E. H. Linfield, A. G. Davies, D. A. Ritchie, R. C. Iotti and F. Rossi, "Terahertz semiconductor-heterostructure laser," Nature, **417**, 156 (2002).

[25] B. Williams, S. Kumar, Q. Hu and J. Reno, "High-power terahertz quantum-cascade lasers," Electron. Lett., **42**(2), 18 (2006).

[26] C. Walker, C. A. Kulesa, C. Groppi and D. Golish, "Future prospects for terahertz spectroscopy," in Millimeter and submillimeter detectors and instrumentation for astronomy IV, France (2008).

[27] C. Walker, et al, "PoleStar: A 4-pixel 810 GHz array receiver for AST/RO," in Proceedings of the 12th international symposium on space terahertz technology, San Diego (2001).

[28] C. Groppi, C. Walker, C. K. Kulesa, D. Golish, A. S. Hedden, P. Gensheimer, G. Narayanan, A. W. Lichtenberger, U. U. Graf and S. Heyminck, "DesertSTAR: a 7 pixel 345 GHz heterodyne array receiver for the Heinrich Hertz Telescope," in Millimeter and Submillimeter Detectors for Astronomy (2003).

[29] C. Groppi, et al, "SuperCam: A 64 pixel heterodyne array receiver for the 350 GHz atmospheric window," in Proceedings of the 20th international symposium on space terahertz technology, Charlottesville (2001).

[30] J. V. Siles, R. H. Lin, C. Lee, E. Schlecht, A. Maestrini, P. Bruneau, A. Peralta, J. Kloosterman, J. Kawamura and I. Mehdi, "Development of High-Power Multi-Pixel LO Sources at 1.47 THz and 1.9 THz for Astrophysics: Present and Future," in Proceedings of the 26th International Symposium on Space Terahertz Technology, Cambridge, MA, (2015).

[31] J. A. Murphy, C. O'Sullivan, N. Trappe, W. Lanigan, R. Colgan, and S. Withington, "Modal Analysis of the Quasi-Optical Performance of Phase Gratings," Int. J. Inf. Mill. Waves **20**(8), 146 (1999).

[32] H. Dammann, and E. Klotz, "Coherent optical generation and inspection of two-dimensional periodic structures," Int. J. Opt. **24**(4), 505 (1977).

[33] U. U. Graf, and S. Heyminck, "Fourier gratings as submillimeter beam splitters," IEEE Trans. Antenn. Propag. **49**(4), 542 (2001).

[34] W. Holland, et al, "SCUBA: A common-user submillimeter camera operating on the James Clerk Maxwell Telescope, http://arxiv.org/abs/astro-ph/9809122 (1998).

[35] W. Holland, et al, "SCUBA-2: The 10000 pixel bolometer camera on the James Clerk Maxwell Telescope," https://arxiv.org/abs/1301.3650 (2013).

[36] P. Khosropanah, et al, "Ultra-low noise TES bolometer arrays for SAFARI instrument on SPICA," Proc. SPIE 9914, 99140B (2016).

[37] P. K. Day, H. G. Leduc, B. A. Mazin, A. Vayonakis and J. Zmuidzinas, "A broadband superconducting detector suitable for use in large arrays," Nature, **425**(6960), 817, (2003).

[38] J. Rantwijk, M. Grim, D. Loon, S. Yates, A. Baryshev and J. Baselmans, "Multiplexed Readout for 1000-Pixel Arrays of Microwave Kinetic Inductance Detectors," IEEE Trans. Microw. Theory Tech. 64(6), 1876 (2016).

[39] P. de Visser, J. Baselmans, J. Bueno and T. M. Klapwijk, "Demonstration of an NEP of 3.8×10^{-19} W/Hz$^{1/2}$ at 1.54 THz in multiplexible superconducting microresonator detectors," in 39th IRMMW-THz, Tucson, AZ (2014).

2

THz QUANTUM CASCADE LASERS TOWARDS LOCAL OSCILLATOR QUALIFICATION

A brief overview on THz quantum cascade lasers (QCLs) is given in this chapter from their working principles to their advancements towards qualification as local oscillators for space applications. The state-of-the-art THz QCLs based on the third order DFB technology, which has been applied in the work of this thesis are introduced and described in this chapter too.

2.1. Up-to-date status of THz QCLs

Quantum cascade lasers (QCL) are the only compact, high power, low-consumption and spectrally pure semiconductor sources, which are able to operate over a wide THz frequency band from 1.2 to 4.9 THz [1]. Although the state-of-the-art output powers are over 1 W in pulsed operating mode [2] and 130 mW in continuous wave (CW) [3], such high power QCLs may not be practical for LO applications in other senses. The required cryogenic operating temperature has been their main remaining challenge till now. 199 and 129 K are the operating temperature records respectively for pulsed [4] and CW [5] modes. Figure 2.1 shows the state-of-the-art operation temperatures of THz QCLs with different designs of the gain medium (will be explained later in this chapter) [6].

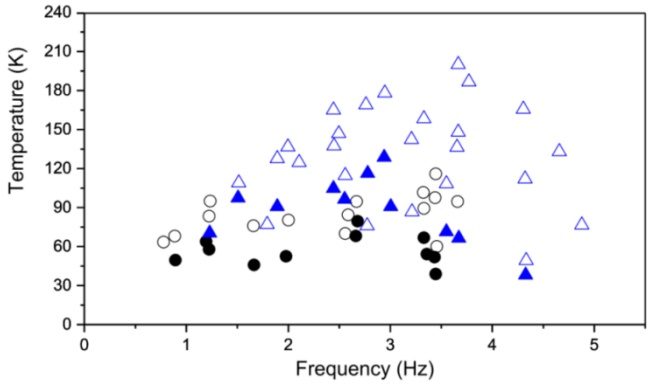

Figure 2.1. Maximum operating temperatures of THz QCLs with different gain mediums. Solid and open symbols refer to CW and pulsed operating modes respectively. Circles and triangles refer to the bound-to-continuum and resonant-phonon gain mediums respectively [6]

2.2. Gain medium (active region)

Electrically biased stack of quantum wells (QWs) is the building blocks of quantum cascade lasers. It is made by molecular beam epitaxy (MBE) growth process, in which the layer thicknesses can be as small as atomic layers and accurately controlled. The quantized energy states in QWs, called sub-bands, play the role of

staircase steps for electrons to flow through (like a cascade) via quantum tunnelling, and emit radiation in each transition between the upper and lower radiative levels (URL and LRL respectively). That is why they are called inter-sub-band (ISB) lasers too. Figure 2.2 depicts such working principle. This medium, in which the gain is produced is called gain medium or active region. It consists of a number of periods (*N*), in each the electrons emit radiation (radiation part) and get injected to the same position of the next period (injection part) to repeat the same process. This leads to generation of *N* photons per electron, which boosts the device output power since N is typically as large as 200.

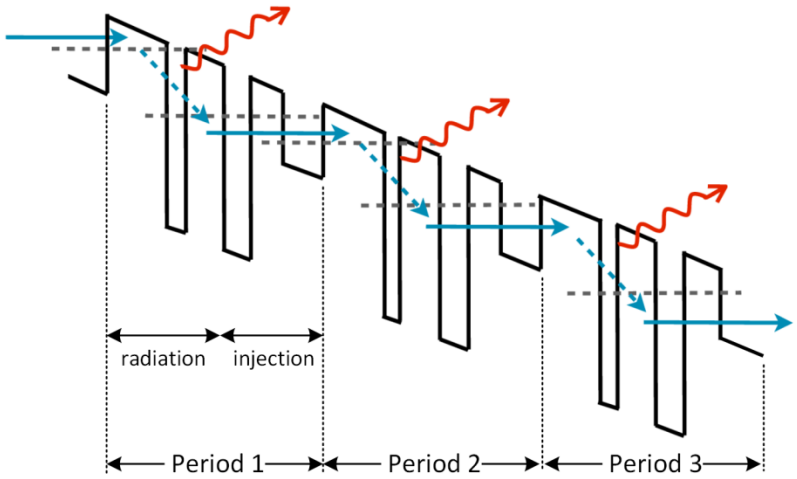

Figure 2.2. The gain medium (active region) in QCLs. Each electron produces a photon in each period and gets injected to the next period to do the same

Proper arrangement of quantum wells with appropriate thicknesses is the way to engineer the structure and determine the emission frequency, which is proportional to the energy difference between radiative sub-bands. Since the latter can be sufficiently small, THz radiation can be achieved, unlike the inter-band conventional QW lasers, where the lower limit of the radiation frequency is defined by the material band-gap (in the order of 1 eV).

In order to partially deactivate the unwanted electron scattering mechanisms, which appear due to the high closeness of the radiative levels and degrade the population inversion, and make a clear flowing path for carriers throughout the active region, the temperature should be considerably lowered, usually to cryogenics. Enhancing the operating temperature of THz QCLs is still the biggest challenge the community faces.

GaAs/AlGaAs material system has shown the best characteristics suitable for THz QCLs e.g. small effective mass of electrons (0.06), favourable for higher optical gain at THz [4]. The other drive to keep using this material is the fact that its growth technology is very well established.

The most important requirement for achieving sufficient population inversion for lasing is the rate, at which the lower radiative level (LRL) gets evacuated of carriers. In other words the faster the extraction of carriers from the LRL, the larger population inversion and the larger gain. This factor has been the main challenge, for which lots of efforts and research have been done to overcome and enable the QCLs active regions for THz radiation. In two of three major resulting structures i.e. chirped superlattice [7] and bound-to-continuum [8], a band of closely spaced energy levels (maniband) is used for the electron to leave the LRL towards, instead of a single energy level. This trick, which was used in the first demonstrated THz QCL [7], increases the electrons tendency to minimally stay at the LRL. The other solution, based on which the highest operating temperature THz QCL works [4], uses the ultra-fast interaction between electrons and longitudinal optical phonons (LO-phonon) to empty the LRL. This is called resonant-phonon depopulation scheme [9], in which the energy space between the LRL and the next level is exactly equal to the LO-phonon energy of the applied material system (~ 36 meV for GaAs). Figure 2.3 simply illustrates these two techniques [10].

It has been shown that the intrinsic linewidth of THz QCLs is as narrow as 110 Hz [11], originated from the delta-like shape of the gain spectrum in the inter-sub-band lasers. However, the instabilities in the biasing system and temperature

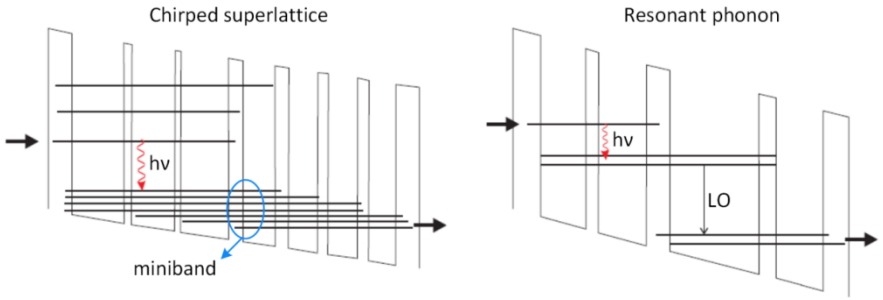

Figure 2.3. Two dominant schemes of quantum well structures applied in the gain medium of THz QCLs [10]

fluctuations usually broaden the linewidth up to hundreds of kHz and even to MHz. Although a THz QCL in its free running mode can still be used as an LO for detecting sufficiently wide spectral lines, a frequency or phase stabilization mechanism needs to be applied for a more reliable observation. The frequency stabilization can be performed in the lab by locking the QCL frequency to an external reference, e.g. a frequency multiplied source [12] or to a molecular absorption line [13]. Despite of promising results however, these methods are not easily applicable in space because of their associated bulky components and high-consumption electronics. Instead, a superlattice diode acting as both source and mixer can be applied [14].

2.3. Waveguide

Parallel to the active region development, the waveguide structure to confine the radiation and providing optical feedback has been under extensive research too. Using conventional dielectric waveguides for confining such long wavelength radiation requires impractically thick cladding layers (> λ/2). Therefore the plasmon waveguides should be applied. In the latter, only one transverse magnetic mode (TM) is supported to propagate at the interface between two materials with positive and negative real parts of the dielectric constant. The fact that the free carrier absorption losses dramatically increase by the wavelength ($\alpha_{\text{free carrier}} \propto \lambda^2$) makes another constraint. Nowadays two dominant waveguide structures for THz

QCLs are widely used, semi-insulating (SI) surface plasmon and metal-metal waveguides. Their schematics and mode confinement are shown in Fig. 2.4.

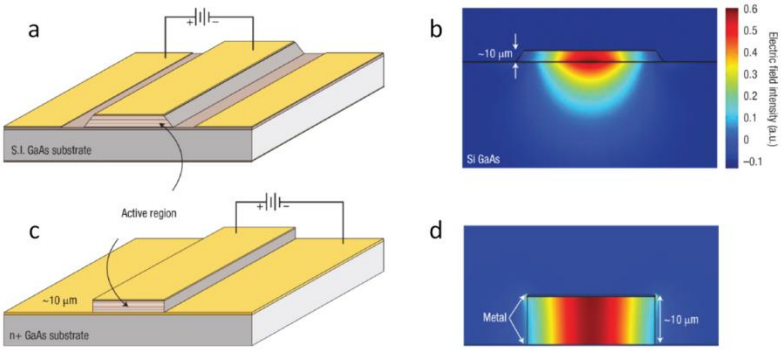

Figure 2.4. Schematics of the SI surface plasmon (a) and metal-metal waveguides together with their corresponding mode confinements (b,d)

In a SI surface plasmon waveguide [2] the QCL active region is grown on a SI substrate of GaAs for example, where a very thin (< 1 µm) heavily doped ($GaAs^{++}$) contact layer is lying in between. The top side of the active region is coated by a metal like gold. Since at THz, the real part of the dielectric constants of the metal and $GaAs^{++}$ are negative, the TM surface plasmon modes confined between these layers i.e. the active region, propagates. The mode intensity across the active region is relatively uniform because of its sub-wavelength thickness. It however strongly leaks out to the substrate but with a minimized overlap with the very thin $GaAs^{++}$ contact layer and thus a minimized absorption (< 5 cm^{-1}). Such a leakage leads to a small (< 0.5) mode confinement factor in the active region (Γ). Since the laser gain threshold is defined by $(\alpha_w+\alpha_m)/\Gamma$, where α_w and α_m are the waveguide absorption and the mirror loss due to the finite reflectivities of the laser facets respectively, a reasonable compromise between α_w and Γ should be made. The loose mode confinement has several influences on the operation of such waveguides. First, it allows to have wide ridges (~ 200 µm) for increasing the power without appearance of the multi-mode operation. Second, it limits the minimum ridge width to about 100 µm [15], since the mode gets squeezed into the substrate

when the ridge is narrower. And third, it makes the far-field beam of such lasers less divergent as a result of the large emission area.

In a metal-metal waveguide [16] the active region is sandwiched between two thin metallic layers e.g. gold. Since the gold skin depth is so small at THz and its plasma frequency is far away enough from the radiation frequency, it makes a very low loss waveguide with a close to unity confinement factor. The latter allows scaling down the ridge width to sub-wavelength dimensions with great impact on the thermal dissipation and so the operation temperature. This feature makes them the only waveguides operating in CW mode at temperatures more than 100 K [5]. However, the need for flip-chip wafer bonding technology makes its processing relatively complex.

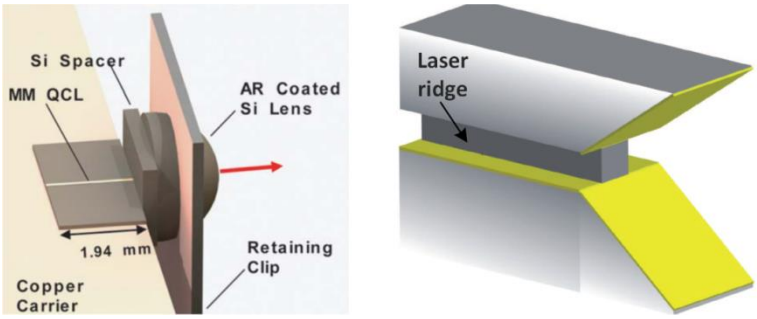

Figure 2.5. The application of a mounted lens (left) [17] and a horn antenna (right) [18] for correcting the far-field beam shape of the metal-metal waveguides

Because of the sub-wavelength mode confinement in metal-metal waveguides, the mode inside the laser sees a big impedance mismatch to the free space propagating modes, which causes a high facet reflectivity and so a low out-coupling efficiency. The latter however lowers the mirror loss, which together with the lower waveguide loss decrease the device threshold current density and subsequently increase the operating temperature. The most unwanted result of such poor extraction efficiency is a non-directional (divergent) diffractive far-field beam, unusable as an LO. Several approaches have been taken to address this

beam shape issue such as employing facet mounted lenses [17] and horn antennas [18] shown in Fig. 2.5.

2.4. Single-mode emission and directional beam pattern

It should be noted that a QCL based on Fabry-Perot cavity typically radiates a multi-mode beam mainly due to the spatial hole burning effect [19]. While the aforementioned techniques relatively correct the beam shape of the metal-metal waveguide THz QCLs, the multi-mode emission issue also has to be overcome to make the device capable for acting as an LO as well as many other applications. Applying a periodic structure to only let the desired mode resonate (single-mode operation), is the dominant solution, which has ended up with two major approaches, distributed feedback structures (DFB) and two dimensional (2D) photonic crystal cavities (PCC) [20,21].

As it is schematically shown in Fig. 2.6a, in a 2D PCC structure the top metallization of the laser active region is patterned with a photonic crystal design acting as a resonator to select the desired emission frequency, while the light at the same time gets vertically diffracted [20]. An optical microscope image of the surface of a PCC THz QCL [21] together with its far-field beam pattern are depicted in Fig. 2.6b and c. The latter shows a promising Gaussian-like beam with a divergence as low as 10° × 10°.

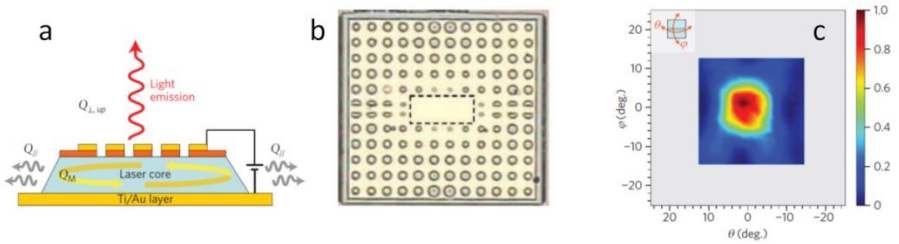

Figure 2.6. a) Schematic of the PCC structure and operation [20]; b,c) An image of an PCC THz QCL together with its far-field beam pattern [21]

Despite of their outstanding directional far-field beam patterns, the 2D PCC-based THz QCLs are not favourable for LO application. The dominant reason comes from their large surfaces (gain medium) with large required operating currents and thus high power dissipations (> 20 W) [21], both forbidden in a space instrument with limited electrical power and cooling capacity.

Although the first-order DFB technique is the easiest for single-mode emission, because of the lack of an out-coupling mechanism the radiation comes out from the laser end facets. Therefore, it does not improve the beam shape of the metal-metal waveguides [22]. Applying the second-order DFB structure, which vertically couples the radiation out, is a way for having a single-mode beam with an improved far-field pattern. However, the beam pattern improvement is limited to the direction parallel to the ridge axis and thus still highly divergent in the perpendicular direction [23]. Shaping such second-order DFB structures to a ring or putting couple of them in a phase-locked array relatively moderates this issue but not satisfactorily [24,25]. Figure 2.7 shows some SEM photos of the first and second-order DFB structures, the ring cavity and the phase-locked array techniques.

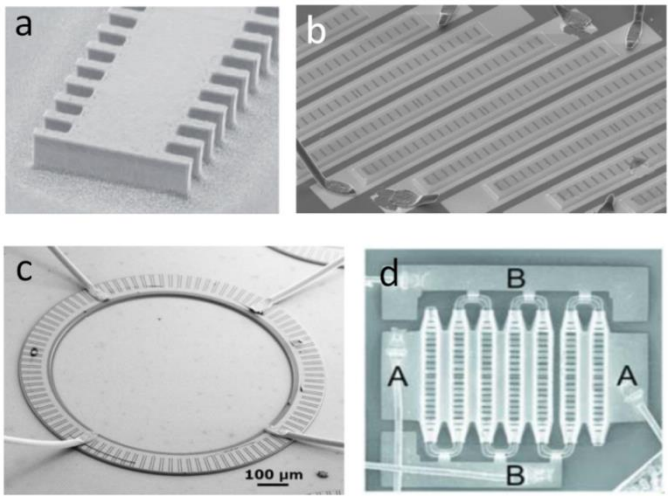

Figure 2.7. SEM photos of the first (a) [22] and second-order (b) [23] DFB structures, the ring cavity (c) [24] and the phase-locked array [25] techniques

2.4.1. Third-order DFB THz QCLs

The most promising waveguide structure for LO application is the third-order DFB, first demonstrated in 2009 by Amanti et al [26]. As shown in Fig. 2.8a, such a system in the simplest way can be explained as a structure consisting of many periods, each acting as a single oscillator. Careful adjustments of the period length and the modal effective index (n_{eff}) make the radiation from all the periods constructively interfering along the laser length in both directions. In other words, the electromagnetic wave inside the structure is phase-matched to the free space radiation flowing on the laser surface, at each radiation slit. Therefore, the beam is expected to have a very low divergence and a single spot beam pattern in the far-field.

Essentially, such a constructive interference (phase matching) happens perfectly if the free space wavelength (λ_0) is an odd multiple of the one propagating inside the laser. Thus, 3 should be aimed as the modal index since larger odd numbers are not reachable when GaAs based active regions are used. Because the GaAs refractive index is about 3.6, it has been however so challenging so far to reduce the n_{eff} to below 3.2 [26]. This deviation from 3 makes the interference less and less constructive at radiation slits farther and farther from the structure centre. From a certain point on, the resulted far-field pattern gets out of interest for a specific application. The maximum length, beyond which the beam pattern begins to deteriorate and the output power decreases is called coherence length. The latter is 16Λ (Λ is the period length)for n_{eff} = 3.2.

An effective technique to further reduce the n_{eff} is referred to the perfectly phase-matched third order DFB [27]. In this technique the structure is designed such that the n_{eff} finds a minor dependence on the gap size between adjacent periods i.e. another degree of freedom. Having adjusted the n_{eff} to 3, one can make a much longer structure leading to more beam directionality and power. When 151 periods are employed, the resulting beam pattern has a divergence as low as 6° × 11°. On the bottom raw of Fig. 2.8 the far-field beam patterns of THz QCLs with

metal-metal (c) [28], third order DFB (d) [29] and perfectly phase-matched DFB (e) [27] waveguide structures can be compared, where a great trend of progress is visible.

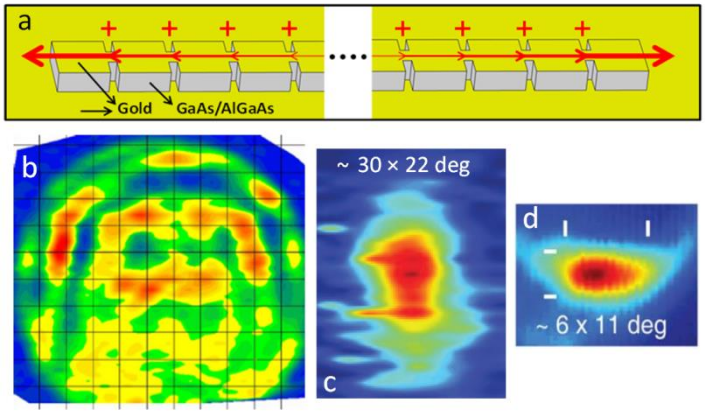

Figure 2.8. a) An schematic of the third-order DFB QCLs; b-d) Respective far-field beam patterns of metal-metal [28], third-order DFB [29] and perfectly phase-matched third-order DFB [27] THz QCLs

A unique feature of narrow metal-metal based THz QCLs is the fact that the electromagnetic field is extended to the free space from the bare lateral sides of the structure. The reason is the subwavelength lateral dimension of the waveguide. A full 3D FEM modelling has been performed by the author for illustration of this effect in third-order DFB structures. The results are shown in Fig. 2.9, where the field out-extended portion can be seen in 3D and top views. This accessible field outside the structure gives some unique opportunities as will be explained in the following paragraphs.

The resonant frequency in third order DFB QCLs can be derived in theory by the expression $f = 3c/2n_{eff}\Lambda$, where c is the speed of light in vacuum. However, it is almost impossible to get it exactly right in the aimed frequency region because of the limited accuracy of the lithographical step in the fabrication. Therefore, a post processing tuning mechanism is quite beneficial, which can actually be realized by manipulation of the n_{eff}. Whilst changing the device temperature (either directly or

by changing the current) gives a quite limited tuning range based on such principle [30], altering the structure surroundings, where the extended field can sense, does the job effectively. Different ways can be applied to do so e.g. approaching an external metallic plunger to the laser side [31] (not easily applicable in space) and dielectric deposition. The latter has been extensively studied in the chapter 4 of this thesis, where more than 13 GHz shift has been achieved by applying a layer of SiO_2.

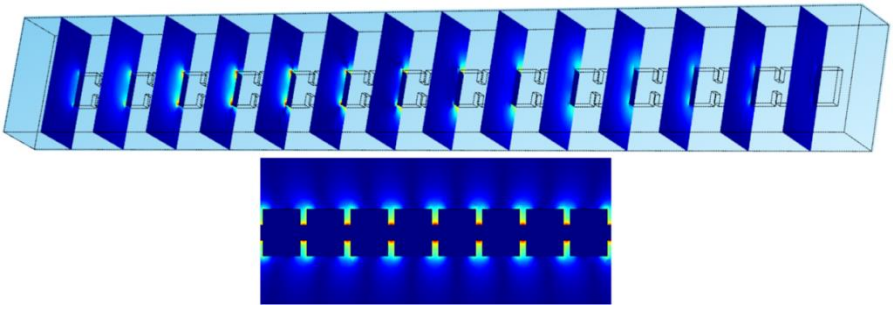

Figure 2.9. 3D (top) and top (bottom) views of the field lateral out-extended portion in third-order DFB QCLs

As previously mentioned, because of the structure operation symmetry, these devices emit radiation identically towards both directions along the laser length. However, only one can be practically used in LO applications. Therefore, advancing the structure such to emit all the radiation in one direction is quite interesting for increasing the applicable output power. Whilst putting a reflector at one end facet in conventional Fabry-Perot lasers can do this function, it is not doable with third order DFB QCLs, where the radiation is flowing outside (on top of the surface) the waveguide. Alternatively, taking advantage of the out-extended field is again a solution to make the emission unidirectional [32]. In this technique reflectors are placed appropriately around the DFB structure so that each emission unit sees two of them in front and rear sides. Properly positioning of reflectors causes the reflected field to destructively interfere with the backward radiation, making the

propagation dominant in the forward direction. This design increases the forward flowing power by a factor of 1.8. Figure 2.10 shows the electric field distribution, the far-field radiation pattern and an SEM photo of such a system.

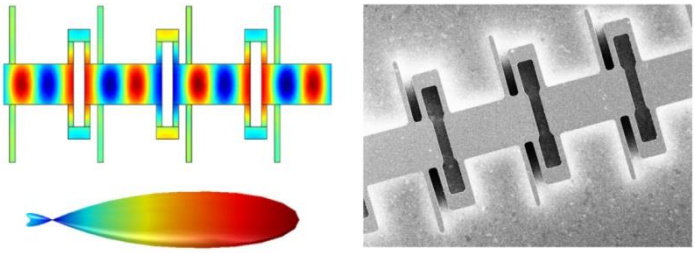

Figure 2.10. Electric field distribution and far-field radiation pattern (a) together with an SEM photo of a unidirectional third-order DFB THz QCL [32]

Bibliography

[1] M. S. Vitiello, G. Scalari, B. Williams and P. D. Natale, "Quantum cascade lasers: 20 years of challenges," Opt. Express **23**(4), 5167 (2015).

[2] L. Li, et al., "Terahertz quantum cascade lasers with >1 W output powers," Electron. Lett., **50**(4), 309 (2014).

[3] B. Williams, S. Kumar, Q. Hu and J. Reno, "High-power terahertz quantum-cascade lasers," Electron. Lett., **42** (2), 18 (2006).

[4] S. Fathololoumi et al., "Terahertz quantum cascade lasers operating up to ∼200 K with optimized oscillator strength and improved injection tunneling," Opt. Express **20**(4), 3331 (2012).

[5] M. Wienold, B. Röben, L. Schrottke, R. Sharma, A. Tahraoui, K. Biermann and H. T. Grahn, "High-temperature, continuous-wave operation of terahertz quantum-cascade lasers with metal-metal waveguides and third-order distributed feedback," Opt. Express **22**(3), 3334 (2014).

[6] G. Liang, T. Liu and Q. J. Wang, "Recent Developments of Terahertz Quantum Cascade Lasers," IEEE J. Select. Top. Quant. Electron. **23**(4), 1200118 (2017).

[7] R. Köhler, A. Tredicucci, F. Beltram, E. H. Beere, E. H. Linfield, A. G. Davies, D. A. Ritchie, R. C. Iotti and F. Rossi, "Terahertz semiconductor-heterostructure laser," Nature **417**, 156 (2002).

[8] B. S. Willams, "Terahertz quantum-cascade lasers," Nat. Photonics **1**, 517 (2007).

[9] B. S. Williams, S. Kumar, Q. Hu and J. L. Reno, "Operation of terahertz quantum-cascade lasers at 164 K in pulsed mode and at 117 K in continuous-wave mode," Opt. Express **13**, 3331 (2005).

[10] B. S. Williams, "Terahertz quantum cascade lasers," PhD dissertation, MIT (2003).

[11] M. S. Vitiello, L. Consolino, S. Bartalini, A. Taschin, A. Tredicucci, M. Inguscio and P. De Natale, "Quantum-limited frequency fluctuations in a Terahertz laser," Nat. Photonics **6**, 525 (2012).

[12] P. Khosropanah, et al, " Phase locking of a 2.7 THz quantum cascade laser to a microwave reference," Opt. Letters **34**, 2958 (2009).

[13] Y. Ren, J.N. Hovenier, M. Cui, D.J. Hayton, J.R. Gao, T.M. Klapwijk, S.C. Shi, T-Y. Kao, Q. Hu, and J. L. Reno, " Frequency locking of single-mode 3.5-THz quantum cascade lasers using a gas cell," Appl. Phys. Lett. **100**, 041111 (2012).

[14] A. V. Khudchenko, D. Hayton, D. G. Pavelyev, A. M. Baryshev, J. R. Gao, T. Y. Kao, Q. Hu. J. L. Reno and V. L. Vaks, "Phase locking a 4.7 THz quantum

cascade laser using a super-lattice diode as harmonic mixer," in 39th IRMMW-THz, Tucson, AZ (2014).

[15] S. Kohen, B. S. Williams and Q. Hu, "Electromagnetic modeling of terahertz quantum cascade laser waveguides and resonators," J. Appl. Phys. **97**, 053106 (2005).

[16] K. Unterrainer, R. Colombelli, C. Gmachl, F. Capasso, H. Y. Hwang, A. M. Sergent, D. L. Sivco and A. Y. Cho, "Quantum cascade lasers with double metal-semiconductor waveguide resonators," Appl. Phys. Lett. **80**, 3060 (2002).

[17] A. W. M. Lee, Q. Qin, S. Kumar, B. S. Williams, Q. Hu and J. L. Reno, "High-power and high-temperature THz quantum-cascade lasers based on lens-coupled metal-metal waveguides," Opt. Letters **32**, 2840 (2007).

[18] M. Amanti, M. Fischer, C. Walther, G. Scalari and J. Faist, "Horn antennas for terahertz quantum cascade lasers," Electron. Lett. **43**, 573 (2007).

[19] A. Gordon, C. Y. Wang, L. Diehl, F. X. Kaertner, A. Belyanin, D. Bour, S. Corzine, G. Hoefler, H. C. Liu, H. Schneider, T. Maier, M. Troccoli, J. Faist and F. Capasso, "Multimode regime in QCLs: from coherent instabilities to spatial hole burning," Phys. Rev. A **7**, 053804 (2008).

[20] Y. Chassagneux, et al, "Electrically pumped photonic-crystal terahertz lasers controlled by boundary conditions," Nature **457**, 174 (2009).

[21] G. Sevin, et al, "Optimized surface-emitting photonic-crystal terahertz quantum cascade lasers with reduced resonator dimensions," Appl. Phys. Lett. **97**, 131101 (2010).

[22] B. S. Williams, S. Kumar, Q. Hu and J. L. Reno, "DFB THz QCLs with laterally corrugated metal waveguides," Opt. Lett. **30**(21), 2909 (2005).

[23] S. Kumar, B. S. Williams, Q. Qin, A. W. M. Lee, Q. Hu and J. L. Reno, "Surface-emitting DFB THz QCLs in metal-metal waveguides," Opt. Express **15**(1), 113 (2007).

[24] L. Mahler, et al, "Distributed feedback ring resonators for vertically emitting terahertz quantum cascade lasers," Opt. Express **17**(15), 13031 (2009).

[25] T. Y. Kao, Q. Hu and J. L. Reno, "Phase-locked arrays of surface-mitting terahertz quantum-cascade lasers," Appl. Phys. Lett. **96**, 101106 (2010).

[26] M. I. Amanti, M. Fischer, G. Scalari, M. Beck and J. Faist, "Low-divergence single-mode terahertz quantum cascade laser," Nat. Photonics **3**, 586 (2009).

[27] T. Kao, Q. Hu and J. L. Reno, "Perfectly phase-matched third-order distributed feedback terahertz quantum-cascade lasers," Opt. Lett., **37**(11), 2070 (2012).

[28] A. J. L. Adam, I. Kasalynas, J. N. Hovenier, T. O. Klaassen, J. R. Gao, E. E. Orlova, B. S. Williams, S. Kumar, Q. Hu and J. L. Reno, "Beam pattern of Terahertz

quantum cascade lasers with sub-wavelength cavity dimensions," Appl. Phys. Lett. **88**, 151105 (2006).

[29] M. Amanti, G. Scalari, F. Castellano, M. Beck, J. Faist, "Low divergence terahertz photonic-wire laser," Opt. Express **18**(6), 6390 (2010).

[30] M. S. Vitiello and A. Tredicucci, "Tunable emission in THz quantum cascade lasers," IEEE Trans. Terahertz. Sci. Technol. **1**(1), 76 (2011).

[31] Q. Qin, B. S. Williams, S. Kumar, J. L. Reno and Q. Hu, "Tuning a terahertz wire laser," Nat. Photonics **3**, 732 (2009).

[32] A. Khalatpour, J. L. Reno, N. P. Kherani and Q. Hu, "Unidirectional photonic wire laser," Nat. Photonics **11**, 555 (2017).

3

FREQUENCY LOCKING AND MONITORING BASED ON BI-DIRECTIONAL TERAHERTZ RADIATION OF A 3RD-ORDER DISTRIBUTED FEEDBACK QUANTUM CASCADE LASER*

We have performed frequency locking of a dual, forward reverse emitting third-order distributed feedback quantum cascade laser (QCL) at 3.5 THz. By using both directions of THz emission in combination with two gas cells and two power detectors, we can for the first time perform frequency stabilization, while monitor the frequency locking quality independently. We also characterize how the use of a less sensitive pyroelectric detector can influence the quality of frequency locking, illustrating experimentally that the sensitivity of the detectors is crucial. Using both directions of terahertz (THz) radiation has a particular advantage for the application of a QCL as a local oscillator, where radiation from one side can be used for frequency/phase stabilization, leaving the other side to be fully utilized as a local oscillator to pump a mixer.

* Published as N. van Marrewijk, B. Mirzaei, D. Hayton, J. R. Gao, T. Y. Kao, Q. Hu and J. L. Reno, Journal of Infrared, Millimeter, and Terahertz Waves 36(12), 1210 (2015).

3.1. Introduction

Terahertz (THz) quantum cascade lasers (QCLs) have been demonstrated as local oscillators for high-resolution spectroscopy both in the lab [1] and, more recently, in a real astronomic instrument [2]. In general, since the QCL is not inherently frequency stable, a system of frequency or phase locking [3, 4] is required. So far, the radiation emitted from only one direction of the QCL has been used for both pumping a mixer and stabilizing the frequency of the source [5]. In this way, to achieve frequency locking, part of the beam power is unavailable for the mixer. There have been many experiments to demonstrate the phase or frequency locking of a THz QCL [6-12]. For local oscillators operated at the high end of terahertz frequencies, such as for the astronomically important [OI] line at 4.7 THz, only two techniques are practically usable for frequency/phase locking since it can only be observed by an instrument in space. They are based on either a gas cell in combination with a THz power detector [10, 11] or a harmonic mixer [12]. The harmonic mixer down converts the QCL THz signal to one typically at MHz frequencies using the higher harmonic of a GHz local oscillator reference signal [12]. To realize the frequency locking, both techniques require a threshold power from a QCL, which can be comparable to what is needed for operating a superconducting mixer. In some cases, the power required for frequency locking can be half of the total power available from the laser making it very difficult to pump a mixer.

It is known that both a standard Fabry-Perot QCL and a distributed feedback (DFB) QCL can emit radiation from both forward and backward directions [13]. The beams in both directions are generated from a single oscillator, and therefore all the temporal characteristics are expected to be fundamentally the same. To take full advantage of the total radiating power available from a QCL, it is very beneficial to make use of the radiation from both directions. For example, one direction acts as a local oscillator source while the other is used for frequency or phase locking. This approach can also have other potential applications such as THz imaging radar

[14]. Although it seems obvious that one should take advantage of both beams, in practice no one has ever reported the use of a QCL in this configuration as local oscillator at the high end of THz frequencies (e.g., 4.7 THz), where the available power is still relatively low.

In this paper, we develop a measurement setup that allows the detection of the radiation simultaneously from both directions. We start with the basic characterization of the radiation beam patterns and emitted power of a 3.5 THz, third-order DFB QCL [15]. We demonstrate a practical application of the dual emitting QCL by applying two gas cell-based frequency discriminators, one for each emission. Specifically, one side is used to realize frequency locking while the other side is used to monitor frequency stability. We find that the sensitivity of the detectors is crucial for both frequency locking and frequency monitoring. Finally, we describe briefly an experiment to make use of one side of radiation to carry out the frequency locking and the other side of the radiation to pump a superconducting niobium nitride (NbN) hot electron bolometer (HEB) mixer [16].

3.2. QCL and the holder

We use a third-order DFB THz QCL based on a four-well resonant phonon depopulation design [17] developed at MIT (Fig. 3.1a). It emits a single mode at 3.490 THz, as measured by a Fourier transform spectrometer (FTS) with a resolution of 0.6 GHz. The device comprises 27 lateral corrugated grating periods over a ~1-mm-long active region, which is 10 μm thick and 50 μm wide. Multiple lasers are grouped together on a single chip, and the QCL used for our experiment is shown in Fig. 3.1a, where the QCL layout is perfectly symmetrical except that the bonding pad and wire appear only on one end of the laser. The third-order DFB structure [18-20], based on a linear phased antenna array concept, can have a controllable single emission mode as well as a low divergent far-field beam. Figure 3.1b schematically illustrates the laser on a chip that is mounted on a Cu chip holder. The latter is attached to a cold plate mounted on a cryocooler. Although the width of the cold plate, on top of which the laser holder is mounted, is larger

than the length of the laser, due to a relative thick chip holder together with the fact that the beam can leave from the QCL chip at a positive angle ~5° [20], the reflection effects due to the presence of the cold plate are negligible. The radiation can therefore be emitted freely and simultaneously towards both directions.

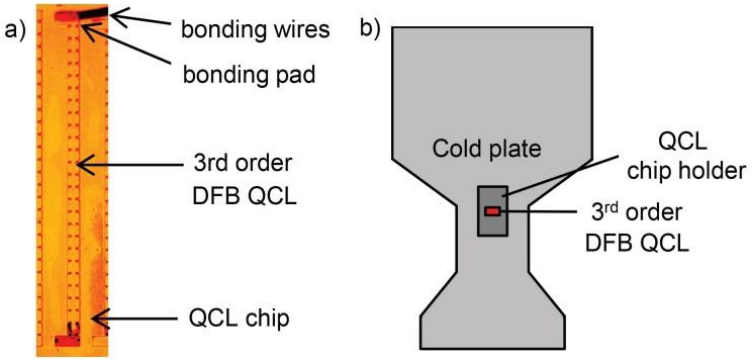

Figure 3.1. a) Photo of the third-order DFB QCL used for the experiment on a chip. One end of the laser with the bonding wire/pad is positioned towards the backward direction in the setup shown in Fig. 3.2; b) Sketch of the QCL sample holder. The QCL (red) is mounted on a Cu chip holder (dark gray). The chip holder is attached to a cold plate (light gray) connected to a cryocooler

3.3. Measurement setup

The setup for the key measurement of this paper is illustrated in Fig. 3.2. The QCL is mounted in a pulse tube cryocooler that reaches ~4 K without load and typically ~12 K with the ~3-W electrical power dissipated by the QCL. The QCL is positioned in such a way where one end of the laser with the bonding pad and wire points to the backward direction. To allow both forward and backward radiation to exit the cryostat, two windows are installed. The front window (corresponding to the forward direction) is a 3-mm-thick high-density polyethylene (HDPE) with a transmission of 71 % measured at the laser frequency, while the rear window is a 1-mm-thick ultra-high molecular weight polyethylene (UHMW-PE) with a transmission of 89 % obtained at the same frequency. The QCL is placed in the center of the cryocooler with roughly an equal distance of ~ 80 mm to the windows.

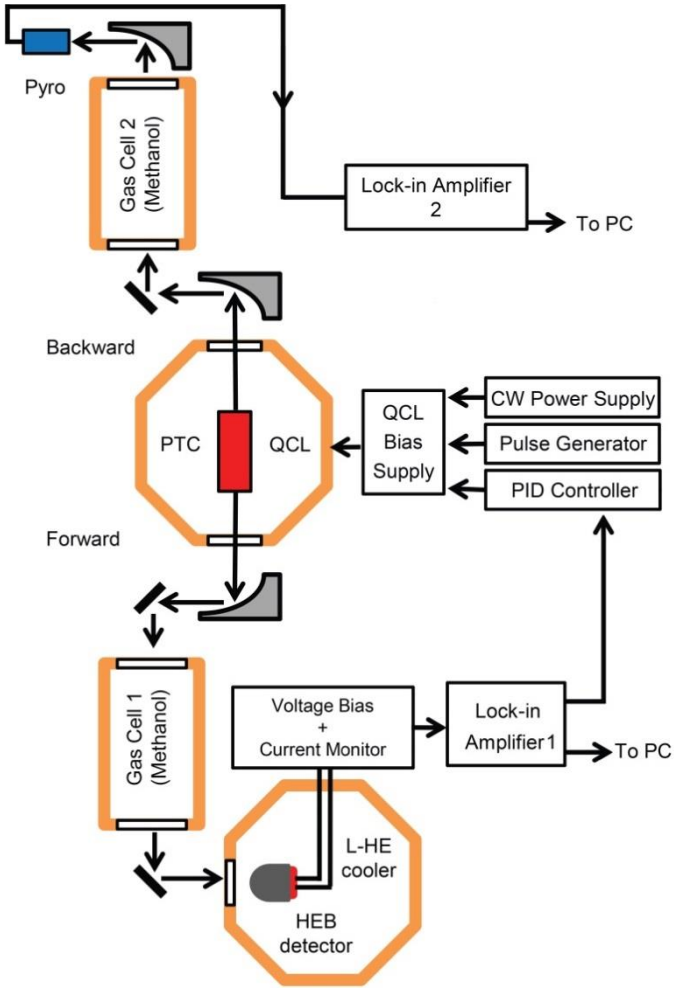

Figure 3.2. Schematic of the measurement setup. The QCL is operated in a pulse tube cryocooler (PTC). The combination of a gas cell and a HEB detector is applied to generate an error signal to a PID controller for frequency locking (forward) and a second gas cell with a pyroelectric detector to monitor the quality of frequency locking (backward).

Both forward and backward radiation are collimated by applying aluminum parabolic mirrors (f = 80 mm) in front of each window and then reflected by flat mirrors through each of two gas cells with lengths of 41 and 27 cm, respectively. Note that the different lengths are not chosen on purpose but are due to their

availability. Due to the abundance of absorption lines in the THz, methanol is used as the reference gas in both gas cells.

The forward radiation beam is then reflected by a flat mirror into a Si lens/antenna-coupled superconducting NbN HEB [1, 16], which is operated as a bolometric power detector. It produces an error signal that is fed, via a lock-in amplifier, to a proportional integral derivative (PID) controller. The PID controller makes a correction signal that is added into the QCL bias voltage to hold the error signal at zero and therefore to stabilize the frequency. The feedback bandwidth, limited by the lock-in amplifier time constant, is ~10 Hz, although the PID bandwidth is much higher (~1 kHz). As indicated by the measured frequency noise power spectral density [11], a bandwidth of ~10 Hz is in practice sufficient to stabilize the average laser frequency and to remove low-frequency jitters.

The backward radiation beam after passing through the gas cell 2 is focused by an aluminum parabolic mirror (f = 25 mm) onto a room temperature pyroelectric detector that is used for monitoring the quality of the frequency locking. We read out the signals from both detectors via two separate lock-in amplifiers connected to a PC. Since we have the same gas and roughly the same pressures in the gas cells, we expect to see a similar changing behavior from the signals detected by both detectors. The two detectors however have very different sensitivities. The HEB has a noise equivalent power (NEP) of 10^{-12} – 10^{-13} [21], whereas the pyroelectric detector has a NEP of ≥ 10^{-9} [22]. Also, the former works at 4 K, while the latter operates at room temperature.

3.4. Experimental results and discussion

We start with the measurements of the far-field QCL beam patterns in both directions by using a small aperture pyroelectric detector scanned within a plane normal to the direction along the laser structure indicated in Fig. 3.3b (z-axis). The distance between the QCL and the scanned planes is about 90 mm. The laser was operated at a bias voltage of 14 V in a pulsed mode. We use this setting for all the

measurements in this work except when specified otherwise. Figure 3.3 shows the measured beam patterns of the radiation from both directions.

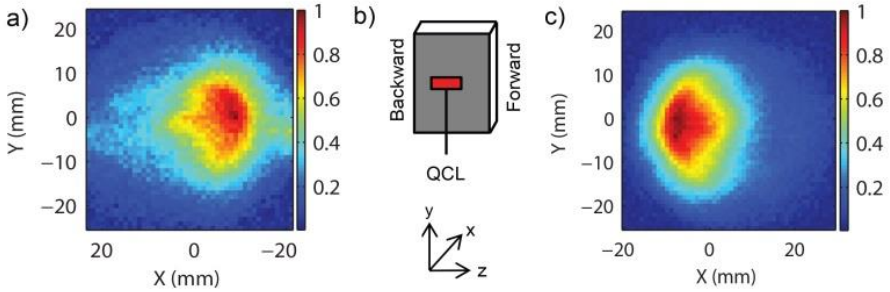

Figure 3.3. a) Measured beam pattern (normalized) from the backward radiation. The observation plane (x, y) is about 90 mm to the QCL; b) Orientation of the QCL. The arrows indicate the positive x, y, and z directions; c) Measured beam pattern (normalized) from the forward radiation. The observation plane (x, y) is also about 90 mm to the QCL.

We apply two methods to compare the powers between the radiation from the two directions. One is to estimate the relative powers by integrating the intensity of the entire beam. The other is to measure the relative powers by focusing the radiation into a pyroelectric detector. We find that the two directions give unequal powers, being independent of the methods used. The backward direction emits less power and has only 56 % power from the forward direction, obtained after correcting the effect due to two different transmissions of the windows. The difference by nearly a factor of 2 in power may be attributed to the bonding pad/wire on the laser in the backward direction. However, it requires additional work to confirm. The power result is consistent with the beam pattern measurement, where the S/N ratio is worse in the backward direction. We have not measured the absolute power of this particular laser since we are more interested in the ratio. However, based on the power measurement of a similar laser [5], we expect the maximal output power of the forward direction to be about 0.8 mW, while the other direction is 0.45 mW.

Prior to frequency locking, we measure methanol absorption lines by sweeping the QCL bias voltage from 13.5 to 14.5 V, which tunes the frequency electrically, as

confirmed by a separate FTS measurement. Both gas cells are filled with methanol at a pressure of ~1.7 mbar. The transmitted signal intensity measured using both the HEB and the pyroelectric detector is plotted as a function of the QCL bias voltage in Fig. 3.4, where the signals are recorded with two lock-in amplifiers simultaneously.

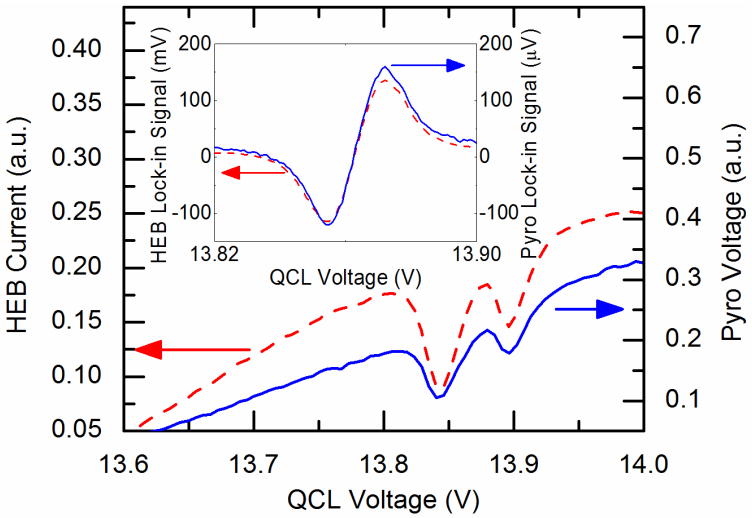

Figure 3.4. Absorption lines of methanol at 1.7 mbar. The lines are measured with an HEB (red dashed) and a pyro (blue), respectively. The inset shows the derivative of an absorption line around 13.8 V measured with the HEB (red dashed) and the pyro (blue) by a lock-in amplifier when QCL is modulated with a small AC signal.

The absorption lines, as expected when measuring with a single source, appeared at exactly the same bias voltages. The derivative of the absorption line at ~13.84 V was also measured by applying a small 70-Hz, 10-mVp-p AC modulation [10]. The resulting derivative curves for each detector is included as the inset in Fig. 3.4. The derivative curves change linearly with the QCL bias voltage over a range close to the absorption line center.

In this way, we can make use of an absorption line for frequency stabilization of the QCL because its frequency is known to be fundamentally stable [10, 11]. Any fluctuations in the frequency of the QCL below the bandwidth of ~ 10 Hz will cause

proportional changes in the derivative output. In practice, we set the QCL bias voltage so as to have its frequency close to the center of a specific absorption line and then feed the derivative signal as the error input to the PID controller. The controller produces a feedback to the QCL bias voltage to keep its frequency aligned to the center of the absorption line where the derivative is equal to zero.

Now we focus on the key experiment of this paper using the setup in Fig. 3.2 by applying this method to gas cell 1 by feeding the HEB's derivative signal to the PID controller to stabilize the frequency, while utilizing output from the gas cell 2 to monitor the quality of frequency locking. A time series of the error signals measured simultaneously from both lock-in amplifiers is plotted in Fig. 3.5, where the upper panel shows the signal from the HEB and the lower panel shows the signal recorded by the pyroelectric detector.

In the time interval from 0 to 9 s (mode 1), the QCL was free running and the error signals recorded in both detectors are relatively large, which is primarily due to the ~1-Hz frequency of the pulse tube cooler. Low frequency drift noise is also visible. Afterwards (mode 2, 10–24 s), the PID is turned on reducing the error signal from the HEB by a factor of 20. It is generally accepted from the previous works [10, 11] that the QCL is then frequency locked. In the same time interval, the error signal from the pyroelectric detector is also reduced in comparison with the free running state. Although the fluctuations of the pyroelectric signal are around zero after the frequency locking, they are not as strongly suppressed as the fluctuations in the HEB. To understand this, we actually block the radiation to the pyroelectric detector and record its error signal, while the frequency locking is maintained by the HEB (referred as the mode 3 in Fig. 3.5). We find that the intrinsic noise level of the pyroelectric detector dominates in both cases, no matter whether there is a radiation signal to the pyroelectric detector or not. Thus, we realize that the error signal from the pyroelectric detector does not directly correspond to the frequency locking quality, but rather to the noise floor of the detector.

Due to the linearity of the derivative signal versus the QCL voltage curve, we can convert its fluctuation amplitude to frequency by making use of the voltage

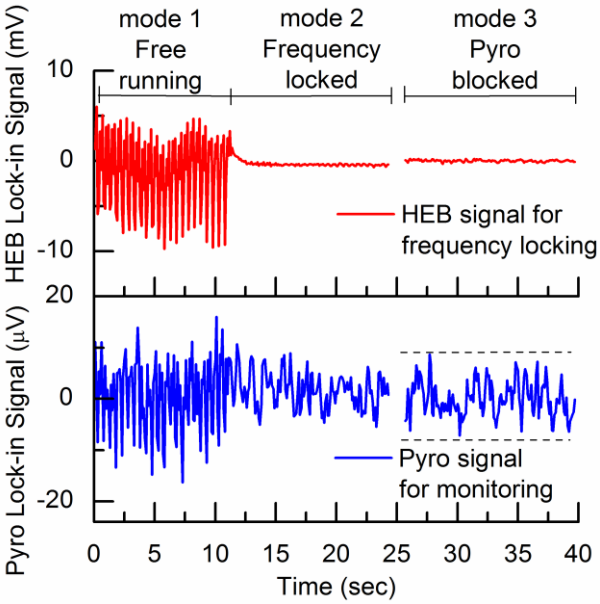

Figure 3.5. The lock-in amplifier signal from the HEB (top, red) and the pyroelectric detector (bottom, blue), reflecting the frequency stability of the QCL. Frequency locking is engaged to the forward radiation after 12 s using the HEB signal (control), while the pyroelectric detector monitors the frequency of the backward radiation. After 30 s, the radiation to the pyroelectric detector is blocked. The dashed line represents the pyroelectric detector noise limit.

tuning coefficient of the laser [11]. The latter has roughly −0.6 GHz/V determined from a separate FTS experiment. We are therefore able to estimate a free running QCL linewidth of around 800 kHz, which is much larger than the intrinsic linewidth [23] because of time-dependent jitters. Strictly speaking, this is not the laser linewidth, but rather the range of laser emission frequency averaged in a measured time interval [11]. After turning the frequency locking on, this so-called linewidth is reduced to about 40 kHz. This analysis is based on the observation from the HEB. In contrast, if we make use of the error signal from the pyroelectric detector, we would record a linewidth of 300 kHz, which contradicts obviously with the first result.

To verify the importance of the noise level of the detector in such a frequency locking experiment, we modify the experiment slightly and take the error signal from the pyroelectric detector for the frequency locking and the HEB's signal for the monitoring. The results, plotted in the same manner as in Fig. 3.5, are shown in Fig. 3.6.

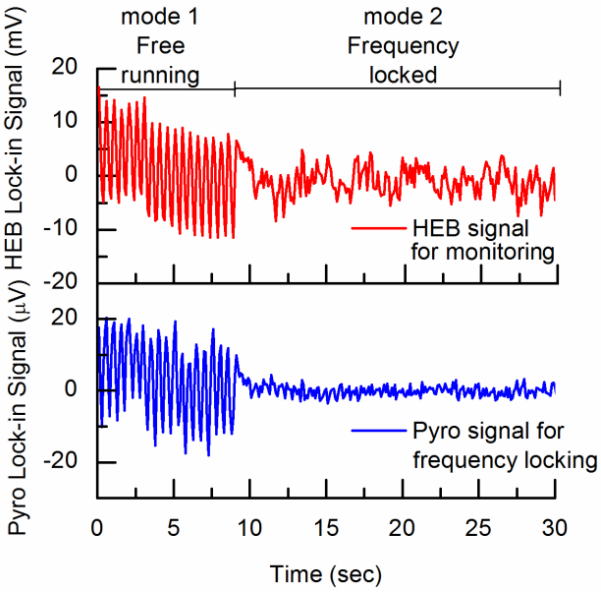

Figure 3.6. The lock-in amplifier signal from the HEB (top, red) and the pyroelectric detector (bottom, blue) reflecting the frequency stability of the QCL. Frequency locking is engaged to the backward radiation after 9 s using the pyroelectric detector signal (control), while the HEB monitors the frequency of the forward radiation.

We now focus on the case of mode 2. The error signal from the pyroelectric detector has been reduced considerably relative to the free running case, and the signal is centered around zero. However, compared with the results by using the HEB for the frequency locking in Fig. 3.5, the residue on the locked signal is large. We attribute these fluctuations to the intrinsic noise of the pyroelectric detector. In this case, the PID controller cannot distinguish the changes between the QCL frequency and the noise from the detector. Consequently, the feedback signal to

the bias of the QCL cannot be appropriately applied. The lack of suppression in the frequency fluctuations can be monitored by the HEB. Since the (intrinsic) noise floor of the HEB is at least three or four orders of magnitude lower than that of the pyroelectric detector [21], the error signal in this case reflects more accurately the quality of the frequency locking. Because of the higher sensitivity of the HEB, these fluctuations are exclusively due to the frequency fluctuations of the QCL and they show only a mild reduction in the linewidth of the QCL. We perform the same analysis as before and find a free running linewidth of around 800 kHz. It becomes about 300 kHz in the locked situation when we use the HEB signal to assess the linewidth. From the pyroelectric detector signal, we would estimate roughly a 100-kHz linewidth. The small linewidth compared with the linewidth derived from the HEB may come from the fact that the PID controller adjusts the QCL frequency to remove the noise from the pyroelectric detector. This is why the HEB monitor shows more noise when the QCL is locked.

To explore the parameters of our experimental setup, we repeat the measurements a few times by adjusting three factors: the methanol pressure in the gas cells, the modulation frequency, and the modulation amplitude. We vary the pressure by a sub-mbar step and find that in the extreme case of very low pressures, the absorption lines become narrower, resulting in a very sharp derivative signal. This makes a more sensitive frequency discriminator but with reduced frequency bandwidth. In the opposite case of very high pressures, the absorption lines are too broad and the change in the error signal due to the change of the frequency is too weak. Then, the frequency locking becomes ineffective.

With respect to the modulation signal applied to the QCL bias voltage, we find that increasing the frequency can increase the S/N ratio, and reducing the amplitude helps to smooth the derivative signal. Both work well for the HEB case but not for the pyroelectric detector. As a compromise, we choose a relatively low modulation frequency of 70 Hz and relatively large amplitude of 10 mV to optimize the performance of the pyroelectric detector in the frequency locking experiments, while the HEB suffers slightly in its performance.

The consequence of the above choice is that in addition to the locked linewidth of 40 kHz and free running linewidth of 800 kHz, simultaneously the frequency of the laser is modulated by 6 MHz at a frequency of 70 Hz, which is calculated based on the voltage tuning coefficient of −0.6 GHz/V. Since a lock-in amplifier is used to demodulate the detector signal, the 70-Hz carrier is not visible in Figs. 3.5 and 3.6. This side effect is intrinsic to the gas cell technique [10, 11], although the effect can be made considerably weaker if one chooses a smaller modulation signal.

It is worthwhile to stress that our experiment represents the first one to make use of the bi-directional radiation from a single THz QCL for a frequency locking experiment, where the laser can be locked, while the quality of the locking can be evaluated in the same time. It is also the first to experimentally demonstrate the importance of the detector sensitivity in a frequency lock loop.

An interesting experiment that remains is to use the forward radiation for the frequency or phase locking for example and to use the backward radiation for monitoring if we can apply a second detector that is a low-noise HEB or a comparable detector. A different technique to monitor the linewidth on the other side after the locking could also be used. The latter can take advantage of a superlattice harmonic mixer, which can generate an ideal reference signal and mix it with the QCL signal into a microwave frequency [12], where one can directly record the linewidth by a spectrum analyzer.

A key demonstration of the advantage in using a dual emitting QCL is to show that a superconducting NbN HEB mixer can be appropriately pumped using one side of the laser while the other side is used for frequency locking. We perform such an experiment by using a standard NbN HEB mixer, which has a NbN area of 2 μm × 0.2 μm, corresponding to a power requirement of 200 nW at the detector itself [1]. We apply a setup simplified with respect to the one in Fig. 3.2 by removing the gas cell 1 in the forward direction. We then lock the frequency of the QCL using the backward beam. At the same time, we apply the forward beam to pump the superconducting mixer. We find that it can pump the HEB to its nearly optimum operating points. With further optimization of the optics to match the

beam to the HEB, we expect that the forward beam can provide sufficient power to pump the HEB to its optimum operating points, while the frequency locking is realized with the backward beam.

In this way, we can in essence make use of 100 % available power from a frequency-locked QCL. This approach is certainly beneficial for the case where a QCL is applied as a local oscillator for a superconducting mixer. This approach will be even more attractive for the cases where a QCL is applied as a local oscillator for a semiconductor Schottky mixer and an array of mixers, both of which require high power.

3.5. Conclusion

By making use of the radiation from the forward and backward directions of a third-order DFB QCL at 3.5 THz, we demonstrate for the first time that we can introduce the frequency locking, while can monitor the quality of the locking simultaneously. Furthermore, by applying two power detectors with a different noise level, we show that the frequency locking quality, namely the linewidth derived from the error signal, depends strongly on the noise level of the detector used. In the case of applying a high noise power detector for the locking, the PID controller not only corrects the frequency fluctuations of the laser but also compensates the noise from the detector by adjusting the QCL frequency, which can lead to a much wider locked linewidth than what is indicated by the (locking) detector.

Bibliography

[1] J. L. Kloosterman, D. J. Hayton, Y. Ren, T. Y. Kao, J. N. Hovenier, J. R. Gao, T. M. Klapwijk, Q. Hu, C. K. Walker, and J. L. Reno, “Hot electron bolometer heterodyne receiver with a 4.7-THz quantum cascade laser as a local oscillator,” Appl. Phys. Lett. **102**, 011123 (2013).

[2] H. Richter, M. Wienold, L. Schrottke, K. Biermann, H. T. Grahn and H. W. Hubers, “4.7-THz Local oscillator for the GREAT heterodyne spectrometer on SOFIA,” IEEE Trans. Terahertz Sci. Technol. **5**, 539 (2015).

[3] A. L. Betz, R. T. Boreiko, B. S. Williams, S. Kumar, Q. Hu, and J. L. Reno, “Frequency and phase-lock control of a 3 THz quantum cascade laser,” Opt. Lett. **30**(14), 1837 (2005).

[4] M. Zhu and J. L. Hall, “Stabilization of optical phase/frequency of a laser system-application to a commercial dye laser with an external stabilizer,” J. Opt. Soc. Am. B. **10**, 802 (1993).

[5] Y. Ren, D.J. Hayton, J.N. Hovenier, M. Cui, J.R. Gao, T.M. Klapwijk, S.C. Shi, T-Y. Kao, Q. Hu, and J.L. Reno, “Frequency and amplitude stabilized terahertz quantum cascade laser as local oscillator,” Appl. Phys. Lett. **101**, 101111 (2012).

[6] A. Baryshev, J. N. Hovenier, A. J. L. Adam, I. Kašalynas, J. R. Gao, T. O. Klaassen, B. S. Williams, S. Kumar, Q. Hu, and J. L. Reno, “Phase locking and spectral linewidth of a two-mode terahertz quantum cascade laser,” Appl. Phys. Lett. **89**, 031115 (2012).

[7] D. Rabanus, U. U. Graf, M. Philipp, O. Ricken, J. Stutzki, B. Vowinkel, M. C. Wiedner, C. Walther, M. Fischer, and J. Faist, “Phase locking of a 1.5 Terahertz quantum cascade laser and use as a local oscillator in a heterodyne HEB receiver,” Opt. Express **17**, 1159 (2009).

[8] P. Khosropanah, A. Baryshev, W. Zhang, W. Jellema, J. N. Hovenier, J. R. Gao, T. M. Klapwijk, D. G. Paveliev, B. S. Williams, S. Kumar, Q. Hu, J. L. Reno, B. Klein, and J. L. Hesler, “Phase locking of a 2.7 THz quantum cascade laser to a microwave reference,” Opt. Lett. **34**, 2958 (2009).

[9] L. Consolino, A. Taschin, P. Bartolini, S. Bartalini, P. Cancio, A. Tredicucci, H. E. Beere, D. A. Ritchie, R. Torre, M. S. Vitiello, P. De Natale, “Phase-locking to a free-space terahertz comb for metrological-grade terahertz lasers,” Nat. Commun. **3**, 1040 (2012).

[10] H. Richter, S. G. Pavlov, A. D. Semenov, L. Mahler, A. Tredicucci, H. E. Beere, D. A. Ritchie, and H.-W. Hübers, “Submegahertz frequency stabilization of a

terahertz quantum cascade laser to a molecular absorption line," Appl. Phys. Lett. **96**, 071112 (2010).

[11] Y. Ren, J.N. Hovenier, M. Cui, D.J. Hayton, J.R. Gao, T.M. Klapwijk, S.C. Shi, T-Y. Kao, Q. Hu, and J. L. Reno, "Frequency locking of single-mode 3.5-THz quantum cascade lasers using a gas cell," Appl. Phys. Lett. **100**, 041111 (2012).

[12] D. J. Hayton, A. Khudchencko, D. G. Pavelyev, J. N. Hovenier, A. Baryshev, J. R. Gao, T. Y. Kao, Q. Hu, J. L. Reno, and V. Vaks, "Phase locking of a 3.4 THz third-order distributed feedback quantum cascade laser using a room-temperature superlattice harmonic mixer," Appl. Phys. Lett. **103**, 051115 (2013).

[13] B.S. Williams, "Terahertz Quantum-Cascade Lasers," Nature Photonics **1**, 517 (2007).

[14] K.B. Cooper, R.J. Dengler, N. Llombart, B. Thomas, G. Chattopadhyay, and P.H. Siegel, "THz Imaging Radar for Standoff Personnel Screening," IEEE Trans. Terahertz Sci. Technol. **1**, 169 (2011).

[15] M. I. Amanti, M. Fischer, G. Scalari, M. Beck, and J. Faist, "Low-divergence single-mode terahertz quantum cascade laser," Nature Photonics **3**, 586 (2009).

[16] J. R. Gao, M. Hajenius, Z. Q. Yang, J. J. A. Baselmans, P. Khosropanah, R. Barends, and T. M. Klapwijk, "Terahertz superconducting hot electron bolometer heterodyne receivers," IEEE Trans. Appl. Supercond. **17**, 252 (2007).

[17] Q. Qin, B. S. Williams, S. Kumar, J. L. Reno, and Q. Hu, "Tuning a Terahertz Wire Laser," Nature Photonics **3**, 732 (2009).

[18] M. I. Amanti, G. Scalari, F. Castellano, M. Beck, and J. Faist, "Low divergence Terahertz photonic-wire laser," Opt. Express **18**, 6390 (2010).

[19] Y. Kao, Q. Hu, and J. L. Reno, "Perfectly phase-matched third-order distributed feedback terahertz quantum-cascade lasers," Opt. Lett. **37**, 2070 (2012).

[20] M. Cui, J. N. Hovenier, Y. Ren, N. Vercruyssen, J. R. Gao, T. Y. Kao, Q. Hu, and J. L. Reno, "Beam and phase distributions of a terahertz quantum cascade wire laser," Appl. Phys. Lett. **102**, 111113 (2013).

[21] Y. Ren, W. Miao, Q. J. Yao, W. Zhang, and S. C. Shi, "Terahertz direct detection characteristics of a superconducting NbN bolometer," Chin. Phys. Lett. **28**, 010702 (2011).

[22] R. N. Schouten, "A new amplifier design for fast low-noise far-infrared detectors using a pyroelectric element," Meas Sci. Technol. **9**, 686 (1998).

[23] M. S. Vitiello, L. Consolino, S. Bartalini, A. Taschin, A. Tredicucci, M. Inguscio, and P. De Natale, “Quantum-limited frequency fluctuations in a terahertz laser,” Nat. Photonics **6**, 525 (2012).

4

FREQUENCY TUNING OF 3RD-ORDER DISTRIBUTED FEEDBACK TERAHERTZ QUANTUM CASCADE LASERS BY SiO_2 AND PMMA*

We report an extensive study of the effect of an additional dielectric layer on the frequency of terahertz quantum cascade lasers (QCLs). QCLs with third-order distributed feedback structure at frequencies of 3.5 and 4.7 THz are used in our experiment. The applied dielectric layer is either Silicon-dioxide (SiO2) or Polymethylmethacrylaat (PMMA). We find that both dielectric layers can shift the lasing frequency by up to -6 GHz on a 3.5 THz QCL, and up to -13 GHz for a 4.7 THz QCL. Full 3D FEM simulations suggest that the effect is dominated by the effective thickness of the dielectric on the side walls of the laser structure, and also confirm that for a given dielectric layer, the effect is stronger in the 4.7 THz QCL due to its different extension of the electro-magnetic field to the free space. This work provides a guideline for shifting the frequency of an existing QCL for frequency critical applications such as spectroscopy or use as a local oscillator.

* Published as B. Mirzaei, D. Hayton, D. Thoen J. R. Gao, T. Y. Kao, Q. Hu and J. L. Reno, IEEE transactions on terahertz science and technology, **6**(6), 851 (2016).

4.1. Introduction

Terahertz (THz) quantum cascade lasers (QCLs) have been demonstrated as local oscillators for high resolution spectroscopy both in the lab [1] and in a real astronomic instrument [2]. In the past decade, enormous progress has been made on the operating temperature [3], output power [4], beam pattern, single mode emission [5-6] and frequency tuning [7-10]. One example is the third-order distributed feedback laser [7] based on a metal-metal waveguide structure [11], which can be operated practically above 40 K using a compact, low power stirling cooler, with a targeted single mode emission in combination with reasonable output power (~ 0.5 mW) and single spot far-field beam pattern. However, due to the limited accuracy of the lithography, the difficulties to determine effective refractive index, the limited electric tuning capability, and the limited intermediate frequency (IF) bandwidth of a practical mixer [1], an additional frequency tuning possibility for a given QCL using an external dielectric layer would be extremely useful. Such a demand is justified by the fact that producing a high quality third-order DFB QCL is inherently a costly and time consuming process, because of the requirement for molecular beam epitaxial (MBE) growth and complex multi-layer structure of the QCLs.

Continually tuning the frequency of a QCL by condensing Nitrogen gas on the laser surface at a cryogenic temperature has been reported [12], and it confirmed this unique property in a laboratory environment. However, for certain applications requiring long-term stability, such as the instrumentation in a space-like environment, alternatives are essential. In this paper we have performed an extensive study of the effect of the dielectric layers of SiO_2 and PMMA on the shift of the lasing frequency. The advantage of the latter is its reversibility, namely the dielectric is removable. By applying full 3D FEM simulations, we identify the importance of the thickness of the dielectric layer on the walls of the laser mesa-structure. Furthermore, we observe a stronger effect of the frequency shift in the 4.7 THz QCL than in the 3.5 THz QCL, which is supported by the simulation.

4.2. QCLs and dielectric layers used

We use third-order DFB THz QCLs with GaAs/AlGaAs active regions based on four-well resonant phonon depopulation scheme [13], at two different frequencies of 3.5 THz and 4.7 THz. A schematic of a third-order QCL is shown in Fig. 4.1a. All the lasers used in this work are based on MBE structures grown at Sandia National Laboratories, but designed and fabricated at MIT. The 3.5 THz QCLs consist of 27 periods over about 1.06 mm in length, with 40 μm in width and 10 μm in height, while the 4.7THz QCLs have 21 periods over a length of about 0.55 mm, with a narrower width of 17 μm and the same height of 10 μm. Multiple lasers are grouped together on a single chip. The SEM photographs of both laser structures are illustrated in Fig. 4.1b.

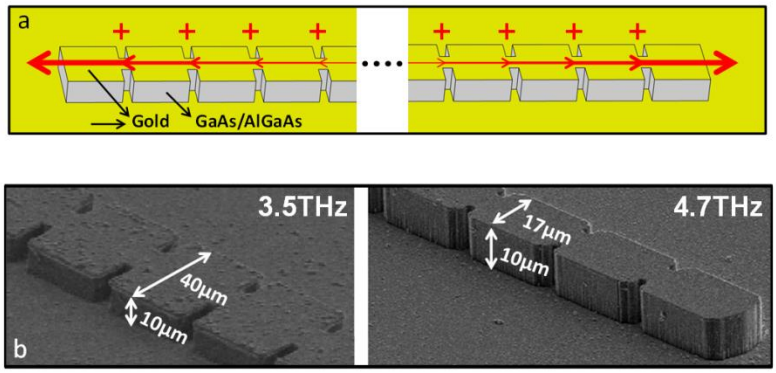

Figure 4.1. a) Schematic of the third-order DFB QCL general geometry, and principle, and THz radiation emission; b) SEM photographs of our experimental 3.5 (left) and 4.7 THz (right) QCLs, consisting of 27 periods of ~ 40 μm long and 21 periods of ~ 27 μm long, respectively.

The tapered horn shape grating of the 4.7 THz DFB laser can make a larger radiation loss for the modes near the upper side of the grating, while reduce the radiation loss for the modes at the other side of the bandgap. The disparity comes from the difference in the relative position between the tip of the tapered horn and the peak field spots inside the laser cavity for both band edge modes.

Effectively, this approach leverages a trade-off between the output power efficiency and mode selectivity. The tip of the tapered horn is designed to be located at one-third of the ridge width away from the edge of the laser ridge and the width of the horn opening is roughly 15 % of the overall DFB periodicity. Based on the power measurements of similar lasers, we expect the maximum output powers of about 0.8 [1] and 0.25 mW [14] for 3.5 and 4.7 THz QCLs, respectively.

Figure 4.2a shows a lateral profile of the EM field inside a third-order DFB waveguide, and in free space, demonstrating how they constructively interfere along the waveguide surface to make a narrow far field beam toward both directions [15], which is also shown by the arrows in Fig. 4.1a. The resonant frequency f of a third-order DFB QCL is determined by the effective refractive index, n_{eff}, through an expression $f= 3c/2n_{eff}\Lambda$ where c is the speed of light in free space and Λ is the period of the grating structure (the length of the sections). So, for a given design, any changes with regard to the electro-magnetic (EM) field surrounding the laser structure, for example, adding a dielectric layer, may affect n_{eff} and can thus change the frequency. This is the essence of the technique for frequency shifting to be applied in this work. To illustrate the physical principle of the changing frequency, we also include simulated electric field distributions around the DFB structures using the full 3D FEM modelling (Fig. 4.2b), where the field extends into the free space, originating from the lateral sides of the laser. The extended field can sense additional dielectric effectively, and therefore increase n_{eff} and consequently decrease the frequency.

As shown in Fig. 4.2b, the field distribution is different in the two lasers. For the 4.7 THz QCL, it is more localized along the period edges which increases the probability to be contacted by a deposited layer, whilst for 3.5 THz QCL, it is more concentrated inside and around the air gaps, making the effect weaker, since it covers a smaller portion of the entire lateral area. The effect strength mainly depends on the ratio between the wavelength and the laser width, which is larger for the 4.7 THz QCL, suggesting a larger frequency shift for this laser for the same

dielectric layer. Detailed simulation of the frequency shift as a function of a dielectric layer will be described later for comparison with the experimental results.

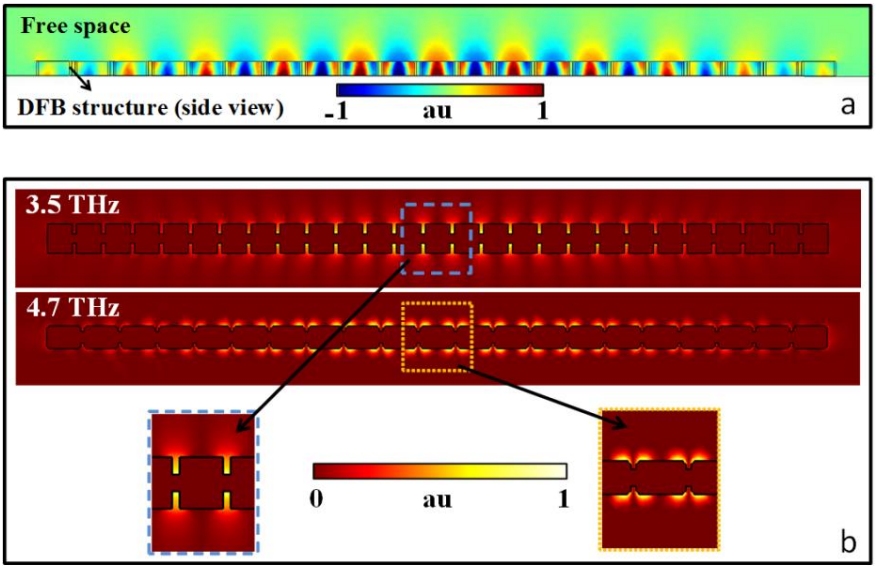

Figure 4.2. a) Side view of the normalized electric field in the DFB structure of 4.7 THz QCL and free space, which constructively interferes for the main mode; b) Top view of the normalized magnitude of the extending electric field to the free space for 3.5 THz (top) and 4.7 THz (bottom) QCLs. Close-up figures show the difference of the field distribution in both lasers.

We focus on two dielectric materials: one is SiO_2 and the other is PMMA. SiO_2 has a reasonable refractive index of ~ 2 at both frequencies of interest [16]. For our purpose, a higher index is favorable. SiO_2 also has relatively low absorption coefficients of ~ 26 and 35 cm^{-1} [16] at frequencies of 3.5 and 4.7 THz respectively. Although lower absorption is preferred, the dielectric layer applied is so thin that the loss is relatively small. Furthermore, use of this material is well known in nanofabrication. We deposit a layer of SiO_2 by RF (Radio-Frequency) sputtering at room temperature (Alliance Concept AC450) and with different thicknesses. A disadvantage however is that, after deposition, SiO_2 cannot be removed without significant risk of damage to the QCL.

PMMA is the other candidate used in this work. It has a refractive index of ~ 1.54 and 1.56 at frequencies of 3.5 and 4.7 THz respectively, but with a higher absorption coefficient of ~ 50 cm^{-1} [17], at both frequencies. The advantage is that the PMMA can relatively easily be removed by Acetone, thus, it is always possible to return the laser to its original frequency. Due to the physical nature of these QCLs, for example, the use of wire bonds for electrical contacts, the usual spin coating deposition of PMMA is unavailable to us. Instead, we add the PMMA by placing a droplet of solvent diluted PMMA onto the laser chip and leaving it to dry in ambient conditions in the lab over night. This forms a layer of solid PMMA covering the laser structure. This process is simple and reliable but with the disadvantage of reduced control over the resulting thickness (relative to spin coating). To reach required thickness, however, one can in principle repeat this process with different PMMA concentrations.

Since all lasers are fine structures with wire bond based devices, it is also prohibitive to use ultrasonic cleaning as would normally be standard prior to SiO_2 or PMMA deposition. But to avoid breaking the bonding wires and damaging metal Au layers, we clean our lasers in hot acetone.

4.3. Measurement setup

We use a pulse tube cooler to operate the 3.5 THz and the 4.7 THz QCL at temperatures of ~ 10 K and ~ 6 K, respectively. We measure the emission spectra of a QCL before and after adding a dielectric layer using a cryogenic Silicon bolometer based Fourier Transform Spectrometer (FTS) with a resolution of ~ 0.6 GHz, and an uncertainty of less than 0.1 GHz. We determine the laser central frequency by fitting the data of the measured spectral line (inset of Fig. 4.3). To make the comparison possible, all the electrical biasing and temperature conditions are kept the same for a given laser in different measurements to make sure that the frequency shift is determined only by the added dielectric layer. All the measurements are performed in the normal laboratory condition (no vacuum). Due

to the relatively long optical path between the QCL and the FTS, we can only select suitable lasers with a frequency well clear of strong, mainly water, absorption lines, which are abundant at these frequencies. To monitor the effect of the dielectric layer on QCL output power, we use a room temperature Pyroelectric detector positioned very close to the window of the cryostat. This avoids the possibility that power measurements are affected by changes in atmospheric absorption due to frequency change.

4.4. Measurement and simulation results

4.4.1. Results on 3.5 THz QCLs

The frequency of the 3.5 THz QCL versus the thicknesses of sputtered SiO_2, varying from 0, 60, 240 and 480 nm, are plotted in Fig. 4.3. The inset shows the corresponding measured, FTS spectra, together with fitted curves for accurately determining the central frequencies. The measured shifts with respect to the original frequency are -2 GHz, -3 GHz and -3.9 GHz, respectively. The SiO_2 thickness is not measured directly from the laser, but from a flat monitor sample, positioned next to the laser during the sputtering deposition.

We assume the measured thickness is the same as one on the top and substrate of the laser, which is referred to the surface layer thickness (blue colour part in Fig. 4.5b). Although the more down shift is observed when the thickness of SiO_2 increases, we observe almost no effect on the output power in comparison with the original value even when the 480 nm thick SiO_2 is added.

We also measured the I-V curves of the lasers before and after deposition (shown in Fig. 4.4), which show a negligible difference. This indicates that the operation properties of the lasers are kept unchanged.

To understand the measured thickness dependence, we perform full 3D FEM simulations using COMSOL 5.1. We take the DFB waveguide structure with the same parameters as the actual laser used, and do the eigenfrequency study in the RF Module to find the resonant frequency. There we can add whatever material

with known characteristics, around the structure and find the effect on the resonance frequency. Input parameters used in simulations are summarized in the Table 4.1.

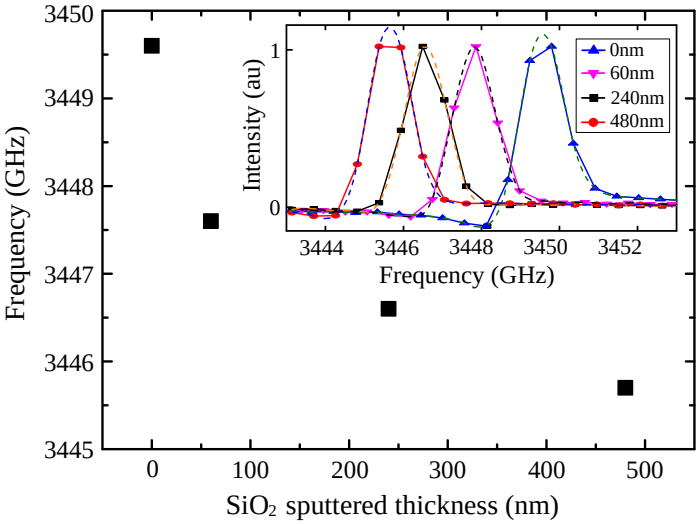

Figure 4.3. Measured frequency as a function of the thickness of the sputtered SiO_2 on the 3.5 THz QCL. The thickness is zero when there is no SiO_2. Inset: Normalized measured FTS spectra without and with three different thicknesses of the sputtered SiO_2. Dashed are fitted curves to find the central frequencies.

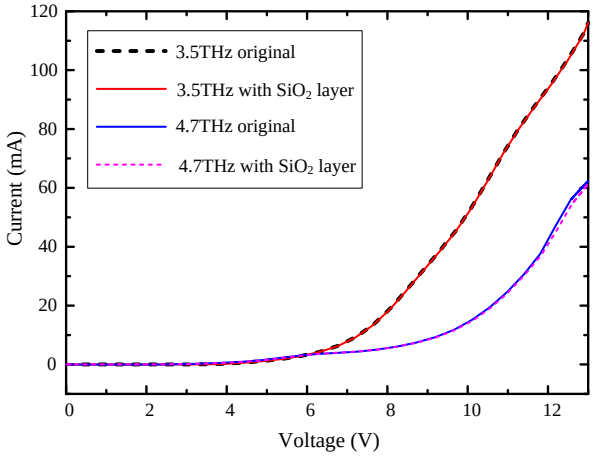

Figure 4.4. Measured I-V curves of both lasers before and after SiO_2 deposition.

Parameter	Value for 3.5THz QCL	Value for 4.7THz QCL
Laser width	40 µm	17 µm
Laser height	10 µm	10 µm
Period length	40 µm	27 µm
Number of periods	27	21
Slit opening length	5.8 µm	2.5 µm
SiO_2 refractive index	2	2
SiO_2 absorption coefficient	26 cm^{-1}	35 cm^{-1}
PMMA refractive index	1.54	1.56
PMMA absorption coefficient	50 cm^{-1}	50 cm^{-1}

Table 4.1. Simulations input parameters

To obtain the thickness of the SiO_2, it is less straight forward. This is because we only know the surface layer thickness, but not the layer thickness on the walls of the waveguide structure (lateral layer thickness, the area shown in orange in Fig. 4.5b), which can depend on the details of the sputtering process and also of the surface condition of the laser before the deposition. However, it is common knowledge that the lateral thickness should be smaller and even considerable smaller than the surface thickness in a practical sputtering deposition. To establish the frequency shift as a function of the lateral layer thickness, we simulate it for different surface thicknesses of SiO_2 on the 3.5 THz QCL including our measured points at 60, 240, and 480 nm. The results are plotted in Fig. 4.5a. Based on the calculated dependences, we find that the lateral thicknesses in our case are ~ 2, 5, and 20 nm, respectively, by matching the calculated frequency shift to the measured one.

Figure 4.5a shows that the frequency shift has approximately a linear dependence to the lateral layer thickness with a rate of ~ 40 MHz/nm for a fixed surface layer thickness around our experimental values. As it's shown in Fig. 4.5b, above a certain range of the initial surface layer thickness (~ 100 nm) where the effect is larger, the shift is mainly determined by the lateral layer thickness, while

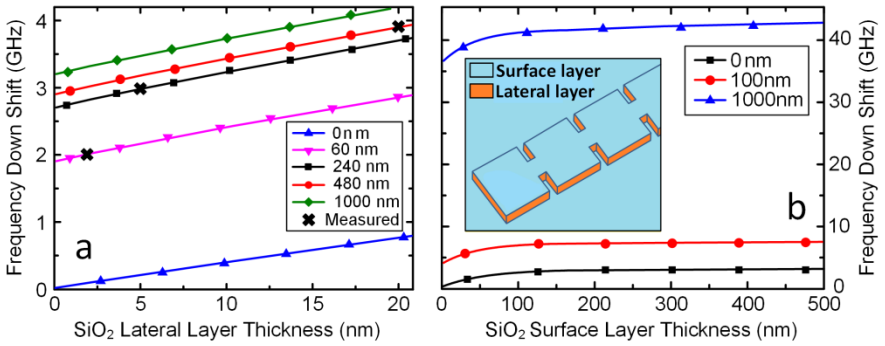

Figure 4.5. a) The simulation results of the frequency down shift for the 3.5 THz QCL vs the lateral layer thickness of the sputtered SiO_2, in different surface layer thicknesses, together with the measured data; b) Simulated frequency downshift vs surface layer thickness of SiO_2 on a 3.5 THz QCL, in different lateral layer thicknesses. Inset: demonstration of the surface and lateral layers.

the effect due to changing the surface layer thickness in the same scale is negligible. In that region, it shows an almost linear dependence to the surface layer thickness with a coefficient of ~ 1 MHz/nm. We made this graph based on the simulated data points down to 60 nm of the surface layer thickness and the rest down to zero is made by fitting. That initial nonlinear region also implies that the EM field is being rapidly attenuated by the vertical distance from the top surface whilst in the lateral sides it remains almost unchanged over ~ 1 µm away from the wall surface.

Alternatively, we apply a layer of PMMA as the dielectric layer on a different 3.5 THz laser that has the same structure as the one used previously with SiO_2. A shift of ~ -6.3 GHz is observed experimentally. In contrast to the case of using SiO_2, a drop of ~ 18 % in the output power is observed (from 0.8 to 0.58 mW), which is consistent with the higher absorption of PMMA. The reduction of the output power may also suggest a much thicker layer of PMMA than the SiO_2 used so far. As explained in a previous section, for PMMA deposition, it is difficult to accurately control the thickness. On the laser, it is technically challenging to measure the thickness. However, we think the layer distribution, in comparison with the sputtered SiO_2 with poor wall coverage, can be different. Since the liquid PMMA

covers the laser, evaporating very slowly, it is reasonable to assume that the QCL is homogeneously covered by PMMA on the surface and also on the walls of the laser structure. With this assumption, we can analyze the measurement by applying 3D simulations.

We calculate the frequency shift of the 3.5 THz laser as a function of the PMMA thickness. The dependence is plotted in Fig. 4.6b, together with the experimental data point by matching the frequency shift. We derive the thickness of PMMA to be 340 nm in our case.

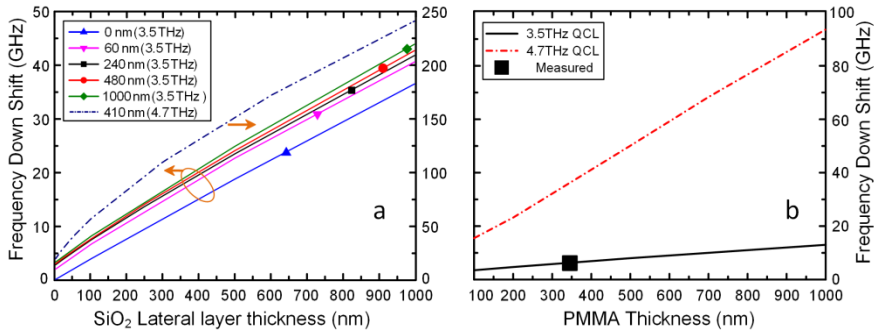

Figure 4.6. a) The simulation results of the frequency down shift of the 3.5 THz QCL vs the lateral layer thickness of the sputtered SiO_2, up to 1 µm, in different surface layer thicknesses, and the same curve for the 4.7 THz QCL with the measured surface thickness of 410 nm; b) The simulated frequency down shift of the 3.5 THz QCL and also the 4.7 THz QCL as a function of PMMA layer thickness, which are assumed to be coated uniformly across the laser structure.

The calculated down shift as a function of PMMA thickness allows an estimate of the frequency shift rate, which is nearly constant and is about 10 MHz/nm. The shift rate, being a factor of 4 lower than that found in the SiO_2 simulation, is due to the lower refractive index of PMMA (~1.54) compared to SiO_2 (~2). In addition, a higher absorption coefficient that attenuates the EM field more strongly as it enters into the PMMA layer, can reduce the influence of the layer on the effective refractive index of the laser.

4.4.2. Results on 4.7 THz QCLs

Now we describe experiments to add a similar dielectric layer to 4.7 THz QCLs. The frequency of these QCLs is motivated by the development of heterodyne receivers to observe the astronomically important neutral oxygen [OI] line at 4.745 THz. We start with a relatively fresh 4.7 THz QCL, like the 3.5 THz QCLs used, by sputter growing a layer of 410 nm SiO_2 on the surface and found a frequency shift of ~ -13.3GHz, which seems to have a much stronger effect than what we observed for the 3.5 THz QCL (nearly 3 times larger down shift for a comparable thickness of SiO_2). Before describing the simulation, we also noticed that the output power after the deposition of SiO_2 had a reduction of about 20 %. This may be partly due to the increased absorption loss in the SiO_2 at this frequency [16], and may be partly due to the fact that the EM field is more strongly interacting with the added material, as expected from the simulation result shown in Fig. 4.2b.

To understand the result obtained with the 4.7 THz QCL, we have repeated the simulation using the 3D simulator in COMSOL with the input parameters adjusted to match the actual QCL. The down shift of the frequency as a function of the lateral layer thickness for the surface layer thickness of 410 nm is shown in Fig. 4.6a. To derive the lateral thickness, we try to match the down shift in the simulated curve where we find that the experimental data point does not fit. In other words, even with zero lateral thickness used in the simulation, we already have a larger down shift than had been observed experimentally. We attributed these results to the problematic surface condition of this laser, which is different from that of the 3.5 THz QCL. The unknown surface condition can reduce the effect of the dielectric on the frequency in two ways: it may absorb considerably the EM field, reducing the effect of additional SiO_2 or PMMA layer, and it prevents them to adhere on the walls of the laser structure.

We have also performed the same experiments using a second 4.7 THz QCL, which has been frequently tested experimentally so far, and is known to suffer from surface contamination. We have sputtered SiO_2 and also applied PMMA to

this laser, however, we observe a weaker effect, not more than -3 GHz shift which confirms the crucial role of the laser surface condition. It is worth to stress that we do perform the normal cleaning procedure using acetone, but it seems to be not as effective at cleaning-up severe contamination in our case. Applying more aggressive cleaning techniques like Oxygen plasma or acetone with ultrasound agitation is not applicable because of the potential to damage the lasers.

Comparing to the same graphs of the frequency down shift vs deposited SiO_2 lateral layer thickness, for the 3.5 THz QCL in Fig. 4.6a, the simulation result for 4.7 THz QCL shows much larger effect, characterized by a rate of 200 MHz/nm. It confirms the intuitive estimation by taking the different outward extended EM distribution of a 4.7 THz QCL into account. This is also confirmed by the simulation for the effect of a homogeneous PMMA layer on a 4.7 THz QCL, plotted in Fig. 4.6b, where it shows a coefficient around 88 MHz/nm, being more than 8 times larger comparing to the 3.5 THz laser.

4.5. Discussion

The experimental results from the 3.5 THz QCL show that with a layer of sputtered SiO_2, one can down shift the frequency of the laser. It also shows that with the simulations, the effect of the lateral layer thickness of the SiO_2 is dominated comparing to the surface layer thickness. The typical frequency shift rate is about -40MHz/nm. Knowing this, one can try to sputter a layer of SiO_2 when the laser is positioned with an angle (or tilted), so that the material can more effectively be deposited on the side walls instead of on the top of the laser. If the surface thickness of SiO_2 is not far from 500nm, the loss is still negligible, so the output power is affected minimally. The dielectric layer based on PMMA is easily introduced. As we have shown, a -6GHz frequency shift can be realized with negligible power loss. This approach offers a reversible process, so one can always remove the PMMA to recover the original frequency. It is interesting to note that during limited thermal cycling of the QCL with PMMA, we do not see the change

with regard to the frequency.

We have performed an extensive study on the effect of SiO_2 and PMMA on the frequency shift of third-order DFB QCLs at 3.5 THz. We however can present only a few experimental data points since we have limited number of QCLs available for such experiments which are uniquely designed to be served as local oscillators in certain space applications. Nevertheless, we confirm and establish the frequency dependence on the additional dielectric layers of sputtered SiO_2 and PMMA in combination with the 3D simulation.

Although the simulation for the 4.7 THz QCLs is informative itself, it is unable to match the experimental result because of the problematic laser surface condition e.g. contamination. However, as a by-product, we realize that the surface condition of the laser before the deposition of SiO_2 is crucial and the fresh lasers are preferable for the change of the frequency by such a technique. The measured frequency shift of about -13GHz together with the simulation results, show that the 4.7 THz QCL due to the strong extension of the EM field to the free space is more sensitive to the presence of a dielectric layer as well as the presence of the contamination. In practice, we have observed measurable down shifts due to the contamination caused, for example, by an oil pumping system. So, to maintain the frequency of as-produced QCL, one should prevent the contamination.

Conclusion

We have extensively studied the frequency down shift of third-order DFB QCLs at 3.5 THz as a function of the thickness of a dielectric layer of either sputtered SiO_2 or PMMA. We observed that both materials can effectively down shift the lasing frequency. Taking advantage of the 3D FEM simulations, we study the frequency dependence on the layer thickness both on the flat surfaces and lateral sides of the structure, where we realize that the latter dominates the frequency shift. SiO_2 is recommended when a high down shift with high accuracy is desired, whilst PMMA is the choice if the frequency shift has to be reversible since it is easily removable. The knowledge provides a guideline to shift the frequency of an existing QCL used

as a local oscillator in practical applications. We have performed a similar study also on the third-order DFB QCLs at 4.7 THz and observed a larger frequency shift, supporting the prediction of the 3D FEM simulation. However, due to the surface contamination no consistent experimental dependence was established.

Bibliography

[1] J. L. Kloosterman, D. J. Hayton, Y. Ren, T. Y. Kao, J. N. Hovenier, J. R. Gao, T. M. Klapwijk, Q. Hu, C. K. Walker, and J. L. Reno, "Hot electron bolometer heterodyne receiver with a 4.7-THz quantum cascade laser as a local oscillator," Appl. Phys. Lett. **102**, 011123-1 (2013).

[2] H. Richter, M. Wienold, L. Schrottke, K. Biermann, H. T. Grahn, H. W. Hubers, "4.7-THz Local Oscillator for the GREAT Heterodyne Spectrometer on SOFIA," IEEE Trans. Terahertz Sci. Technol. **5**, 539 (2015).

[3] S. Fathololoumi et al, "Terahertz quantum cascade lasers operating up to ∼ 200K with optimized oscillator strength and improved injection tunneling," Opt. Express **20**, 3866 (2012).

[4] M. Brandstetter et al, "High power terahertz quantum cascade lasers with symmetric wafer bonded active regions", Appl. Phys. Lett. **103**, 171113-1 (2013).

[5] M. I. Amanti, G. Scalari, F. Castellano, M. Beck, and J. Faist, "Low divergence Terahertz photonic-wire laser," Opt. Express **18**, 6390 (2010).

[6] T. Y. Kao, Q. Hu and J. L. Reno, "Perfectly phase-matched third-order distributed feedback terahertz quantum-cascade lasers", Opt. Lett. **37**(11), 2070 (2012).

[7] Q. Qin, B. S. Williams, S. Kumar, J. L. Reno, and Q. Hu, "Tuning a terahertz wire laser," Nature Photon. **3**, 732 (2009).

[8] J. Xu, J. M. Hensley, D. B. Fenner, R. P. Green, L. Mahler, A. Tredicucci, M. G. Allen, F. Beltram, H. E. Beere, and D. A. Ritchie, "Tunable terahertz quantum cascade lasers with an external cavity," Appl. Phys. Lett. **91**, 121104-1 (2007).

[9] F. Castellano, V. Bianchi, L. Li, J. Zhu, A. Tredicucci, E. H. Linfield, A. G. Davies and M. S. Vitiello, "Tuning a microcavity-coupled terahertz laser," Appl. Phys. Lett. **107**, 261108-1 (2015).

[10] D. Turcinkova, M. I. Amanti, G. Scalari, M. Beck, J. Faist, "Electrically tunable terahertz quantum cascade lasers based on a two-sections interdigitated distributed feedback cavity," Appl. Phys. Lett. **106**, 131107-1 (2015).

[11] B. S. Williams, S. Kumar, H. Callebaut, Q. Hu, and J. L. Reno, "Terahertz quantum-cascade laser at λ≈100 μm using metal waveguide for mode confinement," Appl. Phys. Lett. **83**, 2124 (2003).

[12] D. Turčinková, M. I. Amanti, F. Castellano, M. Beck and J. Faist, "Continuous tuning of terahertz distributed feedback quantum cascade laser by gas condensation and dielectric deposition," Appl. Phys. Lett. **102**, 181113-1 (2013).

[13] B. S. Williams, S. Kumar, Q. Hu, and J. L. Reno, “Resonant phonon terahertz quantum-cascade laser operating at 2.1 THz (λ ≈ 141 μm),” Elec. Lett. **40**, 431 (2004).

[14] Y. Ren, D. J. Hayton, J. N. Hovenier, M. Cui, J. R. Gao, T. M. Klapwijk, S. C. Shi, T. Y. Kao, Q. Hu, and J. L. Reno, “Frequency and amplitude stabilized terahertz quantum cascade laser as local oscillator,” Appl. Phys. Lett. **101**, 101111-1 (2012).

[15] N. van Marrewijk, B. Mirzaei, D. Hayton, J. R. Gao, T. Y. Kao, Q. Hu, J. L. Reno, “Frequency Locking and Monitoring Based on Bi-directional Terahertz Radiation of a third-Order Distributed Feedback Quantum Cascade Laser,” J. Inf. Mil. THz Waves. **36**, 1210 (2015).

[16] E. D. Palik, “*Handbook of optical constants of solids*,” (Orlando, FL: Academic Press, 1985), p. 753.

[17] P. D. Cunningham et al, “Broadband terahertz characterization of the refractive index and absorption of some important polymeric and organic electro-optic materials”, J. Appl. Phys. **109**, 043505-1 (2011).

5

EFFICIENCY OF MULTI-BEAM FOURIER PHASE GRATINGS AT 1.4 THZ*

We compare the results of simulated and measured power efficiency and far-field beam pattern, for two reflective Fourier phase gratings, designed to generate 2 × 2 and 2 × 4 beams respectively from a single-beam, coherent source at 1.4 THz. The designed surface structures were manufactured on aluminum plates by a computer numerical control (CNC) micro-milling machine. Despite small differences between the designed and fabricated gratings, we measured power efficiencies of both gratings to be around 70 %, which is in a good agreement with the simulated values. We also find a good agreement between the simulated and measured diffracted beam size and spatial distribution. We demonstrate the application of both gratings as multiple beam local oscillators to simultaneously pump (or operate) a 4-pixel array of superconducting heterodyne mixers.

* Published as B. Mirzaei, J. R. G. Silva, Y. C. Luo, X. X. Liu, L. Wei, D. Hayton, J. R. Gao and C. Groppi, Optics Express **25**(6), 6581 (2017).

5.1. Introduction

Terahertz heterodyne receivers, typically consisting of a superconducting mixer and a coherent local oscillator (LO) source, are approaching quantum-noise limited sensitivity [1,2]. Therefore, to further improve spatial observing efficiency, multi-pixel heterodyne receivers [3] are necessary, in particular, for sky mapping from astronomical telescopes. Historically, the utilization of large, multi-pixel heterodyne arrays has been held back by the cost and high complexity of multi-beam, frequency or phase matched, local oscillators. One approach is to generate multiple beams from a single beam source by manipulation of its phase by means of a phase grating [4,5]. Considering the challenges in providing suitable THz sources and complexities to synchronize the frequency or phase of many individual sources, this approach is more favourable and practical than providing each pixel with a separate LO. For the application of such a grating, a key figure of merit when converting a single beam into multiple beams is the power efficiency of the conversion, that is, the ratio between the total power of the resulting multiple beams and that of the input single beam.

A phase grating consists of a periodic structure made up of unit cells whereby each cell modulates the phase of the incident electro-magnetic wave in order to produce a series of diffraction orders with different traveling angles. The intensity and angular distribution of the diffraction orders are determined by the unit cell modulation pattern and size. To effectively match the beam pattern to that of a mixer array, additional optics, such as a parabolic mirror or lens, is typically needed for both properly collimating the diffracted beams and controlling spatial distribution.

Since the first grating design for 90-110 GHz [6], several milestones have been reached towards developing THz phase gratings. Sorting by the operating frequency, the following phase gratings have been reported: 7-pixel grating at 345 GHz has been realized with 80 % efficiency [7], 8-pixel grating at 500 GHz with 83 % efficiency [8], 8-pixel grating at 490 & 810 GHz [9] and 3-pixel grating at 1.1 THz

[10]. Beyond these frequencies, little work can be found in the literature. Although a 7-pixel grating at 1.9 THz has been reported [11] no information on the grating measurements and analysis has been given.

Although waveguide based multiple beam generators [12,13] may provide high efficiency, very few experiments are found in the literature. Furthermore, manufacturing of the waveguides, in particular, at the supra-THz frequency range (>1 THz), such as the frequency band centered at 4.7 THz, which is significant for astronomical applications, becomes increasing difficult and costly. Moreover, this approach has also difficulties to make use of existing sources, such as quantum cascade lasers [14]. Therefore, we choose to develop a phase grating, namely with a quasi-optical coupling to a mixer array approach in contrast to the waveguide approach. In this work we present two different phase gratings of 4 and 8-pixels, designed to operate at 1.4 THz. This frequency was chosen because of the availability of a high power gas laser source, facilitating the experimental study of the grating with the goal of improving understanding of the performance, namely the efficiency and the spatial distribution of diffracted beams by comparing the simulations with measurements.

5.2. Fourier phase gratings, design and manufacturing

In a Fourier phase grating, the surface topology of a unit cell is derived based on a Fourier series with a certain number of coefficients. Increasing this number in the design makes the calculated surface structure closer to the ideal, leading to greater power efficiency. However, to balance accuracy of the end result with increasing computation demand, we typically limit the calculation to 13 Fourier coefficients to design our gratings, which ensure at least 98 % of the maximum achievable efficiency if an infinite number of coefficients were to be used [5]. Having built a proper algorithm in MATLAB, we find 13 coefficients to satisfy the following condition for 2 and 4 diffraction orders in one dimension (1D), respectively: $\sum_{i=\pm1}(p_i-\frac{1}{2})^2<0.01$ and $\sum_{i=\pm1,\pm3}(p_i-\frac{1}{4})^2<0.01$, where pi is the fractional power of the

i'th diffraction order. By minimizing these summations, we come up with final selected coefficients. The 2D surface profile of a unit cell is then generated by superimposing two sets of such 1D Fourier coefficients orthogonally. Therefore, the power efficiency is calculated by the product of summation of all fractional powers in both directions.

The divergence angle of the diffracted beams is inversely proportional to the unit cell size. The direction of each diffraction order can be calculated by the expression, $\sin\beta = \sin\alpha + m\lambda/\Lambda$, where Λ is the side length of the square unit cells, which also defines the periodicity of the grating, α and β are the angles of incidence and the m'th diffraction order, respectively. Both angles are with respect to the normal incidence on the grating. In this work, we chose a unit cell with an area of 2 × 2 mm^2 (Λ = 2 mm) to reach a suitable angular distribution of the diffracted beams, to be measurable with available experimental setup, and also for later matching a mixer array. Figure 5.1 shows the surface profiles of unit cells in 3D, designed for 4 (2 × 2) and 8 (2 × 4)-pixel gratings which are repeated 15 times in two orthogonal directions to form the gratings with a total area of 30 × 30 mm^2. We note that the design of the 4-pixel grating and the initial measurements have been reported by us previously in [15].

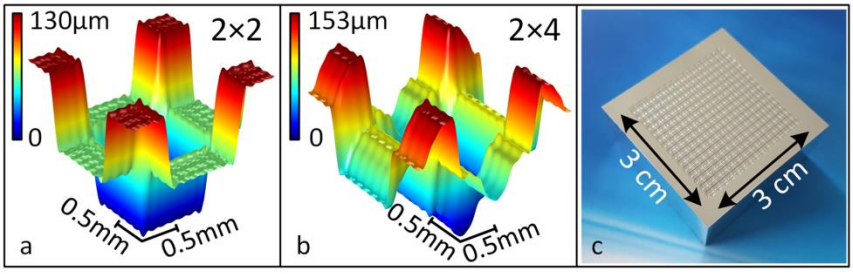

Figure 5.1. 3D surface profiles of unit cells of 4 (a) and 8-pixel (b) gratings with exaggerated z axis and a photograph of the manufactured 8-pixel grating (c).

Unlike traditional Dammann gratings with sharp step like variations in the surface structure [16], the smooth and continuous surface of the Fourier phase

gratings can be accurately machined on a metallic plate to make a reflection grating. A KERN EVO micro-milling machine with a ball end mill is used to transfer the designed pattern onto aluminum, which is expected to have more than 99 % surface reflectivity at THz frequencies [17]. A micrograph of the manufactured 8-pixel grating is also shown in Fig. 5.1. The manufacturing accuracy is limited by the radius of the ball end-mill machine tool, which defines the minimum radius of curvature that can be patterned. Ideally, the latter should match to the designed value. In practice, the minimum radius of curvature becomes smaller with a larger number of Fourier coefficients, i.e. appearance of finer-scale variation with smaller unit cell size, i.e. lateral compression of the profile and also with longer operating wavelength requiring greater profile depth. The minimum radius of curvature of our 4 and 8-pixel grating designs are 122 and 106 µm, respectively. In contrast, the smallest available radius of the diamond ball end-mill used is only 300 µm. Therefore, we do not expect the designed profile to be fully reproduced in manufacturing. Figure 5.2 shows two cross sections or surface profiles measured orthogonally from a unit cell of the manufactured 8-pixel grating, together with the designed profiles, for comparison. Although there are some small deviations, less than 3 µm in amplitude, the main topology is reasonably realized.

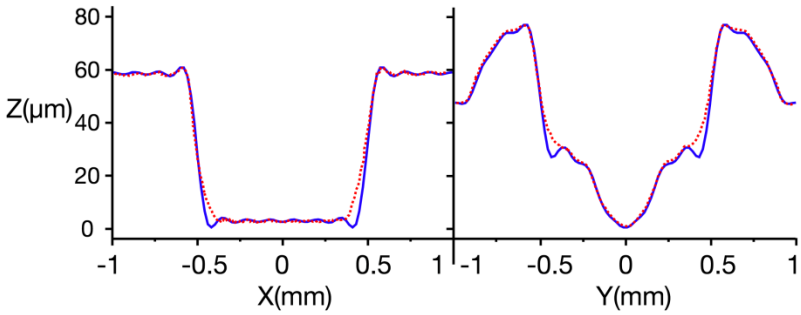

Figure 5.2. Two cross sections or surface profiles measured orthogonally from a unit cell of the manufactured 8-pixel grating (dashed), together with the designed profiles (solid), for comparison (corresponding to the 3D profile shown in the middle of Fig. 5.1). Here Z is the vertical direction of the grating.

An alternative manufacturing route is the 3D printing [18] technique, which has been successfully applied for the THz plastic lenses. The expected challenge is the material, which has to be a highly conductive metal, such as pure Al with extremely fine structure.

5.3. Simulation and measurement results

We use the RF module of COMSOL to fully simulate the 3D performance of the designed gratings in order to compare with the measured results. To calculate the efficiency, we input the surface morphology of a unit cell into the model and apply periodic port and boundary conditions to simulate the entire grating. There we can derive the direction and configuration of the diffracted beams as well as the power fraction of each individual order and the total grating power efficiency. However, this approach does not produce the far-field beam pattern. In order to do so, we model the entire grating by repeating the unit cell geometry in both orthogonal directions. Although this demands more processing time (30 versus 15 minutes), the advantage of this approach is that we are able to perform the simulation using the same parameters as in the experiment, i.e. the shape of the incoming beam and the number of illuminated unit cells. In practice, we apply five processors of 2.5 GHz, each with a memory of 6.4 Gb.

Figure 5.3 illustrates the measurement setup used to characterize the 8-pixel grating. We use a far infrared (FIR) gas laser operating at 1.4 THz to generate the incoming beam to the grating. The laser beam illuminates the grating through a focusing lens (with 250 mm focal distance) and with an incident angle of θ. The incident beam pattern mapped at the equivalent position of the grating is depicted in Fig. 5.4f, where it can be seen that the beam has a non-uniform intensity distribution, characterized with two peaks, originated from the output of the gas laser, with an area covering about 12 unit cells on the grating.

We measure the output beams diffracted by the grating by scanning a pyro-electric detector, mounted on a X-Y motor controlled translation stage. The

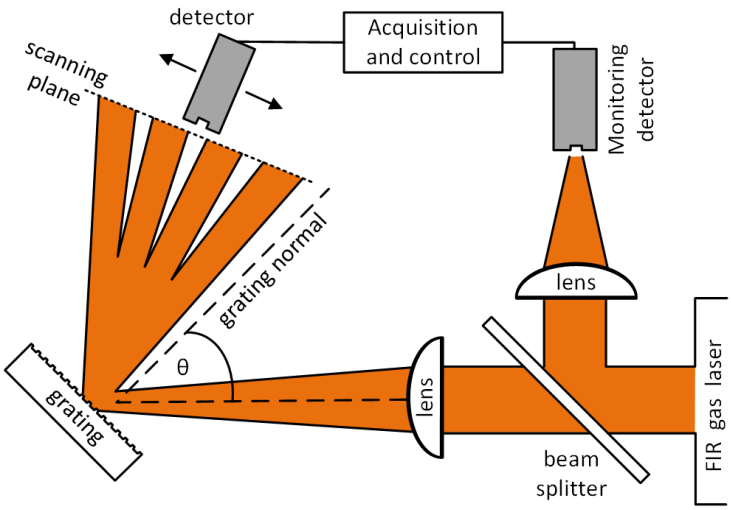

Figure 5.3. Schematic view of the experimental setup for measuring the beam patterns diffracted from the grating.

scanning plane is 60 mm away from the grating and is normal to the imaginary line drawn from the centre of the grating to the centre of the beam pattern, ensuring symmetric results. The lens is chosen as such to produce a focal point at the scanning plane, giving cleaner measured diffracted beams. Because the entrance aperture of the pyro-electric detector is 2 mm in diameter, we choose 1 mm as the scanning step size to effectively scan the whole target area. Since the output power of the gas laser fluctuates in time, we introduce a beam splitter and an additional pyro-electric detector to monitor the instantaneous power as reference to correct the fluctuations in the acquired diffracted beam pattern.

We repeat the measurement for two different incident beams with orthogonal azimuth angles, by 90° rotation of the grating on the fixed plane. To distinguish these two cases, we show the arrows schematically to represent the diffracted beams, each with a different colour, as well as the incident beam in red, in Figs. 5.4a and 5.4b, which are the results from the 3D simulations in COMSOL. The measurement results for the case of $\theta = 25°$ are plotted in the left side of Figs. 5.4c and 5.4d, corresponding to the cases shown in Figs. 4(a) and 4(b), respectively. We

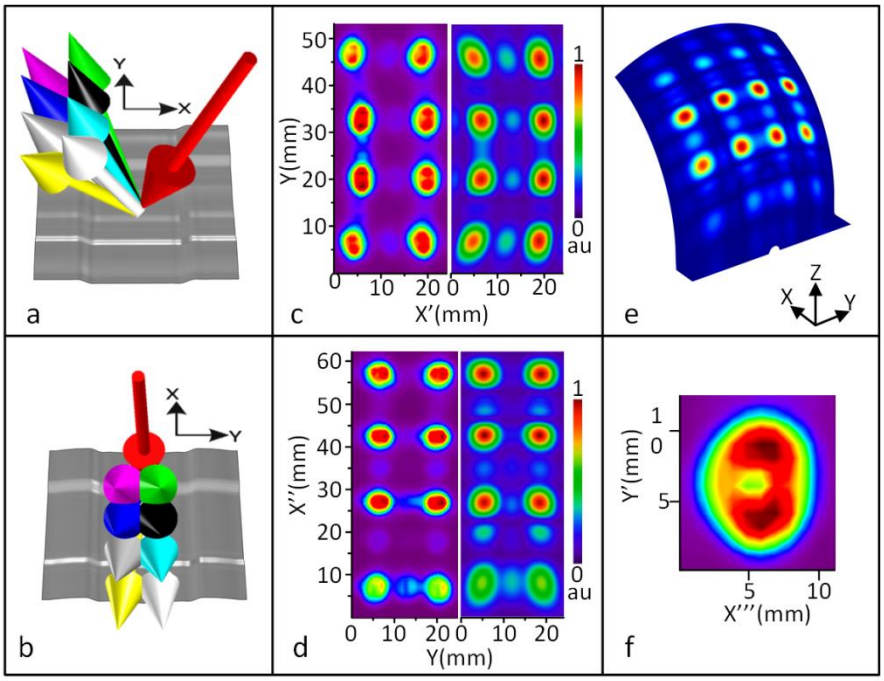

Figure 5.4. a,b) Arrow schematics illustrate the simulation results of diffraction orders, corresponding to two incident beams with 90° azimuth angle difference on the 8-pixel grating; c,d) Planar measured (left) and simulated (right) far-field beam patterns at 60 mm from the grating with incident beams corresponding to (a) and (b) respectively; e) the simulated far-field beam pattern of the case corresponding to (a) shown on a spherical surface; f) Measured incident beam on the grating.

find that in the first case (Fig. 5.4c) the power is more uniformly distributed among the diffracted beams, which are symmetrically distributed in space, making it more favorable for the application as local oscillator for a mixer array. For comparison, the simulation results are plotted next to the measured results in Figs. 5.4c and 5.4d, where they show a good agreement in terms of the diffracted beam distribution and the size of the beam pattern. The cause of the different beam patterns produced by different applied incident beams is the unit cell profile asymmetry of the 8-pixel grating. In fact, the projection of the incident beam on the grating surface is perpendicular to 1 × 2 (Fig. 5.2 left) for the first incident beam and to 1 × 4 (Fig. 5.2 right) grating 1D profile for the second incident beam. It is

worth mentioning that in the simulation, we take the same size as the experimental incident beam, but with a single Gaussian-like profile instead of the double peaked beam produced by the gas laser. Because of this, the simulation does not reproduce the exact shape of the experimental diffracted beams.

Since the beam patterns are measured along a flat, not a spherical plane, they look slightly distorted and stretched. For clarity, the simulated beam pattern in Fig. 5.4c, is plotted on a spherical surface and included in Fig. 5.4e, which illustrates clearly that the beams are actually distributed in straight rows and columns.

To obtain the efficiency experimentally, we integrate the measured intensity of all 8 beams, excluding other orders, and divide it by the integrated intensity of the incoming beam at the grating position. Taking the air absorption in the optical path between the grating and the scanning plane into account, we end up with a measured efficiency of 73 ± 1 %. The 2 % uncertainty originates from both the air loss estimation and the background noise of the pyro-electric (room temperature) detector. Comparing to the expected values of 73.8 % from the 3D COMSOL simulations and 72 % from the Fourier series calculation in the design, for the same incident angle (θ = 25°), we conclude that the measured efficiency is in good agreement with that predicted by the simulations.

An interesting question is: how much does the deviation of the manufactured grating surface structure from the design affect the efficiency? For this, we perform the simulation, by taking the measured grating surface profile as the input to the 3D COMSOL, where we find a drop of about 0.3 % in the efficiency and a negligible difference in the beam pattern, calculated using the designed surface profile. Taking advantage of this capability in COMSOL simulations, allows us to conclude for the first time that, even with non-ideal machining, one can reach nearly the theoretically predicted efficiency and beam pattern. This conclusion has a high impact on the manufacturability of a grating, making its fabrication less critical.

We also study the effect of different incident angles θ on the far-field angular and power distributions of the diffracted beams and on the grating power

efficiency, for the case corresponding to Fig. 5.4a. The simulation results are plotted in Fig. 5.5 for four incident angles of 15°, 20°, 25° and 30°, where each sub-figure contains the azimuth angle and the elevation angle with respect to the grating surface, together with the power fraction of all diffracted beams that are separated by circles filled by different colours, corresponding to the arrows in Fig. 5.4a. This figure shows that by increasing the angle with respect to the normal incidence, the power distribution becomes less uniform whilst the power efficiency decreases negligibly by less than 2 %.

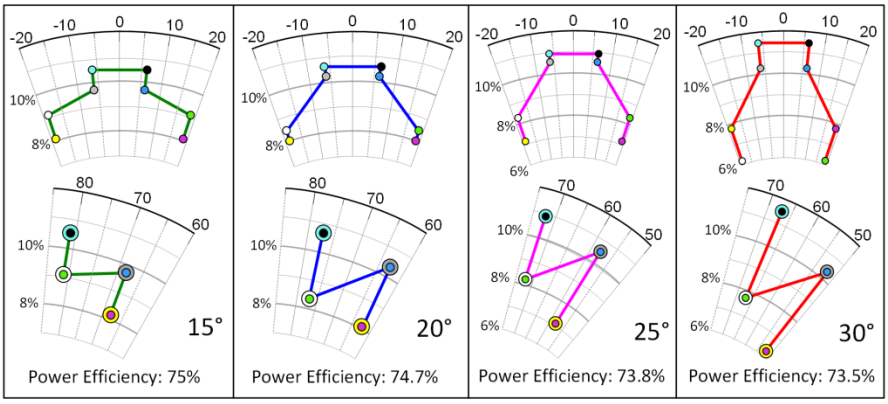

Figure 5.5. Angular and power distributions of diffracted beams for the case shown in Fig. 5.4a, for four different incident angles. The power fractions in the top and bottom plots of each section are shown versus the azimuth angle and the elevation angle with respect to the grating surface, for different diffracted orders, respectively. Each diffraction order is distinguished by the colour of the corresponding arrow in Fig. 5.4a. In the elevation angle plots, the doubled circles indicate the overlapping of two corresponding diffracted beams.

We apply a similar measurement setup, to characterize the beam pattern of the 4-pixel grating. Figure 5.6 shows the measured incident beam on the grating with θ = 25°, and also the measured and simulated diffracted beams, both of which are at a plane, being 12 cm away from the grating. Very similar overall beam shapes and sizes show a high correlation between the measurements and simulations. All diffracted beams actually duplicate the detailed profile of the incident beam.

To derive the efficiency of the 4-pixel grating, we apply a slightly modified

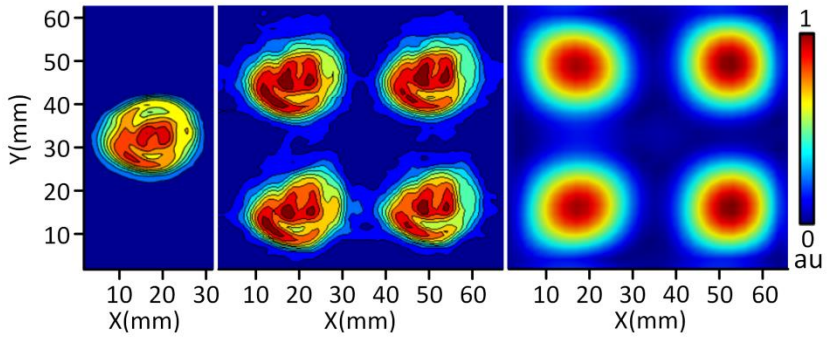

Figure 5.6. Measured incident beam (right) and measured (middle) and simulated (right) diffracted beam patterns of the 4-pixel grating at a plane, which is 12 cm away from the grating. Small differences in the measured beam profiles are likely due to the FIR laser, the profile of which is found to vary in time.

measurement setup, where two identical lenses with 50 mm focal distance were used, one placed before the grating, and the other between the grating and the scanning plane to collimate the diffracted beams, which are needed to match those of a mixer array as described in the following paragraph. Using an integration similar to the 8-pixel grating case, we derive an efficiency of 66 ± 1%, where 2% uncertainty comes from the loss calculation of the lens. COMSOL simulation and the calculation in design predict power efficiencies to be 66.4% and 65%, respectively, which again show a good agreement to the experimental value.

To complete the study, we implement both gratings in a heterodyne experiment using a 2x2 HEB mixer array. We apply the 4-pixel grating together with the 1.4 THz gas laser to optically pump the array. Since we have no 8-pixel mixer array available, we examine the 8-pixel grating by coupling three groups of four left, four centre or four right beams to the array. We succeeded in pumping all the mixers to reach their optimal (for the best sensitivity) operating current-voltage curves simultaneously. Applying the isothermal technique [19] to estimate the beam power at the detector and having estimated all the losses in the optical path from the laser to the mixer array and also taking the efficiency of the grating into account, we end up with about 25 µW for the total required input power, and

about 50 μW for an 8-pixel mixer array. This order of power is reachable at lower frequencies (< 2 THz) by multiplier based solid state sources [13] and at higher frequencies by quantum cascade lasers [14].

5.4. Conclusion

We modelled and also experimentally demonstrated two Fourier phase gratings generating 2 × 2 and 2 × 4 beams from a single, coherent beam at 1.4 THz. Good agreements between the measurements and simulations are found for both the diffracted beam pattern and power efficiency. The measured efficiency is 66% for the 2x2 and 73% for the 2x4 grating, respectively. We also find that the incident angle can affect the distribution of power among the diffracted beams, but affects the efficiency negligibly. Furthermore, we confirm that the diffracted beams of the 4-pixel grating and 8-pixel grating are able to optically pump an array of superconducting HEB mixers. Thus, we demonstrate that the grating is an extremely promising technology for generating a multiple beam local oscillator for a heterodyne array at the supra-THz, required for future astronomic observatories, such as NASA Galactic-extragalactic ultra-long-duration spectroscopic stratospheric observatory (GUSTO).

Bibliography

[1] W. Zhang, P. Khosropanah, J. R. Gao, E. L. Kollberg, K. S. Yngvesson, T. Bansal, R. Barends, and T. M. Klapwijk, "Quantum noise in a terahertz hot electron bolometer mixer," Appl. Phys. Lett. **96**(11), 111113 (2010).

[2] B. D. Jackson, A. M. Baryshev, G. de Lange, J. R. Gao, S. V. Shitov, N. N. Iosad, T. M. Klapwijk, "Low-noise 1 THz superconductor–insulator–superconductor mixer incorporating a NbTiN/SiO2/AlNbTiN/SiO2/Al tuning circuit," Appl. Phys. Lett. **79**(3), 436 (2001).

[3] C. Walker, Terahertz Astronomy (CRC, Taylor & Francis Group, 2016), Chap. 5&6.

[4] J. A. Murphy, C. O. Sullivan, N. Trappe, W. Lanigan, R. Colgan and S. Wittington, "Modal Analysis of the Quasi-Optical Performance of Phase Gratings," Int. J. Inf and Mill Waves, **20**(8), 1469 (1999).

[5] U. U. Graf and S. Heyminck, "Fourier gratings as submillimeter beam splitters," IEEE Trans. Antennas Propag. **49**(4), 542 (2001).

[6] W. Lanigan, N. Trappe, J. A. Murphy, R. Colgan, C. O'Sullivan and S. Withington, "Quasi-optical multiplexing using reflection phase gratings," in Proceedings of the 11th International Symposium on Space Terahertz Technology, University of Michigan (2000).

[7] C. E. Groppi, C. K. Walker, C. Kulesa, D. Golish, A. Hedden, P. Gensheimer, G. Narayanan, A. W. Lichtenberger, U. U. Graf and S. Heyminck, "Desert STAR: A 7 pixel 345 GHz heterodyne array receiver for the Heinrich Hertz Telescope," Proc. SPIE 4855, 330 (2003).

[8] S. Heyminck and U. U. Graf, "Reflection gratings as THz local oscillator multiplexer," Proc. SPIE 4014, 164 (2000).

[9] U.U. Graf, S. Heyminck, E.A. Michael, S. Stanko, C.E. Honingh, K. Jacobs, R.T. Schieder, J. Stutzki and B. Vowinkel, "SMART: the KOSMA sub-millimeter array receiver for two frequencies," in Proceedings of the 13th International Symposium on Space Terahertz Technology, Harvard University (2002).

[10] N. Hurtado, U. U. Graf, H. Adams, "Optics and cryogenics for the 1.1 THz multi-pixel heterodyne receiver for APEX," Proc. SPIE 9153, 915327 (2014).

[11] C. Risacher, R. Güsten, J. Stutzki, H. W. Hübers, D. Büchel, U. U. Graf, S. Heyminck, C. E. Honingh, K. Jacobs, B. Klein, T. Klein, C. Leinz, P. Pütz, N. Reyes, O. Ricken, H. J. Wunsch, P. Fusco, and S. Rosner, "First Supra-THz Heterodyne Array Receivers for Astronomy With the SOFIA Observatory," IEEE Trans. Terahertz Sci. Technol. **6**(2), 199 (2016).

[12] C. Groppi, C. Walker, C. Kulesa, D. Golish, J. Kloosterman, S. Weinreb, G.

Jones, J. Barden, H. Mani, T. Kuiper, J. Kooi, A. Lichtenberger, T. Cecil, G. Narayanan, P. Pu¨tz and A. Hedden, “SuperCam: A 64 pixel heterodyne array receiver for the 350 GHz atmospheric window,” in Proceedings of the 20th International Symposium on Space Terahertz Technology (Charlottesville, 2009), pp. 90–96.

[13] J. V. Siles, R. H. Lin, C. Lee, E. Schlecht, A. Maestrini, P. Bruneau, A. Peralta, J. Kloosterman, J. Kawamura and I. Mehdi, “Development of High-Power Multi-Pixel LO Sources at 1.47 THz and 1.9 THz for Astrophysics: Present and Future,” in Proceedings of the 26th International Symposium on Space Terahertz Technology, Cambridge, MA (2015).

[14] B. S. Williams, “Terahertz quantum-cascade lasers,” Nat. Photonics **1**, 517 (2007).

[15] Y.C. Luo, X. X. Liu, D. J. Hayton, L. Wei, J.R. Gao and C. Groppi, “Fourier phase grating for THz multi-beam local oscillators,” in Proceedings of the 26th International Symposium on Space Terahertz Technology, Cambridge, MA (2015).

[16] H. Dammann and E. Klotz, “Coherent optical generation and inspection of two-dimensional periodic structures,” Int. J. Optics, **24**(4), 505 (1977).

[17] H. Ehrenreich, H. R. Philipp, and B. Segall, “Optical properties of aluminum,” Phys. Rev. **132**(5), 1918 (1963).

[18] W. D. Furlan, V. Ferrando, J. A. Monsoriu, P. Zagrajek, E. Czerwinska, and M. Szustakowski, “3D printed diffractive terahertz lenses,” Opt. Lett. **41**(8), 1748 (2016).

[19] H. Ekström, B. S. Karasik, E. Kollberg and K. S. Yngvesson, “Conversion gain and noise of niobium superconducting hot-electron-mixers,” IEEE Trans Microw. Theory Tech. **43**(4), 938 (1995).

6

8-BEAM LOCAL OSCILLATOR ARRAY AT 4.7 THZ GENERATED BY A PHASE GRATING AND A QUANTUM CASCADE LASER *

We present an 8-beam local oscillator (LO) for the astronomically significant [OI] line at 4.7 THz. The beams are generated using a quantum cascade laser (QCL) in combination with a Fourier phase grating. The grating is fully characterized using a third order distributed feedback (DFB) QCL with a single mode emission at 4.7 THz as the input. The measured diffraction efficiency of 74.3 % is in an excellent agreement with the calculated result of 75.4 % using a 3D simulation. We show that the power distribution among the diffracted beams is uniform enough for pumping an array receiver. To validate the grating bandwidth, we apply a far-infrared (FIR) gas laser emission at 5.3 THz as the input and find a very similar performance in terms of efficiency, power distribution, and spatial configuration of the diffracted beams. Both results represent the highest operating frequencies of THz phase gratings reported in the literature. By injecting one of the eight diffracted 4.7 THz beams into a superconducting hot electron bolometer (HEB) mixer, we find that the coupled power, taking the optical loss into account, is in consistency with the QCL power value.

* Published as B. Mirzaei, J. R. G. Silva, D. Hayton, C. Groppi, T. Y. Kao, Q. Hu. J. L. Reno and J. R. Gao, Optics Express **25**(24), 29587 (2017).

6.1. Introduction

Heterodyne spectroscopy provides valuable scientific information for modern astrophysics, in particular, the process of star formation and the life cycle of interstellar clouds in our own and nearby galaxies. It has the capability to measure molecular and atomic fine structure lines in the super-terahertz frequency region (> 1 THz) [1] including ionized nitrogen [NII] at 1.4 THz, ionized carbon [CII] at 1.9 THz, hydrogen deuteride [HD] at 2.6 THz and neutral oxygen [OI] at 4.7 THz, each containing unique source of information. One important observation is to map particular THz lines in star forming areas within our Milky Way at very high spectral resolution. Such large-scale surveys with velocity-resolved imaging of key fine structure lines require multi-pixel heterodyne receivers [2] with the state-of-the-art mixer performance in order to increase the observation speed and thus the observing efficiency of the telescope. A single heterodyne receiver with extremely high spectral resolving power of 10^6-10^7, consists typically of a mixing detector, a local oscillator (LO), a low noise GHz cryogenic amplifier and a backend GHz spectrometer. Because of the complexity of the receiver and especially the power dissipation of low noise cryogenic amplifiers, the state-of-the-art heterodyne receiver arrays typically have in the order of 10 pixels. Furthermore, very few instruments using multi-pixel receivers have been demonstrated at THz frequencies in the literature.

A multi-pixel heterodyne receiver therefore requires multiple parallel receivers; each pumped with its own LO beam. In general, advanced fabrication technology allows making relatively uniform array of mixers, so that (as will be shown later in this paper) within a certain variation of the LO power they still deliver receiver sensitivities with negligible differences. For generating multiple THz LO beams two approaches have been reported: solid-state waveguide multiple beam generators based on frequency multipliers driven by a common microwave source [3,4], and reflective phase gratings for generating multiple beams by diffracting a single THz source [5,6]. A phase grating is a periodic arrangement of a unit cell with a specific

surface morphology for phase manipulation of the incident coherent radiation. Such a surface profile determines the intensity distribution among the diffracted beams, their angular configuration, and the diffraction efficiency. The latter is defined as the ratio of the total power of the desired diffraction orders to the power of the incoming beam. We will call it efficiency in the rest of the paper.

The choice of the LO technologies depends strongly on the frequency. The neutral oxygen [OI] line at 4.7 THz mostly probes warm natural gas heated by massive newly formed stars [7,8]. As such, it is useful for probing the star formation process, especially when the emission is spectrally resolved. However, because the technology at this frequency is not sufficiently mature yet, it has been relatively less studied so far. Since waveguide based multi-beam LOs have not been demonstrated at such a high frequency, the QCL [9] is the only practical solid-state source at 4.7 THz, which can provide multiple beams in combination with a phase grating. At present, given the power level and beam pattern of the current generation of THz QCLs suitable for use as an LO, such as third order DFB QCLs [10], they can typically only drive a single pixel superconducting hot electron bolometer (HEB) mixer. Progress, however, is rapid enough to overcome these issues soon with the next generation of 4.7 THz QCLs. One could think of using an array of QCLs instead. However, it is in general very challenging to produce multiple lasers with the same frequency. Furthermore, phase or frequency locking of multiple QCLs can be quite complicated.

No detailed study of a phase grating-based LO has so far been published beyond 1.4 THz [11], in which a FIR gas laser was applied. There are two challenges for such a system at higher frequencies. One is the realization of the phase grating since its surface finesse increases by the frequency and becomes more difficult to fabricate. The other is the 4.7 THz QCL with non-Gaussian beam and insufficient output power. Furthermore, the wave fronts of THz QCLs, which are not fully understood [12], might also affect the grating performance.

In this work we report an 8-pixel Fourier phase grating developed for operation at 4.7 THz together with its full characterization using a third order DFB QCL. In

addition to the diffraction beam pattern and efficiency measurements, the power uniformity issue of such a LO array is discussed. We present an experiment of optically pumping an HEB mixer using one of the diffracted beams. The effects of the number of applied Fourier coefficients (FC) on the efficiency and also on the manufacturability of the grating are studied as well. We also demonstrate the grating bandwidth advantage using a FIR gas laser emission at 5.3 THz as the input.

6.2. Grating optimization and realization

A phase grating is formed by 2D repetition of a unit cell with a surface profile determined by the Fourier series based on a limited number of FCs, which modulates the phase of the incoming beam [6]. In addition to providing the required diffraction pattern and high efficiency, the unit cell profile has to have a minimum radius of curvature (MRC) meeting the manufacturing capability, beyond which the machine is not able to faithfully pattern. This minimum radius of curvature is limited by the diameter of available ball-end milling tools for fabrication via Computer Numerically Controlled (CNC) machining. Thus an optimization process needs to be performed. There are two main parameters for such an optimization. First is the number of applied FCs, which is proportional to the efficiency and inversely proportional to the MRC; second is the unit cell size, which is proportional to the MRC and inversely proportional to the divergence of the diffraction pattern.

The FCs for deriving the 2D profiles for beam multiplexing by 4 and 2 are calculated in MATLAB and optimised using a genetic algorithm to ensure the maximum achievable efficiency. They are then orthogonally superimposed to make the surface topology of the unit cell of an 8-pixel grating. The rectangular uniform arrangement of the diffracted beams requires the power to be distributed only among the 8 products of the diffraction orders of $m = \pm 1$ and $n = \pm 3$.

We use 13 FCs to simulate a 3x3 cm^2 grating, consisting of 25 times the unit cell of 1.2x1.2 mm^2 in two orthogonal directions, for operation at 4.7 THz with 25° incident angle with respect to the normal. A 3D drawing of 16 unit cells of the

phase grating is shown in Fig. 6.1a. We only show a part of the whole grating (225 unit cells), otherwise it would not allow a detailed view of the surface structure. Note that for clarity, the height is out of scale.

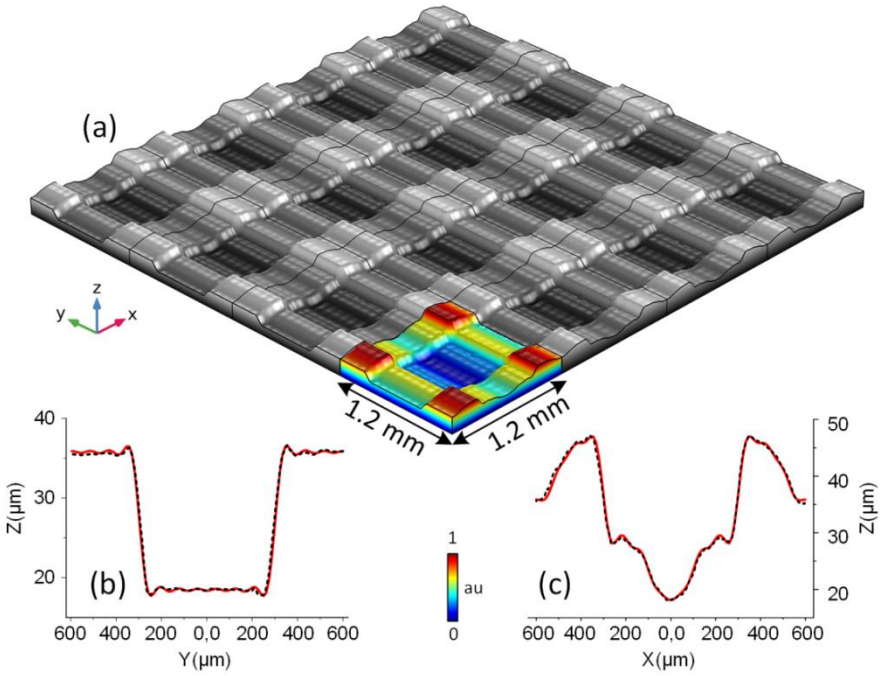

Figure 6.1. a) 3D drawing of 16 unit cells of the phase grating. A single unit cell is shown in colour. The height is out of scale for clarity, (b), (c) The calculated and manufactured 2D cross-section profiles of a unit cell. Z shows the height, and X and Y are the two lateral directions. The dashed black and solid red curves are the manufactured and calculated results respectively.

Based on the grating equation [13], $\sin\beta = \sin\alpha + m\lambda/\Lambda$, an angle of ~ 6° is expected between two adjacent diffracted beams, where α and β are the angles of incidence and the m'th (± 1 and ± 3) diffraction order respectively and Λ is the grating periodicity (equal to the unit cell size). The desired angle is chosen mainly based on the beam configuration of an existing HEB mixer array and its distance to the grating. This design results in an MRC of 112 μm, which is larger than the 90-μm radius of the ball end mill (available at the time we started) used with the KERN EVO micro-milling machine (at Arizona State University) that is employed for the

grating manufacturing. In other words, the available machine is able to pattern all the fine surface structures. An aluminium plate (Aloca QC-10 Mold Alloy) is chosen as the grating material because of its very high reflectivity [14] and manufacturability. The manufactured 2D cross sections of a unit cell are measured by a Dektak XT30 stylus profiler and plotted in Figs. 6.1b and 6.1c together with the calculated ones. They show very good matches with deviations in amplitude of < 1 µm.

6.3. Quantum cascade laser and the experimental setup

As the input source, we use a third order DFB QCL with an GaAs/AlGaAs active region based on four-well resonant phonon depopulation scheme [15]. It consists of 21 periods over a length of about 0.55 mm with 17-µm width and 10-µm thickness. Multiple lasers with a 7.5 GHz frequency spacing are grouped together on a single chip with a linear frequency coverage that allows targeting of a specific frequency. The active region was grown at Sandia National Laboratories by molecular beam epitaxy (MBE) while the QCLs were designed and fabricated at MIT. We choose a QCL with a single mode emission at 4.756 GHz mainly because of a relatively low water absorption in air at this frequency. The QCL was operated at a temperature of ~ 7 K using a pulse tube cooler. No power measurement was done for this specific QCL. However, based on the measured power of a similar laser on a different chip [16], we expect it to be around 0.25 mW.

A room temperature pyro-electric detector with an aperture diameter of 2 mm, mounted on a X-Y translational stage, is used for all the beam pattern measurements in this work. The QCL beam profile is measured in front of the cryostat window at a ~ 3 cm distance from the laser and plotted in Fig. 6.2a.

The QCL beam is highly divergent with a strong deviation from a Gaussian profile. This QCL has the beam pattern that is worse than the others studied previously in our group [12,16]. Directly applying such a beam to the grating leads to the same order of divergence for the individual diffracted beams, which is more than their angular separation. This means that they are merged and would not be

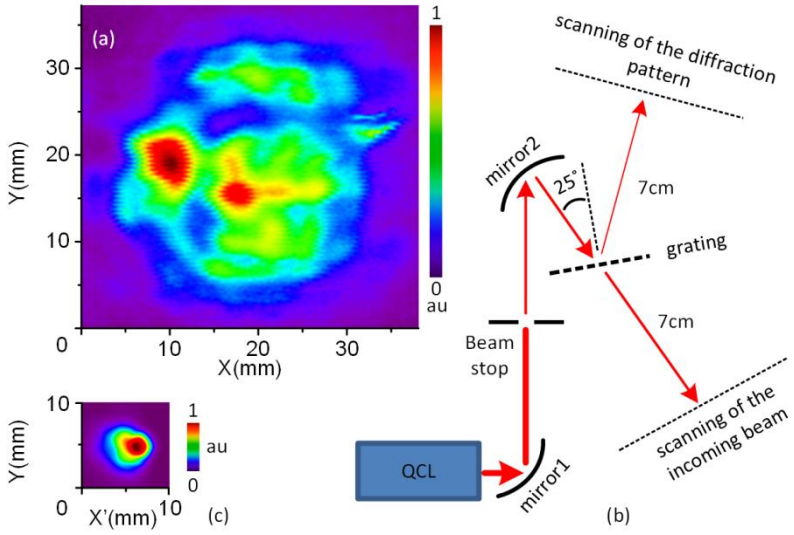

Figure 6.2. a) Quantum cascade laser beam pattern measured in front of the cryostat window; b) Optical setup for collimation and filtering the laser beam. the line thickness is an indication of the intensity; c) incoming collimated beam to the grating.

resolved from each other. Therefore we have introduced a spatial mode filter shown schematically in Fig. 6.2b. Two parabolic mirrors are used for beam collimation. An iris beam stop in between the mirrors reduces the beam size by partially passing the left bright spot (and blocking the rest). This is the optimum setup we can make for this purpose regarding to the geometrical constraints. The resulted collimated beam shown in Fig. 6.2c then illuminates the grating at 25° incident angle with respect to the normal. For the reason to be explained in the next section, we measure the filtered beam at 7 cm away from the grating position when it is removed. The aperture size of the beam stop is adjusted to maximize the passing QCL power whilst still resolving separated diffracted beams at a reasonable distance from the grating. By integrating the intensity of the beam patterns and considering about 1.4 and 0.5 dB absorption losses by the cryostat UHMW-PE window and the air respectively, we find that about 78 % of the total QCL power in the whole beam pattern is blocked by this setup. This large power waste already explains the crucial role of the laser beam pattern. If the latter was more

concentrated in a small area, a much smaller (or no) portion would be needed to be removed.

6.4. Measurement and simulation results

Since the grating unit cell has two different orthogonal cross-sections, it results in two different diffraction beam patterns (either 4 by 2 or 2 by 4) when illuminated from each orthogonal direction [11]. The beam patterns measured at a distance of 7 cm from the grating using the setup shown in Fig. 6.2b, for both cases are plotted in Fig. 6.3. The high-resolution patterns have been achieved by fine scanning with a step size of 0.1 mm. We measure the incoming beam in the same distance from the (removed) grating to cancel out the effect of the air absorption in the efficiency calculations later on. As expected, all diffracted beams copy the incoming beam profile, but horizontally flipped. The predicted ~ 6° angular distance between each two adjacent beams is experimentally confirmed. The unwanted higher diffraction orders are visible around the desired ones with much weaker intensities. This gives a good visual feeling of the efficiency. Since both diffraction patterns show a similar behaviour in terms of power and spatial distribution, we focus on the result shown on the left side (4x2) in the rest of the paper.

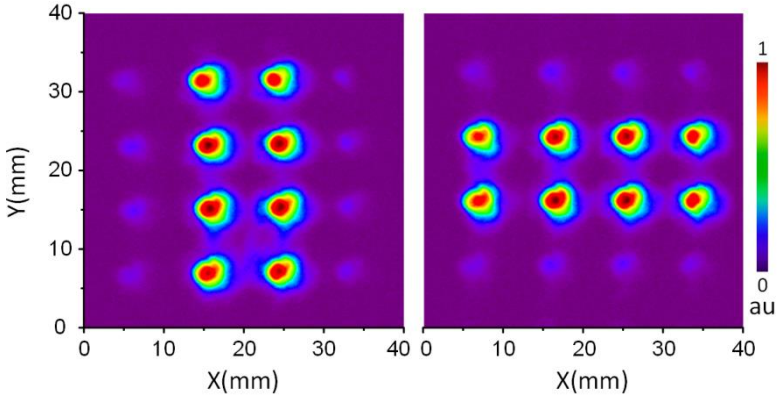

Figure 6.3. Measured diffraction patterns of the grating at 4.7 THz using a quantum cascade laser with 25° of incidence in two different orthogonal directions.

For estimating the efficiency, we take the ratio between the integrated intensities of all the desired diffracted beams and the one of the incoming beam. It should be mentioned that the noise floor of the room temperature detector, which can affect the efficiency analysis, is removed before the integration. We find an efficiency of 74.3 %, which is close to 75.4 % predicted by a 3D simulation using the RF module of COMSOL. The latter is done by importing the grating surface profile and simulating a periodic port with periodic boundary conditions. Extracting the S parameters of the port then gives the efficiency. The maximal grating efficiency is dependent on the diffraction pattern. So the 75.4 % efficiency is associated with our prerequisite 4x2 rectangular beam configuration, otherwise the efficiency can be different.

We analyse the uniformity of the power distribution among the diffracted beams by applying the same method of integrating the intensity. The fractions of the incoming beam power distributed to the diffracted beams shown on the left side of Fig. 6.3 from top to bottom of the left column are 9 %, 10.4 %, 9.5 %, and 8.6 % and on the right column are 8.6 %, 10.3 %, 9.3 % and 8.4 %. The power in the individual beams varies within ~ 21 % around its average value. The 3D simulation also shows that the intensities of the four central beams are slightly higher to the same extent.

In order to confirm that such a power variation among the diffracted beams may not deteriorate the performance of an HEB array, in which all the HEBs require the same LO power, we use our existing experimental data to evaluate the effect of the LO power tolerance to the sensitivity of a single mixer. This particular measurement was done at 4.3 THz (very close to our frequency of interest). The receiver noise temperature (T_{rec}) of the HEB mixer was measured as a function of LO power, reflected by the HEB current (inversely proportional to the LO power) at a constant bias voltage of 0.8 mV. The result is shown in the inset of Fig. 6.4 and suggests the optimum current of ~ 38 μA, in which the T_{rec} becomes minimal [17]. The correspondence between the current and the LO power can be estimated from the pumped current-voltage (I-V) characteristics by using the isothermal technique

[18]. The multiple I-V curves, measured at different LO powers, are plotted in Fig. 6.4, where the top curve (in brown) is recorded without LO (superconducting state) and the bottom (in red) with a sufficiently high LO power to fully pump the device (to the resistive state). By estimating all the LO powers and their corresponding T_{rec}s we find that the change in the T_{rec} is less than 4 % when the LO power varies within about 21 %. We therefore conclude that despite the power variation (~ 21 %), the multi-beam LO made by our phase grating can pump a uniform HEB array without affecting the uniformity of the T_{rec}.

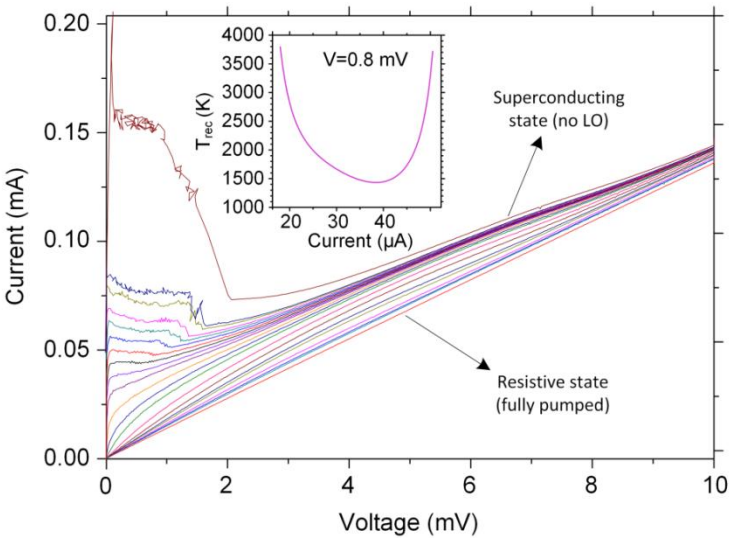

Figure 6.4. The current-voltage characteristics of the HEB mixer at different levels of the LO power, which is zero in the top curve (in brown) and sufficient to fully pump the device in the bottom curve (in red). Inset: Measured receiver noise temperature (T_{rec}) of a hot electron bolometer (HEB) mixer versus the current at a bias voltage of 0.8 mV. The current is inversely proportional to the absorbed local oscillator (LO) power.

We study the effect of the number of applied FCs on the grating efficiency and manufacturability using the same 3D simulation. The results, which are plotted in Fig. 6.5a, show that decreasing this factor from 13 to 6 degrades the efficiency from 75.4 to 69 % (by ~ 6 %) while increases the MRC by ~ 274 μm (~ 300 %). As explained before, the MRC determines the manufacturing requirement, which is

the size of the ball end mill in our case. This is an interesting and useful finding since one can ease the manufacturing considerably by sacrificing a few percent of the efficiency. 3D surface profiles of the resulting unit cells from applying 6 and 13 FCs are plotted in Figs. 6.5b and 6.5c, respectively, illustrating the effect on the surface fines and challenge of the manufacturing.

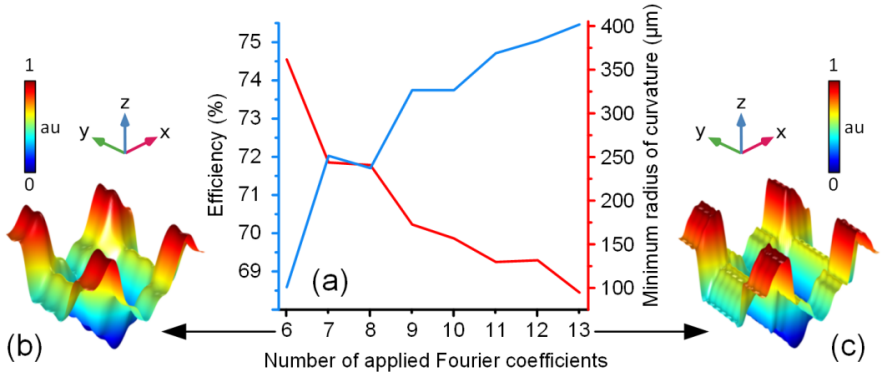

Figure 6.5. a) Grating efficiency and the surface minimum radius of curvature (MRC), versus the number of applied Fourier coefficients (FCs) in design; b,c) 3D profiles of the unit cells made by 6 and 13 FCs, respectively.

6.5. Grating operation bandwidth

The bandwidth of a phase grating is an interesting property, which has so far been less explored. In theory, it can perform well over a wide frequency band by properly changing the incident angle. A grating designed for the frequency f with an incident angle θ with respect to the normal works with the same efficiency as long as the value of $f \times \cos(\theta)$ is fixed. In our case, if we consider an applicable range of 0 to 45 degrees for the incident angle, the grating can function optimally from 4.3 to 6 THz.

Due to the limited available THz sources, we verify the performance of the 4.7 THz grating using a FIR gas laser line at 5.3 THz. The measured incident beam and the resulting diffraction pattern at 15 cm away from the grating are plotted in Fig. 6.6.

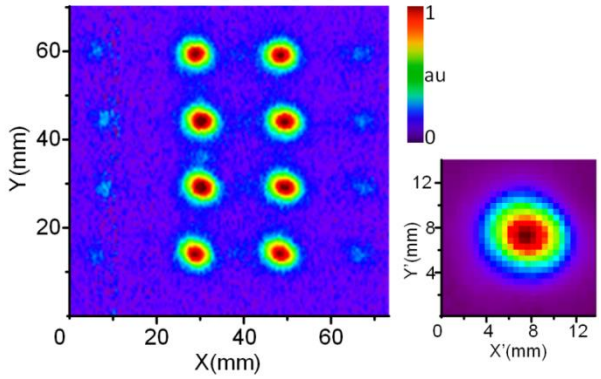

Figure 6.6. Diffraction beam pattern measured at a distance of 15 cm from the grating (left) and the incident beam (right) at 5.3 THz measured using a FIR gas laser.

In this particular measurement, the incident angle is chosen to be 37° (as opposed to 25° for 4.7 THz). The diffracted beams are in the same order of spatial and power distributions as the case of 4.7 THz described earlier in this paper. The derived efficiency by applying the same analysing method is 74 %, being almost equal to the 4.7 THz case. Our measurement at 5.3 THz, being 0.6 THz higher than the targeted frequency, confirms that the grating bandwidth should be more than 13 %. The broadband grating characteristic offers a potential for other applications including multiple imaging at different frequencies using a single grating [19].

6.6. Pumping a superconducting HEB mixer

To further quantify the performance of the 4.7 THz grating, we perform an experiment, in which we apply one of the eight diffracted beams (originated from the QCL) as the LO to pump a superconducting HEB mixer. We have to change the optical setup in order to redirect the diffracted beams towards a suitable place for putting and manually fine positioning a bulky liquid helium cryostat, in which the HEB is mounted. By doing so and considering the very limited geometrical flexibility, we could illuminate the grating with only about 9 µW. An additional beam stop is introduced after the grating to pick only one, out of the eight

diffracted beams. Then it is coupled into a quasi-optical (lens-spiral antenna) HEB mixer using a focusing lens. We succeed in coupling ~ 50 nW to the HEB mixer, which is derived from the pumped I-V characteristics using the isothermal technique [18]. By taking into account the total optical loss of ~ 32.6 dB [20] in the entire system, we find that ~ 91 μW of the QCL power is used (we assume that the QCL has a 0.25 mW output power). We think this power fraction is reasonable by attributing the difference to the partial mismatch between the non-Gaussian LO beam and beam of the HEB mixer, and also to the uncertainty in the actual QCL output power.

Let us now estimate the required QCL power for a practical 8-pixel array with spiral antenna coupled HEB mixers. To do so, we consider the system as the following; a) each mixer needs a pumping power of 220 nW; b) Si lens for the mixer has an antireflection (AR) coating at 4.7 THz; c) a 3 μm thick Mylar beam splitter is used for a heterodyne measurement; d) the setup is in vacuum; e) the focusing lens is made of silicon with double sided AR coating at 4.7 THz; f) The QCL has an ideal Gaussian beam. This system has an optical loss of ~ 26.2 dB [21], implying that a power of ~ 92 μW from the QCL is needed in this case. However, the fraction of the power in the beam in the fundamental Gaussian mode can be much less (e.g. 10 %) in practice, which increases the required QCL output power considerably (e.g. 0.9 mW). It is worth to mention that producing THz QCLs with either higher power or improved beam profile seems to be feasible [22,23] considering the rapid progress being made in the community.

6.7. Conclusion

We report for the first time a Fourier phase grating for generating eight local oscillator beams using a single mode 4.7 THz DFB quantum cascade laser as the input source. We characterized the grating performance by measuring the diffraction pattern and deriving the diffraction efficiency of 74.3 %, which is in an excellent agreement to the 3D simulation result. We demonstrated that the power uniformity of such a multi beam LO is sufficient, leading to uniform sensitivities of

the array mixers. The effects of applying different number of Fourier coefficients in simulation, on the efficiency and manufacturing is discussed. The broad-band characteristic of the grating is verified by its evaluation at 5.3 THz, where we found the same performance as the case for 4.7 THz. Finally we analysed the power issue by coupling one of the diffracted beams generated by the QCL-grating combination to a superconducting hot electron bolometer mixer. We estimate that an 8-pixel array receiver, in which each mixer needs a power of 220 nW, requires from 92 μW to 0.9 mW for the QCL power if its Gaussian component has a power fraction from 100 to 10 %.

Our work demonstrates the principle of a novel array local oscillator technology, which is demanded for future space missions. It is a prototype LO unit for a NASA science mission GUSTO (Galactic/X-galactic Ultra-duration-balloon Spectroscopic/Stratospheric Terahertz Observatory), which is scheduled to launch in 2021 from Antarctica and map three THz fine structured lines including [OI] using an 8-pixel receiver array.

Bibliography

[1] C. Kulesa, “Terahertz spectroscopy for astronomy: from comets to cosmology,” IEEE Trans. THz Sci. Tech. **1**, 232 (2011).

[2] C. Walker, Terahertz Astronomy (CRC, Taylor & Francis Group, 2016), Chap. 5&6.

[3] J. V. Siles, R. H. Lin, C. Lee, E. Schlecht, A. Maestrini, P. Bruneau, A. Peralta, J. Kloosterman, J. Kawamura and I. Mehdi, “Development of high-power multi-pixel LO sources at 1.47 THz and 1.9 THz for astrophysics: present and future,” in Proceedings of the 26th International Symposium on Space Terahertz Technology, Cambridge, MA (2015).

[4] C. Groppi, C. Walker, C. Kulesa, D. Golish, J. Kloosterman, S. Weinreb, G. Jones, J. Barden, H. Mani, T. Kuiper, J. Kooi, A. Lichtenberger, T. Cecil, G. Narayanan, P. Pu¨tz and A. Hedden, “SuperCam: A 64 pixel heterodyne array receiver for the 350 GHz atmospheric window,” in Proceedings of the 20th International Symposium on Space Terahertz Technology, Charlottesville (2009).

[5] J. A. Murphy, C. O. Sullivan, N. Trappe, W. Lanigan, R. Colgan and S. Wittington, “Modal Analysis of the Quasi-Optical Performance of Phase Gratings,” Int. J. Inf and Mill Waves **20**, 1469 (1999).

[6] U. U. Garf and S. Heyminck, “Fourier gratings as submillimeter beam splitters,” IEEE Trans. Antennas Propag. **49**, 542 (2001).

[7] A. G. G. M. Tielens and D. Hollenbach, “Photodissociation regions. I. basic model. II. A model for the Orion photodissociation Region” ApJ. **291**, 722 (1985).

[8] S. Leurini, F. Wyrowski, H. Wiesemeyer, A. Gusdorf, R. Gusten, K. M. Menten, M. Gerin, F. Levrier, H. W. Hubers, K. Jacobs, O. Ricken and H. Richter, “Spectroscopically resolved far-IR observations of the massive star-forming region G5.89-0.39,” A&A. **584**, A70 (2015).

[9] B. S. Williams, “Terahertz quantum-cascade lasers,” Nat. Photonics **1**, 517 (2007).

[10] M. I. Amanti, G. Scalari, F. Castellano, M. Beck and J. Faist, “Low divergence Terahertz photonic-wire laser,” Opt. Express **18**, 6390 (2010).

[11] B. Mirzaei, J. R. G. Silva, Y. C. Luo, X. X. Liu, L. Wei, D. J. Hayton, J. R. Gao and C. Groppi, "Efficiency of multi-beam Fourier phase gratings at 1.4 THz," Opt. Express **25**, 6581 (2017).

[12] M. Cui, J. N. Hovenier, Y. Ren, N. Vercruyssen, J. R. Gao, T. Y. Kao, Q. Hu and J. L. Reno, “Beam and phase distributions of a terahertz quantum cascade wire laser”, Appl. Phys. Lett. **102**, 111113 (2013).

[13] W. C. Elmore and M. A. Heald, Physics of waves (Dover Publications, Inc., New York, 1969).

[14] H. Ehrenreich, H. R. Philipp and B. Segall, “Optical properties of aluminum,” Phys. Rev. **132**, 1918 (1963).

[15] B. S. Williams, S. Kumar, Q. Hu and J. L. Reno, “Resonant phonon terahertz quantum-cascade laser operating at 2.1 THz (λ ≈ 141 μm),” Elec. Lett. **40**, 431 (2004).

[16] J. L. Kloosterman, D. J. Hayton, Y. Ren, T. Y. Kao, J. N. Hovenier, J. R. Gao, T. M. Klapwijk, Q. Hu, C. K. Walker and J. L. Reno, “Hot electron bolometer heterodyne receiver with a 4.7-THz quantum cascade laser as a local oscillator,” Appl. Phys. Lett. **102**, 011123 (2013).

[17] W. Zhang, P. Khosropanah, J. R. Gao, T. Bansal, T. M. Klapwijk, W. Miao and S. C. Shi, “Noise temperature and beam pattern of an NbN hot electron bolometer mixer at 5.25 THz,” J. Appl. Phys. **108**, 093102 (2010).

[18] H. Ekström, B. S. Karasik, E. Kollberg and K. S. Yngvesson, “Conversion gain and noise of niobium superconducting hot-electron-mixers,” IEEE Trans Microw. Theory Tech. **43**, 938 (1995).

[19] L. P. Boivin, "Multiple Imaging Using Various Types of Simple Phase Gratings," Appl. Opt. **11**, 1782 (1972).

[20] The quoted optical loss is contributed by the HEB-antenna coupling (0.5 dB), the spiral antenna (3 dB, for a linearly polarized Gaussian beam), the Si lens reflection loss (1.2 dB), the QMC heat filter (0.4 dB), the HEB cryostat UHMW-PE window (1.4 dB), the HDPE focusing lens (1.2 dB), the air loss (1 dB), the phase grating (10 dB), the beam stop (in combination with two mirrors) (12.5 dB), and the UHMW-PE window of the QCL cryostat (1.4 dB).

[21] The quoted optical loss is contributed by the HEB-antenna coupling (0.5 dB), the spiral antenna (3 dB, for a linearly polarized Gaussian beam), the AR coated Si lens reflection loss (0.15 dB), the QMC heat filter (0.4 dB), the HEB cryostat UHMW-PE window (1.4 dB), the Si focusing lens with AR coating on both sides (0.3 dB), the phase grating (10 dB), the beam splitter (9 dB), and the UHMW-PE window of the QCL cryostat (1.4 dB).

[22] T. Y. Kao, X. Cai, A. W. M. Lee, J. Reno and Q. Hu, “Antenna coupled photonic wire lasers,” Opt. Express **23**, 17091 (2015).

[23] A. Khalatpour, J. L. Reno, N. P. Kherani and Q. Hu, “Unidirectional photonic wire laser,” Nat. Photon. **11**, 555 (2017).

SUMMARY

QUANTUM CASCADE LASERS AS SUPER TERAHERTZ LOCAL OSCILLATORS FOR ASTRONOMY

Quantum cascade laser (QCL) technology has made a breakthrough in THz radiation sources, opening a new window into variety of applications. QCLs are compact, low-consumption and narrow linewidth lasers with relatively high output powers, capable to emit radiation across the whole super-THz (2-6 THz) range. These are all demanded for spectroscopy, which is so interesting in THz due to the fingerprint molecular rotational absorption/emission spectrums. Among many other potential applications of spectroscopy including chemical identification, security checking and biomedical diagnosis, high-resolution probing of celestial fine structured lines is prominent for addressing the human permanently staying curiosity about the origins of stars, galaxies and the Universe.

Incorporating THz QCLs as local oscillators (LOs) in heterodyne receivers broadens their spectral field of view towards the higher end of the THz region, where a number of useful probes like [OI] line at 4.7 THz are located. Practical adaptation of THz QCLs for such LO application is the main theme of this thesis. The most promising unique LO-qualified THz QCLs based on the third-order DFB mechanism have been used throughout this work to stay on the border of technology and make the outcome more practical, realistic and applicable.

Although the intrinsic linewidths of THz QCLs are quite narrow (~ 110 Hz), the fluctuations in temperature and biasing system broaden it up to the MHz range, wider than required upper limit for resolving many interesting lines. This issue can be effectively overcome using frequency/phase locking techniques. This crucial adaptation has been demonstrated in this thesis in a novel configuration, where the radiation of a THz QCL has been used in both directions for the first time. The crucial role of the detector sensitivity in frequency locking also has been nicely shown using such a setup. Making use of the QCL radiation in both directions has a high impact on its applicability as LO in terms of the output power, where one side can be used for frequency/phase stabilization, leaving the other to be fully utilized as an LO to pump a mixer. This work and the idea behind, can be even more efficiently applied to the advanced unidirectional THz QCLs, in which only about 10 % of the power flows in the reverse direction. Application of two superconducting HEBs on both laser sides can give a clearer observation of the locking quality. Finally, a space-applicable superlattice harmonic mixer can be used for stabilization i.e. demonstration of a power-efficient prototype frequency locking module for a certain space project.

The other demanded capability is the frequency adjustment of already processed QCLs, which have deviations from the aimed frequency range due to the limited lithographical accuracy or the frequency shift caused by long usages in different experiments. The latter had happened to the 4.7 THz QCL aimed to be applied as the LO for NASA's STO2 (Stratospheric terahertz observatory 2), with a shift of 11 GHz out of the [OI] line frequency. The work presented in chapter 4 was initiated to develop a technique for solving this problem, which led to an extensive study on using dielectrics for frequency tuning of THz QCLs, where a considerable shift of ~ 13 GHz has been reported. As simulations offer even more possible tuning ranges, for further advancement, one can try to considerably improve the effect of the applied PMMA layer by using an adhesion promoter to GaAs like Surpass 3000. This requires several additional steps in order to understand and control the process. The other relatively ambitious idea to advance this work is using a coating

material with sufficient thermal expansion. Once such a material is available a continues broad tuning ranges can be achieved only by tuning the temperature.

While pushing the sensitivities of THz heterodyne receivers further towards the quantum noise limit has become very challenging and slowly progressing, increasing the number of pixels is another way to improve the observing efficiency through speeding up the sky mapping. Developing array receivers therefore, has been in focus by the community for many years. For this purpose, in parallel to arrays of ultra-sensitive mixers, array LOs should be also developed for their uniform optical pumping. For the latter at super-THz however, providing several identical LO-qualified QCLs is quite challenging, which further requires complex synchronization systems. Instead, multiplexing the beam of a single QCL is an efficient approach, which can be effectively done using phase gratings.

Demonstration of the first THz Fourier phase grating with a high power efficiency is reported in chapter 5 of this thesis, where the 1.4 THz radiation from a far-infrared (FIR) gas laser was turned into 4 and 8 beams following the simulation results. This establishment and its associated analysis and simulations made a reliable platform for taking a step forward towards the demanded technology at 4.7 THz.

Chapter 6 of this thesis presents the realization and demonstration of an 8-pixel LO operating at the significant [OI] line (4.7 THz), made by combination of a phase grating and a QCL. This is the highest operating frequency of THz phase gratings reported in the literature. The phase grating has been even tested at 5.3 THz using an FIR gas laser to evaluate its operation bandwidth. Such a system is highly demanded by future THz heterodyne array receivers as it is considered as the prototype LO unit for the higher frequency channel of NASA science mission GUSTO (Galactic/X-galactic Ultra-duration-balloon Spectroscopic/Stratospheric Terahertz Observatory).

Increasing the number of pixels is of course the most interesting advance in THz array receivers. For such a purpose in principle, a proper phase grating with a large number of desired diffraction orders can be realized. However, the output power

of the source (i.e. QCL) should be increased almost with the same scale, which is the main limiting factor for the number of pixels. On the other hand, proper alignment i.e. collimation of a large number of generated beams and making the whole pattern matching to a mixer array is also challenging. A potential idea to overcome this issue is curving the whole grating surface in order to act as a parabolic mirror at the same time. Although it seems ambitious, it is worthy to deeply look at.

The other promising idea for advancing the LO arrays is the integration, which can be pursued considering the fact that only 2 unit cells are enough for the grating to function. This can lead to a compact and robust multi-beam collimated THz source, in which the grating(s), the QCL and the optics are integrated.

While it is tried in this thesis to adapt the THz QCLs for astronomical applications though their frequency stabilization, tuning and beam multiplexing, the need for their beam shape correction still should be addressed. Although this has been a strong concern in the QCL community to further optimize the laser structure in order to make a more Gaussian-like beam pattern, developing an external optical component in parallel can be achieved relatively easier and quicker. An idea for that purpose is making a compact integrated spatial filter to be placed in front of a QCL beam for extracting its Gaussian component. This can be achieved using two similar elliptical silicon lenses placed back-to-back with a small aperture at the interface to act as a filter. Unlike back-to-back feed horn structures, this system can be relatively easily and cheaply made for super-THz frequencies.

ACKNOWLEDGEMENTS

Although I tend to be independent, looking back at this *short* four-years period of my PhD, I immediately see that it was impossible to be accomplished lonely. Here I would like to thank everyone who helped me progressing, even in a short moment or by a tiny hint.

I first thank my promoter, Prof. Leo Kouwenhoven with his valuable support and encouragements. Our regular meetings have been always ending up with a boosted motivation and fortified hopes.

I would also like to express my deep gratitude to my wonderful daily supervisor, Dr. Jian Rong Gao. Gao, since a long time before starting my PhD you have been offering your help and support to me. During my PhD, I mostly remember your kind advices and motivating criticisms in a wide range, from the lab technical issues to the paper writing corrections and comments. I especially thank you Gao for making such a unique opportunity to orient my PhD towards the real space projects like NASA's STO2 and GUSTO. Hope the latter can successfully fly in 2021.

Now it's time to remember the great moments we made together with Jose Silva from SRON, either in Delft or Groningen, doing exciting experiments. Thanks Jose for your great contribution. In addition, I appreciate the help and support from my colleagues and friends including Nuri van Marrewijk, who helped me settle in

the lab in the beginning of my PhD, Darren Hayton for his kind supports and advices, David Thoen, who offered his time and expertise to me with his technical assistance. The efforts from the THz sensing group especially Akira Endo for organizing the regular Friday meetings are also appreciated, which gave the opportunity to present my progress and get feedbacks. I also acknowledge the crucial collaboration of MIT team headed by Prof. Qing Hu for providing the state-of-the-art THz QCLs, and also the financial support given by the Delft space institute.

I am also grateful to all my Iranian friends here in the Netherlands especially Masoud Mirzaei and his family who helped us getting accustomed with and settled in the new living environment.

Finally, I would like to extend my greatest acknowledgements and appreciations to my father and mother, my kind and compassionate spouse and my beloved daughter, who are all I have and all I love.

LIST OF PUBLICATIONS

Journal Papers

1. B. Mirzaei, J. R. G Silva, D. Hayton, C. Groppi, T. Y. Kao, Q. Hu, J. L. Reno, and J. R. Gao, "8-beam local oscillator array at 4.7 THz generated by a phase grating and a quantum cascade laser," Optics Express 25 (24), 29587-96 (2017).
2. B. Mirzaei, J. R. G. Silva, Y. C. Luo, X. X. Liu, L. Wei, D. J. Hayton, J. R. Gao, and C. Groppi, "Efficiency of multi-beam Fourier phase gratings at 1.4 THz," Optics Express 25 (6), 6581-6588 (2017).
3. B. Mirzaei, D. Hayton, D. Thoen, J. R. Gao, T. Y. Kao, Q. Hu, and J. L. Reno, "Frequency tuning of third-Order distributed feedback terahertz quantum cascade lasers by SiO_2 and PMMA," IEEE Transactions on Terahertz Science and Technology 6 (6), 851-857 (2016).
4. N. van Marrewijk, B. Mirzaei, D. Hayton, J. R. Gao, T. Y. Kao, Q. Hu, and J. L. Reno, "Frequency locking and monitoring based on bi-directional terahertz radiation of a 3rd-order distributed feedback quantum cascade laser," Journal of Infrared, Millimetre, and Terahertz Waves 36 (12), 1210-1220 (2015).

Conference Papers

1. B. Mirzaei, J. R. G Silva, D. Hayton, W. Laauwen, Y. Gan, Q. Hu, C. Groppi, and J. R. Gao, "Prototype 4.7 THz array local oscillator for GUSTO," in Proceedings of the 29th International Symposium on Space Terahertz Technology, Pasadana, California, USA (2018).
2. J. R. G Silva, D. Hayton, B. Mirzaei, W. Laauwen, Y. Gan, A. Young, C. Kulesa, C. Walker, and J. R. Gao, "Preliminary design study of a 4×2 HEB array at 4.7 THz for GUSTO," in Proceedings of the 29th International Symposium on Space Terahertz Technology, Pasadana, California, USA (2018).

3. J. R. G Silva, B. Mirzaei, W. Laauwen, Q. Hu, C. Groppi, C. Walker, and J. R. Gao, "4×2 HEB receiver at 4.7 THz for GUSTO," in Proceedings of SPIE 10708 (Millimeter, Submillimeter, and Far-Infrared Detectors and Instrumentation for Astronomy IX), Austin, Texas, USA (2018).
4. J. R. G Silva, B. Mirzaei, D. Hayton, J. R. Gao, and C. Groppi, "2x4 HEB array receiver at 1.4 THz based on a multi-beam Fourier phase grating LO," in 38th ESA Antenna Workshop (Innovative Antenna Systems and Technologies for Future Space Missions), ESTEC, Noordwijk, The Netherlands (2017).
5. B. Mirzaei, J. R. G Silva, J. R. Gao, C. Groppi, T. Y. Kao, Q. Hu, and J. L. Reno, "An 8-Beam, 4.7 THz Local Oscillator Using a Quantum Cascade Laser and a Phase Grating," in 14th International Conference on Intersubband Transitions in Quantum Wells, Singapore (2017).
6. B. Mirzaei, J. R. G. Silva, Y. C. Luo, X. X. Liu, L. Wei, D. J. Hayton, J. R. Gao, and C. Groppi, "4 and 8-pixel THz Fourier phase gratings," in proceedings of the 28th International Symposium on Space Terahertz Technology, Cologne, Germany (2017).
7. B. Mirzaei, D. Hayton, D. Thoen, J. R. Gao, T. Y. Kao, Q. Hu, and J. L. Reno, "Dielectric deposition for tuning the frequency of THz quantum cascade lasers," in proceedings of the 28th International Symposium on Space Terahertz Technology, Cologne, Germany (2017).
8. J. R. G. Silva, X. Liu, B. Mirzaei, Y. C. Luo, D. J. Hayton, J. R. Gao, and C. Groppi, "Demonstration and stabilization of a 4x2 HEB array receiver at 1.4 THz based on a Fourier phase grating LO," in proceedings of the 28th International Symposium on Space Terahertz Technology, Cologne, Germany (2017).
9. B. Mirzaei, D. Hayton, D. Thoen, J. R. Gao, T. Y. Kao, Q. Hu, and J. L. Reno, "Frequency tuning of third-Order distributed feedback terahertz quantum cascade lasers by SiO_2 and PMMA," International Quantum Cascade Lasers School and Workshop, Cambridge, UK (2016).
10. B. Mirzaei, N. van Marrewijk, D. Hayton, J. R. Gao, T. Y. Kao, Q. Hu, and J. L. Reno, "Simultaneous frequency locking and monitoring using a bi-directional THz quantum cascade laser," in proceedings of the 27th International Symposium on Space Terahertz Technology, Nanjing, China (2016).
11. D. Hayton, J. R. Gao, W. Laauwen, B. Mirzaei, A. Khudchenko, J. L. Kloosterman, D. Paveliev, Q. Hu, W. Kao, V. Vax, and C. Walker, "A 4.7 THz

HEB QCL Receiver for STO2," in proceedings of the 27th International Symposium on Space Terahertz Technology, Nanjing, China (2016).

12. B. Mirzaei, N. van Marrewijk, D. Hayton, J. R. Gao, T. Y. Kao, Q. Hu, and J. L. Reno, "Simultaneous frequency locking and monitoring using a bi-directional THz quantum cascade laser, "Frequency locking and monitoring based on bi-directional terahertz radiation of a 3rd-order distributed feedback QCL," in the 13th International Conference on Intersubband Transitions in Quantum Wells, Vienna, Austria, (2015).